NASA Contractor Report 185188

Thermomechanical Deformation Testing and Modeling in the Presence of Metallurgical Instabilities

Michael G. Castelli

Sverdrup Technology, Inc.
NASA Lewis Research Center Group
Cleveland, Ohio

January 1990

Prepared for
Lewis Research Center
Under Contract NAS3-25266

National Aeronautics and
Space Administration

THERMOMECHANICAL DEFORMATION TESTING AND MODELING IN THE PRESENCE OF METALLURGICAL INSTABILITIES

Michael G. Castelli
Sverdrup Technology, Inc.
NASA Lewis Research Center Group
Cleveland, Ohio 44135

ABSTRACT

A number of viscoplastic constitutive models have been developed to describe deformation behavior under complex combinations of thermal and mechanical loading. Questions remain, however, regarding the validity of procedures used to characterize these models for specific structural alloys. One area of concern is that the majority of experimental data available for this purpose are determined under isothermal conditions. This experimental study is aimed at determining whether viscoplastic constitutive theories characterized using an isothermal data base can adequately model material response under the complex thermomechanical loading conditions typical of power generation service.

The approach adopted was to conduct a series of carefully controlled experiments on a nickel–based superalloy, Hastelloy Alloy X. Previous investigations had shown that this material experiences metallurgical instabilities leading to complex hardening behavior, termed dynamic strain aging. Investigating this phenomenon under full thermomechanical conditions leads to a number of challenging experimental difficulties which up to the present work were unresolved. To correct this situation, a number of advances were made in thermomechanical testing techniques. Advanced methods for dynamic temperature gradient control, phasing control and thermal strain compensation

were developed and incorporated into real–time test control software. These advances allowed the thermomechanical data to be analyzed with minimal experimental uncertainty.

The thermomechanical results were evaluated on both a phenomenological and microstructural basis. Phenomenological results revealed that the thermomechanical hardening trends were not bounded by those displayed under isothermal conditions. For the case of Hastelloy Alloy X (and similar dynamic strain aging materials), this strongly suggests that some form of thermomechanical testing is necessary when characterizing a thermoviscoplastic deformation model. Transmission electron microscopy was used to study the microstructural physics, and analyze the unique phenomenological behavior. In general, the thermomechanical response was found to be dominated by behavioral trends associated with the maximum cycle temperature. Having clearly identified the factors affecting the thermomechanical behavior, an existing thermoviscoplastic constitutive model is extended to qualitatively predict the thermomechanical hardening trends of Hastelloy Alloy X, a dynamic strain aging material. The approach taken in this study involves the introduction of an evolving internal state variable which accounts for the effects of microstructural changes under thermomechanical conditions.

TABLE OF CONTENTS

CHAPTER 1

INTRODUCTION

Essentially all structural components used in high temperature power systems experience non–isothermal loading. During the life of these components, inelastic deformation often results from a combination of mechanical loading, thermal transient cycles and thermal gradients. Unfortunately, even with this knowledge of in–situ conditions, it is common practice to base a structural analysis and design on constitutive equations and damage models developed from isothermally–generated data bases. Model characterization typically involves performing a series of isothermal tests over the temperature range of interest; from these tests, material parameters are characterized as functions of temperature. This approach furnishes the mathematical model with a "non–isothermal flavor", but unfortunately, many of the subtle, yet significant, material responses which are thermomechanically path–dependent are not properly represented or "built into" the model. Thus, an obvious question arises as to whether these isothermally developed equations and models are capable of predicting thermomechanical (in–situ) deformation.

In addition to this challenge, thermomechanical constitutive modeling is further complicated when the material of interest is subject to metallurgical instabilities. One form of such an instability transpires in solid solutions where solute atoms (such as carbon and nitrogen) are especially mobile and free to

diffuse through the parent lattice. Once diffusion has occurred, a new microstructural phase is formed. This new phase often precipitates at locations in the vicinity of mobile dislocations, where their presence restricts subsequent movements. The resulting phenomenological behavior is characterized by extensive material hardening, and is often referred to as dynamic strain aging [1].

With these specific problems in mind, a series of closely controlled thermomechanical deformation tests were conducted on the nickel–base superalloy Hastelloy Alloy X. Hastelloy Alloy X was chosen because of its common use in high temperature aerospace applications (i.e., as combustor liners for aircraft gas turbine engines), and because it exhibits strong temperature–dependent dynamic strain aging effects. Differences existing between isothermal and thermomechanical material behavior are noted and analyzed on the basis of both phenomenological and microstructural observations. These two forms of analysis are then coupled to explain several unique phenomenological trends observed under thermomechanical conditions.

Upon understanding the microstructural physics (leading to the unique thermomechanical trends), greatest benefit can be gained by modeling the instabilities, and their effects in a macroscopic constitutive model. Therefore, an existing thermoviscoplastic constitutive model [2,3] is introduced and extended to qualitatively predict the observed trends. This ability is gained by introducing an additional internal state variable to reflect the temperature path dependent effects of dynamic strain aging.

Through the use of advanced thermomechanical testing, material behavior which is more representative of that found in application can be studied and analyzed. This "true" thermomechanical data can then be used to guide the structuring of mathematical deformation models, in hopes of better assessing the damage, and ultimately, the life of a component.

CHAPTER 2

HASTELLOY ALLOY X : A SELECTED REVIEW OF HIGH TEMPERATURE PHENOMENOLOGICAL AND METALLURGICAL BEHAVIOR

2.1 Introduction

The superalloy Hastelloy Alloy X, hereafter referred to as Hastelloy X, exhibits many material characteristics that are desirable for high temperature energy system components. Thus, it has been the focus of many high temperature experimental investigations and is widely used in the aerospace and nuclear industries. Hastelloy X is a solid solution strengthened nickel–based superalloy, with exceptionally good corrosion and oxidation resistance at temperatures up to 1150°C (2100°F). It derives most of its solution strengthening from molybdenum, with minor contributions from cobalt and tungsten. Hastelloy X exhibits significant microstructural changes as a result of both static and dynamic thermal aging. These microstructural changes result in phenomenological features such as a ductility minimum and a strain aging peak. Because this material exhibits these complex microstructural changes under service condition temperatures, it is important to understand their effects on the macroscopic behavior under both isothermal and thermomechanical loadings.

This chapter presents an annotative review of publications concerned with the phenomenological and metallurgical behavior of Hastelloy X pertaining to the major interests of this study.

2.2 Phenomenological Aspects: Deformation, Fatigue, Life

One of the first comprehensive studies conducted on Hastelloy X was guided by Glasier at Aerojet General Corporation under an Atomic Energy Commission/National Aeronautics Space and Administration contract through the mid sixties and was documented in a final report in 1968 [4]. In this work a literature survey and testing program were initiated to obtain pertinent information on Hastelloy X in the range of –252°C (–423°F) to 982°C (1800°F). This was done in support of the Phoebus 2 Rocket Nozzle Program. Individual test data as well as statistical analyses were reported on the tensile properties (elastic modulus, yield strength and ultimate strength) of forgings, strip stock, weldments and brazements. An extensive database of physical properties over the full working temperature range was developed including thermal expansion, thermal diffusivity (from which thermal conductivity was calculated), specific heat, density and Poisson's ratio. Mechanical properties of bearing strength, compressive strength, shear strength, low cycle fatigue and thermal cycling were also presented. In addition, fabrication and manufacturing processes were discussed along with a metallurgical analysis of thermal treatments and processing. As the spectrum of the investigation was so broad, the detailed conclusions of this study will not be repeated herein. The database accumulated in this research created a solid foundation for subsequent investigators.

As Hastelloy X is of interest in high temperature applications, the need for low cycle thermal fatigue characteristics is essential. In 1969, Carden et al [5] examined the effects of structural geometry and temperature field in an attempt to simulate the behavior of rocket nozzle coolant tubes. This work was then followed up by a limited experimental program initiated by Carden and Slade [6] to examine the material behavior under conditions where the temperature and displacement could be controlled and measured. High strain range, low cycle fatigue tests were conducted in argon, along with a select few in air. Both isothermal and thermomechanical tests were performed to study the effects of temperature, cycle frequency and temperature–load phasing. Special attention was given to the minimum ductility that Hastelloy X experiences at or near 705°C (1300°F). It was found from earlier work by Carden et al [5] that high temperature exposure time influenced both the onset of buckling of the coolant tubes and their cyclic life, but it was concluded in this work that strain rate (crosshead speed) did not have a significant effect on either the tensile strength or true strain at fracture. The strain hardening exponent was found to vary from 0.35 to 0.18 for monotonic tensile loadings from room temperature to 650°C (1200°F). It then dropped to 0.04 to 0.02 from 760°C (1400°F) to 1095°C (2000°F) respectively. Some specimens experienced severe geometric distortion, such as specimen bulging that accumulated throughout the course of the test. The most noticeable occurrence of this cyclic instability was during an out–of–phase (maximum temperature and maximum compressive stress coincide, minimum temperature and maximum tensile stress coincide during cycle) test from 708°C (1300°F) to 980°C (1800°F). This phenomenon, referred to as barrelling by subsequent investigators, was not addressed further by Carden and

Slade than to say that conditions which lead to this type of progressive instability under thermal cycling are understood as conditions that allow local strain concentrations to develop. The authors conclude by citing McClintock and Argon [7] that the cyclic instability (i.e. barrelling) was not a consequence of the development of a tensile or compressive mean stress associated with out–of–phase or in–phase thermomechanical strain controlled tests, respectively. It was determined that the high temperature fatigue behavior could be adequately predicted by the tensile data and the method of universal slopes. Lastly, the thermomechanical fatigue test results showed reasonable agreement to isothermal behavior when the isothermal test used for comparison was one which was conducted at a temperature comparable to the maximum temperature of the cyclic test. In other words, thermomechanical fatigue behavior from 700°C (1300°F) to 980°C (1800°F) compared well with isothermal behavior at 980°C (1800°F). This observation has since been contradicted by further research that will be discussed later in complete detail.

Between July, 1970 and April, 1972 an extensive low cycle fatigue experimental program was conducted on Hastelloy X at Battelle Columbus Laboratories. This work was published in several smaller documents and then eventually in 1976 in a single complete document by Jaske et al [8] under the direction of NASA Lewis Research Center. The program was designed to experimentally evaluate the low cycle fatigue behavior in both hydrogen and air at temperatures from 540°C to 870°C (1000–1600°F). A strain rate of 10^{-3} s^{-1} was selected as being a prototypical test rate; relatively high axial strain ranges were investigated including 1.5, 3.0 and 5.0 percent. All tests were conducted under compressive strain cycling with constant strain–controlled amplitude. In

this investigation, heat–to–heat variations (chemical composition) were shown to affect behavior. As ductility varied from heat to heat, the fatigue life was found to vary in a directly proportional manner. As may be expected, these variations resulted in more pronounced effects as the strain range increased and also in the temperature regime where hardening was significant. Serrated yielding or jerky flow was exhibited during tensile tests at 540°C (1000°F); this is often associated with mechanical aspects of the Portevin–LeChatelier Effect and negative strain rate sensitivity. When compressive hold times were introduced at 760°C (1400°F) and 871°C (1600°F), a 15% to 20% increase in stress range (when compared to a test without a hold period) was realized. These specimens failed prematurely due to the development of a cyclic deformation instability which resulted in specimen necking. The relation of this increased stress range to the cyclic instability was not explained due to the limited experimental study of hold–time fatigue.

Up until this time, most investigators had emphasized experimental programs designed to generate low cycle fatigue data for Hastelloy X under relatively high strain ranges ($\epsilon \geq 1.0\%$) in environments other than air. Very little work had been done on low strain range low cycle fatigue in air until that of Seavers' in 1979 [9]. Here, tests were performed in the low total strain range ($\epsilon \leq 0.9\%$) longer life (1,000 to 10,000 cycles) regime. Effects of long hold periods under these low strains were also investigated. One temperature given special attention (as with Carden and Slade) was 705°C (1300°F). Repeated observations revealed that Hastelloy X underwent a thermal aging reaction after long–time exposures to this temperature which resulted in minimum room temperature tensile ductility. It was found that Hastelloy X experienced a

substantial tension hold time effect at the temperature of 705°C (1300°F) where the life reduction was most pronounced in the low strain range regime. Compression hold time effects were somewhat inconclusive. Virgin material tended to exhibit continuous cyclic strain hardening behavior plateauing shortly before crack initiation, whereas material aged (at 705°C) for 2500 hours before testing exhibited a somewhat stable cyclic stress response. Coffin's frequency modified fatigue equation, Ostergren's damage function and strain range partitioning were all addressed as predictive methods for life extrapolation purposes. All three were recommended as reasonable methods for correlating Hastelloy X low cycle fatigue data.

An extensive characterization of advanced time–temperature constitutive models to experimental data on Hastelloy X was done by Walker [10] in 1981. Three models were selected as being most appropriate for describing the material behavior of Hastelloy X; these models were 1) Walker's functional theory [11], 2) Miller's theory [12], and 3) Krieg, Swearengen and Rohde's theory [13]. Dissipation of inelastic work into heat was calculated for a test conducted at 982°C (1800°F) with ± 0.6% strain at a strain rate of 3.87×10^{-3} s^{-1}. This revealed a rise in temperature at the center of the specimen of approximately 0.8°C (1.4°F); therefore, it was concluded that the effect of inelastic dissipation of work into heat could be neglected in the data reduction. The following tests were conducted on uniaxial bar specimens: a) fully reversed cyclic stress–strain tests with various strain amplitudes over temperatures ranging from 425°C (800°F) to 980°C (1800°F); b) various creep tests initiated from several points on steady state hysteresis loops; c) various stress relaxation tests starting from zero initial strain values on steady state hysteresis loops. Hastelloy X exhibited

hysteresis loops that were asymmetric with respect to all temperatures with material being stronger in compression than in tension and with asymmetry increasing with temperature. An inverse strain rate sensitivity was present at 427°C (800°F) and 537°C (1000°F), but changed to a normal strain rate sensitivity for temperatures above 648°C (1200°F). Steady state hysteresis loops revealed that the yield stress increased from 427°C (800°F) to 537°C (1000°F) and then decreased from 537°C (1000°F) to 648°C (1200°F) and continued to decrease as temperature increased. In general, the calibrated constitutive models were adequate in predicting isothermal uniaxial response, but some difficulty was found in handling the inverse strain rate sensitivity. Relatively poor accuracy was obtained when the viscoplastic theories were used to predict uniaxial thermomechanical behavior of Hastelloy X. This inadequacy was in part due to the inability of state variables to change with temperature during elastic excursions in a thermomechanical simulation.

Hastelloy X is one of the materials that has received a significant amount of attention for use in high temperature gas–cooled reactor (HTGR) applications. The extensive HTGR program at Oak Ridge National Laboratories has produced a significant amount of data on Hastelloy X. A report by McCoy and King [14] extended the database with particular emphasis on ductility degradation during creep and aging of both base metal and weldments. The tests were conducted in both inert gas and impure helium environments. The impure helium environment was found to be carburizing with the kinetics of the process becoming rapid above 800°C (1470°F). The predominant effect of aging was the reduction of ductility at ambient temperature in both environments with the reduction being larger in the HTGR helium environment, and larger for

weldments than for base metals. Room temperature impact energies were found to be drastically reduced on samples aged in inert gas at 704°C (1300°F) and 871°C (1600°F). Creep tests did not reveal a measurable difference in creep rates and creep strengths due to heat variations, test environments (air vs. HTGR helium), aging or welding.

Multiaxial high temperature fatigue data is quite limited for all materials including Hastelloy X due to the complexities and difficulties involved with closely controlled multiaxial tests. A three year experimental program devoted to biaxial low cycle fatigue experiments on Hastelloy X was conducted by Jordan [15] with the quest of selecting the most appropriate fatigue failure parameters for existing life theories. Tests included isothermal fatigue at room temperature and 649°C (1200°F) for both proportional and non–proportional loading. An extensive description of the test hardware and its development was included, as this was a substantial portion of the total effort. Multiaxial fatigue life was found to be a function of strain amplitude and weakly dependent upon straining path. Strain rate and non–proportional loading effects did not significantly influence the fatigue life. The cracking mode switched from primarily cracking on the maximum shear planes at room temperature to cracking primarily on the maximum normal strain planes at 649°C (1200°F). This was most likely due to influencing oxidation effects at the hotter temperature. It was concluded that the most convenient theory for predicting multiaxial fatigue life at elevated temperatures was the octahedral shear stress theory, whereas the octahedral shear strain theory was more convenient for room temperature tests.

It has been well documented throughout the years that elevated–temperature components subjected to periodic thermal transients are subject to time dependent fatigue behavior. This time dependent fatigue or creep–fatigue interaction which occurs at temperatures within the creep range results in a decrease in fatigue life with increasing hold time or decreasing frequency. Brinkman's paper on high–temperature time–dependent fatigue [16] puts forth a critical review of the efforts aimed at obtaining a database with emphasis on understanding factors affecting creep–fatigue damage. Factors such as the effects of creep–induced intergranular cavitation, mean stress, material condition and environment were addressed for several alloys including Hastelloy X. Tests conducted on Hastelloy X at 760°C (1400°F) exhibited a decrease in fatigue life from both tensile and compressive hold periods. The deleterious effects of the compressive hold times were explained by the development of mean tensile stresses under low strain range conditions. Brinkman speculated that metallographic examination of specimens subjected to tensile hold periods in excess of 30 minutes within the range of 704°C–760°C (1300°F–1400°F) would reveal intergranular cavitation and crack propagation, particularly for tests conducted at low strain ranges. Heat–to–heat or minor chemical variations were qualitatively identified as influential factors although a quantitative assessment of their affects on time–dependent fatigue properties was not made due to limited information addressing the subject. Thermal aging, particularly under those conditions which lead to metallurgical instability, was also cited as having an influence on time–dependent fatigue life. Several extrapolating cycle–life models were discussed in terms of their respective strengths and shortcomings.

It was concluded that no model currently available was superior in universally predicting cyclic life, particularly at low strain ranges with long creep periods.

Work performed by McKoy and King [14] discussed earlier in this chapter revealed that Hastelloy X suffers a loss in ductility when subjected to moderate aging periods (up to 20,000 hours). A follow–up program was conducted by McKoy [17] to further characterize thermal aging effects and how they affect the service life of components. Both base metal and transverse weldments of Hastelloy X were aged up to 53,000 hours at 593°C (1100°F), 704°C (1300°F) and 871°C (1600°F) in an impure helium environment. Half of the samples were subjected to tensile tests at room temperature while the other half were subjected to long term creep tests at their respective aging temperatures. The latter half of the program (creep test portion) was still in progress at the time of the report but it was reported that general trends had thus far indicated that the aged material was weaker than the unaged material. It was postulated that the massive amounts of carbide precipitates (formed as a result of 53,000 hours of aging) caused a depletion of the solid solution strengthening elements from the matrix, hence, the resulting reduction in creep strength. The most significant effect of the extended aging period was the resulting change in strength. After 20,000 hours, the strength was a maximum due to aging at 704°C (1300°F) and the reduction in fracture strain was a maximum as a result of aging at 871°C (1600°F). In contrast, after 53,000 hours of aging both the 704°C (1300°F) and 871°C (1600°F) samples experienced overaging effects and both the largest increase in strength and decrease in fracture strain occurred in the sample aged at 593°C (1100°F).

Up until 1985, very little if any experiments had been performed on Hastelloy X to determine if thermomechanical loading could produce phenomenological behaviors not found under isothermal conditions. As discussed earlier, Carden and Slade [6] in 1969 performed an extremely limited number of thermomechanical tests which did not exhibit any form of unique behavior when compared to isothermal tests, at least on the basis of fatigue life. One explanation for this may be that the temperature ranges at which these tests were conducted were not the temperature ranges which lend themselves to thermomechanical uniqueness. Bartolotta published a report in 1985 [18] which set out to determine if Hastelloy X exhibited thermomechanical history dependence and if so, the implications this would have on constitutive model development. This was accomplished by performing a series of simple stepwise non–isothermal tests and comparing behavioral trends to those of isothermal tests. Experimental evidence revealed that Hastelloy X experienced a hardening behavior which was highly dependent upon thermomechanical path. Thus, one conclusion was that isothermal cyclic–hardening data would not be sufficient to predict hardening behavior under general non–isothermal conditions. The need for viscoplastic constitutive models to be formulated under the influence of a thermomechanical database was also expressed. A thermoviscoplastic mathematical representation was postulated in a general sense which qualitatively accounted for the thermomechanical path dependence observed from the simple stepwise non–isothermal tests.

The literature available on Hastelloy X concerned with phenomenological deformation aspects leads up quite well to the work performed by Robinson and Bartolotta [19]. This work was performed to further specify a thermoviscoplastic constitutive relationship that qualitatively accounted for the thermal history dependence observed by Bartolotta [18]. In an attempt to assess the importance of accounting for thermomechanical path dependence, two qualitative models were proposed and evaluated for several test conditions. The first model, which was formulated entirely on the basis of isothermal data, was found to be inadequate for predicting cyclic hardening behavior under general thermomechanical conditions. The second model, which was formulated to reflect thermomechanical path dependence, was found to be qualitatively capable of predicting the cyclic hardening behavior observed in the previously cited simple non–isothermal tests. Using predicted results as a basis for comparison of the two qualitative models, it was concluded that non–conservative lifetime predictions could be obtained when an isothermally formulated model was used to predict deformation under simple thermomechanical loading conditions.

2.3 Metallurgical Aspects: Aging Kinetics, Phases, Stability

In order to have a well founded understanding of the high temperature macrostructural behavior of Hastelloy X, it is essential to have at least a working knowledge of the microstructural changes occurring as influenced by time, temperature, environment and load. It is not to claim here that metallurgical changes influence macroscopic behavior for all materials, but it is well established that Hastelloy X undergoes microstructural changes which significantly influence its mechanical behavior. Therefore, it is necessary to understand these metallurgical instabilities if one is to properly asses their influence on the phenomenological behavior.

The precipitation of a carbide phase is one significant change Hastelloy X undergoes as a result of exposure to high temperatures. Kotval and Hatwell [20] address the topic of discontinuous precipitation of $M_{23}C_6$ carbides in nickel–based superalloys. This metallurgical phenomenon involves the migration of $M_{23}C_6$ carbides to grain boundaries at high temperatures. This is quite common in Hastelloy X and other nickel–based superalloys and is responsible for occurrences such as ductility reductions and brittle intergranular modes of fracture. A significant review of previous work concerning this topic was presented. It was noted that Lewis and Hattersley [21] suggested that the type of $M_{23}C_6$ precipitation observed in Ni–Cr austenites (such as Hastelloy X) represented the early stages of discontinuous precipitation. Tu and Turnbull [22] were cited as suggesting that the difference in surface free energies on opposite sides of the $M_{23}C_6$ plates was the driving force for grain boundary migration. Also, observations taken from Singhal and Martin [23] imply that the grain boundary provides a diffusion short circuit for the substitutional solute atoms

(principally chromium) which assist the preferential growth of the $M_{23}C_6$ plate in contact with the grain boundary. Kotval and Hatwell's main objective was to observe conditions of extensive discontinuous precipitation of $M_{23}C_6$ carbides and address their effects on mechanical properties. It was concluded that discontinuous precipitation was much more pronounced when a high degree of solute supersaturation existed. X–ray diffraction patterns of a discontinuous precipitation cell illustrated that the $M_{23}C_6$ carbide phase and the γ' phase (a well ordered fcc phase occurring throughout the matrix after normal commercial heat treatment) have close crystallographic relationship with the parent matrix. Discontinuous precipitation cells were found to have no apparent effect on material strength, but high temperature ductility was found to decrease markedly. The investigation led to the conclusion that the morphology of discontinuous precipitation cells at grain boundaries was highly conducive to the initiation of cracks which in turn resulted in premature grain boundary failure.

Throughout the literature addressing phenomenological behavior, a ductility minimum was consistently observed and emphasized in experimental programs for obvious reasons. Arkoosh and Fiore [24] published a report investigating the elevated temperature ductility minimum in Hastelloy X strictly from a metallurgical viewpoint. A generalized model proposed by Rhines and Wray [25,26,27], commonly used to explain this so called "midrange ductility dip" was shown to be inappropriate for Hastelloy X due to the absence of recrystallization as temperatures rise just above the ductility minimum regime. Specimens were heat treated and then subjected to elevated temperature tensile tests above, at and below the minimum ductility temperature [760°C (1400°F), 649°C (1200°F) and 593°C (1100°F) respectively]. Metallographic comparisons

were made between those specimens and specimens subjected to the same heat treatment without the subsequent tensile tests. There was no evidence of recrystallization in the stressed or unstressed samples even at the temperature of 760°C (1400°F). A fine secondary carbide was found to have precipitated intragranularly and at grain and twin boundaries of stressed samples tested at 649°C (1200°F) and 760°C (1400°F), but the unstressed samples showed very little secondary precipitation. This implied that a significant amount of deformation–assisted precipitation was occurring as a result of the dislocations' powerful affect on lowering the nucleation barrier [28] and becoming the preferred carbide nucleation sites. At temperatures higher than the minimum ductility temperature these carbides were found to loose their effectiveness as dislocation pinners due to an overaging or ripening effect. It was further cited [29] that at high temperatures the precipitates may begin to redissolve resulting in the dissipation of mechanical energy as the dislocations become free and vibrate. The angular position of the $\langle 111 \rangle$ diffraction peak for the unstressed samples was found to be approximately 19.8°, whereas the stressed samples had their $\langle 111 \rangle$ peak at angles greater than 20.3°. The unstressed samples displayed an interplanar atomic spacing (based on the $\langle 111 \rangle$ electron diffraction pattern) which was independent of temperature (constant for all three test temperatures). In contrast, the stressed samples' interplanar atomic spacing was found to be a function of temperature and consistently less than that found in the unstressed samples. The key metallographic observation was noted as being that in the 760°C (1400°F) stressed specimens, grains were much more elongated and exhibited extensive intragranular deformation. It was postulated that significant carbide precipitation occurring at temperatures above the minimum ductility

temperature was leading to extensive solute depletion and subsequently weakening the solid solution matrix. This allowed the weakened matrix to deform intragranularly as well as by grain boundary shear, permitting extensive plastic flow which in turn prevented intergranular cracks from forming a continuous network. Hence, a post–dip ductility increase was realized as a result of the bulk deformation increase.

Hastelloy X was identified before as a material of interest for HTGR applications. These reactor systems contain many metallic components that must operate for extremely long periods (up to 40 years) at elevated temperatures. When this type of performance is demanded from a component, thermal stability becomes a significant issue. Lai's report [30] on the thermal stability of Hastelloy X seemed to be the most referenced piece of literature addressing this topic. The paper presented results of an investigation into the aging kinetics, microstructural changes and changes in room temperature impact toughness as a result of up to 10,000 hours of aging. The aging was performed at temperatures of 538°C, 649°C, 760°C and 871°C (1000°F, 1200°F, 1400°F and 1600°F respectively) and all subsequent testing was performed after the removal of the oxide scale and the surface layers affected by surface oxidation. Impact tests were conducted on standard Charpy V–notch specimens in accordance with the requirements of ASTM E23–72 and hardness was measured in a Rockwell hardness tester. All microstructural characterization was performed using optical metallographic techniques and X–ray diffraction measurements made on extracted phases. The microstructure in the solution annealed condition was found to contain a coarse precipitate phase identified as M_6C carbide; this carbide was referred to as the primary carbide. A secondary carbide phase

identified as M_6C' (referred to as $M_{23}C_6$ by other investigators) was concluded to be the carbide precipitated during aging. This phase was found to be intragranularly dispersed throughout the matrix in all specimens aged at 649°C to 871°C (1200°F to 1600°F), but it was present only at the grain boundaries for specimens aged at 538°C (1000°F). A hardness increase was observed for the specimens aged at 649°C and 760°C (1200°F and 1400°F) whereas the 538°C (1000°F) specimen did not reveal a noticeable change in hardness. A slight hardness increase was observed for the 871°C (1600°F) specimen followed by overaging and a decrease in hardness after 4,000 hours. A significant reduction in toughness was realized at all aging temperatures with the major portion of the reduction occurring in the first 100 hours of aging for the 649°C, 760°C and 871°C (1200°F, 1400°F and 1600°F respectively) specimens. In contrast, the specimen aged at 538°C (1000°F) experienced a continuing drop of impact toughness with aging time. This was claimed to have been associated with the continuous formation of M_6C' carbides at the grain boundaries. All reductions in room temperature impact toughness were associated with the precipitation of M_6C' carbides, whether intergranularly or intragranularly. Finally, it was noted that in addition to carbide precipitation, precipitation of a σ phase was identified after aging for 10,000 hours at 760°C (1400°F) and a μ phase after 1,000 hours at 871°C (1600°F).

As is the case for most research programs, improvements in both equipment and methodology over time can lead to more conclusive investigations and a better understanding of both previously unexplainable and possibly non–detectable occurrences. It is noted [31] that inherent limitations of optical metallographic observations and X–ray diffraction techniques, such as those

employed by Lai in 1978, could lead to inconclusive results concerning the metallurgical structure/property relationship, especially in the case of a multi–phase complex superalloy [32] such as Hastelloy X. Therefore, in an effort to avoid these limitations, an investigation into the long term aging characteristics of Hastelloy X was performed by Tawancy [31] where the technique of thin–foil transmission electron microscopy and electron diffraction was employed. Since metallographic and tensile specimens were aged for up to 16,000 hours at 538°C, 649°C, 760°C and 871°C (1000°F, 1200°F, 1400°F and 1600°F respectively), many of the same features (metallurgical and mechanical) observed by Lai [30] were also reported by Tawancy. Only those features shedding new light on or contradicting previous observations of the aging characteristics will be presented herein. Hastelloy X in the annealed condition was typically found to contain a small amount of second–phase particles identified by both X–ray and electron diffraction to be a fcc structured molybdenum–rich carbide of the form M_6C. The annealed condition also revealed a relatively high dislocation density at the carbide–matrix interface. It was postulated that these dislocations formed during rapid cooling as a result of the thermal coefficient of expansion mismatch between the carbide and the matrix. These "inherent" dislocations as well as subsequently formed dislocations more randomly dispersed throughout the matrix, were found to serve as carbide precipitation sites during aging at elevated temperatures. The molybdenum–rich M_6C primary carbide was found to have promoted the precipitation of a molybdenum–rich μ phase. Several observations were made on specimens aged at 538°C (1000°F) which were not previously detected with the use of optical metallography. Transmission electron microscopy revealed fine

precipitates not only at the grain boundaries (as Lai had hypothesized) but also in the matrix after 16,000 hours of aging. Electron diffraction patterns indicated that the precipitates had a fcc structure with a lattice constant three times that of the matrix. Characteristic identification revealed these precipitates as chromium–rich $M_{23}C_6$ carbides. The $M_{23}C_6$ carbides precipitating in the matrix were found primarily at pre–existing matrix dislocations and at the dislocations around the primary carbides which had resulted from the thermal expansion mismatch. Another precipitate was found only at the grain boundaries and in comparatively less amounts than the $M_{23}C_6$ carbide. This was identified as the fcc structured molybdenum–rich $M_{12}C$ carbide. Early stages of aging at 650°C (1200°F) produced microstructures reported as being similar to those found after 16,000 hours of aging at 538°C (1000°F). However, after 1,000 hours of aging at 650°C (1200°F), the matrix and grain boundaries were found to contain a tetragonal crystal structured phase with a platelet morphology intermixed with the $M_{23}C_6$ carbides. After further investigation, the phase was identified as a chromium–iron–rich σ phase. It was cited [33] that a σ phase was promoted by the pre–existence of a phase enriched with a σ–forming element; in this case the σ–forming element was the chromium in the chromium–rich carbide phase $M_{23}C_6$. The density of the σ phase was shown to increase as aging continued and was claimed to be partially responsible (in its later stages) for the hardening, strengthening and reduction in room temperature ductility realized from prolonged aging at 650°C (1200°F). This was explained by noting that σ phase, especially in platelet morphology, was known to be extremely hard and brittle at room temperature [34]. Microstructural observations made of samples aged up to approximately 8,000 hours at 760°C (1400°F) revealed phase changes similar to

those described for the 650°C (1200°F) samples. However, at aging periods of 8,000 hours and greater, the σ phase was shown to have undergone considerable growth and had evolved into a blocky–type of morphology. It was concluded that growth of the σ phase

in later stages of aging could account for the commonly observed overaging at this temperature. Specimens aged 100 hours at

871°C (1600°F) revealed precipitate phases of $M_{23}C_6$ carbide, molybdenum–rich $M_{12}C$ carbide and a hexagonally structured molybdenum–rich μ phase at the grain boundaries and to a lesser degree in the matrix. As was described with the σ phase at 650°C (1200°F), the molybdenum–rich μ phase was promoted by the pre–existence of a molybdenum–rich phase such as the $M_{12}C$ carbide or possibly even the original M_6C phase. This was supported by noting that the μ phase was nearly always found to be connected to either a $M_{12}C$ carbide at the grain boundaries or to a M_6C carbide in the matrix. The overall behavior of the μ phase was described much in the same way as that of the σ phase, in that the μ phase caused an embrittling effect at room temperature and eventual coarsening of the μ phase in the later stages of aging could explain the observed overaging effect experienced at 871°C (1600°F).

As was the case with the phenomenological aspects of Hastelloy X, the literature addressing the metallurgical aspects of Hastelloy X leads up quite well to a report published in 1987 by Miner et al [35] discussing the cyclic hardening mechanisms in Hastelloy X. Transmission electron microscopy (TEM) and electron diffraction techniques were used to examine specimens that had been subjected to isothermal cycling at temperatures of 93°C, 538°C and 871°C (200°F, 1000°F and 1600°F respectively). Many of the same microstructural

phases noted in the past literature were also observed here. A cyclic hardening peak, often referred to as a dynamic strain aging peak, was found to occur at approximately 650°C (1200°F). Optical microscopy revealed relatively large M_6C carbides widely and randomly dispersed throughout the "as received" Hastelloy X. While testing at 93°C (200°F) had essentially no effect on the M_6C carbides, considerable dissolution was evident after only 1000 cycles. In the specimen tested at the intermediate temperature 538°C (1000°F), dissolution of the original M_6C was less apparent, but TEM examination showed that new extremely small $M_{23}C_6$ carbides were precipitated within the grains. The $M_{23}C_6$ carbides were not found at all in the low temperature specimens and largely found reprecipitated at grain boundaries in the 871°C (1600°F) specimen.

Examination by TEM also showed a much higher dislocation density in the 538°C (1000°F) specimen than in the other specimens. In the 93°C (200°F) test specimen, the relatively low dislocation density is compatible with the slight cyclic hardening observed in that temperature regime. In the 871°C (1600°F) specimen, recovery processes (i.e. climb) competing with cyclic hardening were evidenced by the formation of subcells with interiors of low dislocation density.

Although these observations reflect some features of classical dynamic strain aging, with the fine $M_{23}C_6$ carbides precipitating at dislocation cites and causing strengthening by pinning mobile dislocations, other observations suggest a considerably more complicated hardening process. For example, the strengthening did not exhibit the degree of time dependence expected for a process controlled by diffusion of solutes; the strengthening appeared more dependent upon the number of cycles than time. A modified strain aging mechanism is suggested that would exhibit the cycle dependent, but little time

dependent, hardening observed at the intermediate temperature. Another oddity identified was the observation that the dense homogeneous dislocation structure found in the specimen cycled at 538°C (1000°F) did not seem to be consistent with the patchy–distribution of the precipitated $M_{23}C_6$ phase.

The publications selected for review in this chapter have answered many questions pertaining to the high temperature behavior of Hastelloy X, but in contrast, it can easily be stated that very little is understood about the true to life complex thermomechanical behavior of this multi–phase material. It is this author's hopes that the data and analysis presented for this investigation will add another piece to the possibly and quite probably infinite puzzle.

For the readers benefit and discretion, a more representative list of the literature available addressing experimental programs and various applications of Hastelloy X is included in APPENDIX A. As one will no doubt find, the amount and spectrum of both work and literature are extremely broad.

CHAPTER 3

MATERIAL AND EXPERIMENTAL DETAILS

3.1 Introduction

The main objectives and experimental details of this investigation are described within this chapter. The factors motivating this experimental study are also discussed. Special emphasis was placed on maintaining closely controlled test conditions. This was achieved through the development and refinement of several test parameters including specimen geometry, hardware, software, procedures and techniques. Once having established this mature set of experimental parameters, a straight–forward systematic approach used in conducting these complex thermomechanical deformation tests will be defined.

3.2 Motivational Factors and Objectives

As Chapter 2 concludes, Hastelloy X is a complex multi–phase material exhibiting several metallurgical and phenomenological features not fully understood. Combining this with the fact that Hastelloy X is currently of wide use in the aerospace and nuclear industries, one can see that further experimental investigation and analysis is warranted. More specifically, three major motivational factors dictated the objectives of this study. First, the isothermal cyclic hardening behavior [from room temperature to 982°C (1800°F)] of Hastelloy X has been shown to exhibit complex trends [36]. This behavior is

influenced by metallurgical instabilities which result in dynamic strain aging effects. A question naturally arises as to whether this complex behavior is present under "more realistic" thermomechanical conditions; and if so to what extent. Second, very little experimental thermomechanical data is available for Hastelloy X. As this material has been shown to be thermomechanically path dependent [18,19], some form of thermomechanical data should be considered during the development of mathematical models used to predict this material's viscoplastic behavior. Also, closely controlled thermomechanical experiments can be used to verify these models. Third, as a result of significant advances in experimental hardware and software, high temperature thermomechanical deformation experiments can now be performed to a degree of accuracy and control not previously possible. Taking these factors into consideration the main objectives of this investigation were formulated.

The primary objective is to perform a series of closely controlled uniaxial thermomechanical experiments in air where the temperature and mechanical strain are cyclicly in–phase or 180° out–of–phase. The temperature range of interest is from room to 1000°C (1832°F). Upon completion of these tests, both the data and specimens will be used to investigate several areas of interest. One main interest is to make a number of comparisons between isothermal and thermomechanical material behavior. These comparisons range from more general phenomenological material responses, such as overall hardening range and rate with respect to temperature regime, to more subtle behaviors, such as the inelastic strain for a given cycle. Upon establishing isothermal and thermomechanical material behavior patterns (similarities and differences), a microstructural analysis is performed to clarify and substantiate

these results. Through the use of both analyses, a description of the thermomechanical deformation will be formulated. A second main objective of this investigation, is to study the thermomechanical phenomenological trends with an emphasis on their relevancy to thermoviscoplastic constitutive modeling. An existing model [2,3,19] is then modified to qualitatively predict these trends.

3.3 Test Matrix

The test matrix is formulated to investigate the behavior of Hastelloy X over its full working temperature spectrum. Key features [i.e. the strain aging peak exhibited at approximately 600°C (1112°F)] are considered when determining individual test temperature ranges. A mechanical strain range of 0.6% is selected and maintained throughout all of the tests, regardless of temperature range. This range was used for comparable isothermal tests [36] and will enable direct comparisons between thermomechanical and isothermal behavior. The mechanical strain rate however is dependent upon the temperature rate and temperature range of each test. This is not considered a potential problem for subsequent comparisons with isothermal response as Hastelloy X is known to be relatively insensitive to small strain rate variations. Twelve different test conditions are investigated under strain and temperature control; these tests are summarized in Table 3.1. Eight tests (four in–phase and four out–of–phase) are conducted with temperature ranges of 200 C°(360°F).over a spectrum from 200°C (392°F) to 1000°C (1832°F). These tests are intended to show variations in thermomechanical trends as functions of different temperature regimes [i.e. how does thermomechanical behavior at the "relatively low" temperatures of 200°C to 400°C (392°F to 752°F) differ from the thermomechanical behavior at

PROPOSED TEST MATRIX

TEMPERATURE RANGE (Degrees C)

	200-400	400-600	600-800	800-1000	300-800	300-1000
IN PHASE	1	1	1	1	1	1
OUT OF PHASE	1	1	1	1	1	1

ALL TESTS WERE PERFORMED UNDER STRAIN CONTROL AT ± 0.3 % MECHANICAL STRAIN

A TRIANGULAR WAVEFORM WAS USED TO CONTROL BOTH STRAIN AND TEMPERATURE

Table 3.1 - Test Matrix

the "intermediate" temperatures of 400°C to 600°C (752°F to 1112°F), and so on]. The four remaining test conditions, those with relatively large temperature ranges, are conducted to investigate the effects of cycling completely through the known strain aging peak. This condition is considered to be more probable for components subjected to general thermomechanical loadings. It is important to clearly define the conditions imposed for "in–phase" and "out–of–phase" tests. Figure 3.1 illustrates the controlling parameters for an out–of–phase test and their phasing relationship. Here, two thermal strain ranges (small and large) are shown to emphasize the resulting possible forms of the total strain hysteresis loops. For this study, a test is defined to be in–phase when the maximum temperature coincides with the maximum positive mechanical strain, and the minimum temperature coincides with the maximum negative mechanical strain. The mechanical strain is defined as follows:

$$\epsilon_m = e_t - \epsilon_{th}$$

where e_t is the total strain and ϵ_{th} is the thermal strain component resulting from $\alpha\delta T$. In contrast, a test is defined to be out–of–phase (Figure 3.1) when the maximum temperature coincides with the maximum negative mechanical strain and the minimum temperature coincides with the maximum positive mechanical strain (i.e. temperature and strain waves are 180° out–of–phase). Thus, given that all the tests involve fully reversed ±0.3% mechanical strain, (independent of thermal strain), in–phase conditions result in tension during the "hot" portion of the cycle, and out–of–phase conditions result in tension during the "cold" end of the cycle. This is accomplished by pre–determining and accounting for the cyclic thermal strains over any given cyclic temperature range. This is discussed in greater detail when experimental procedures and techniques are addressed in

EXAMPLE OF OUT-OF-PHASE THERMOMECHANICAL TESTING

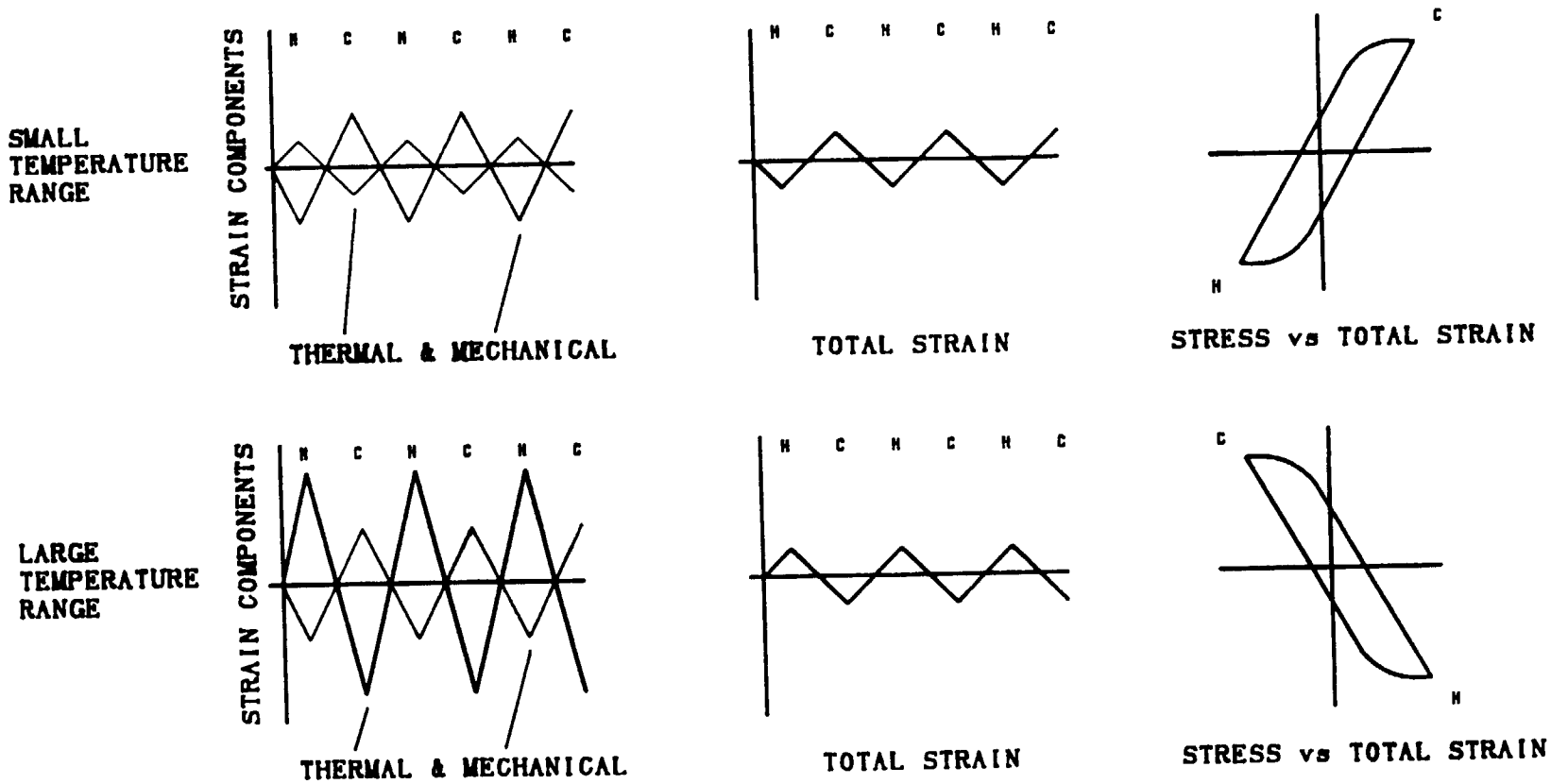

H => HOT END OF CYCLE C => COLD END OF CYCLE

Figure 3.1 - Out-Of-Phase Thermomechanical Testing

Section 3.7. As seen in Figure 3.1, a triangular wave form is used to control both the strain and temperature. This waveform was selected over a non–linear waveform for two major reasons. First, it is more easily interpreted during subsequent analyses, and second, it allows for more precise control of phasing between temperature and strain. The exact time per cycle (i.e. total strain rate) was not initially prescribed due to the variability of heating rate, cooling rate and phasing control. These parameters are interactively optimized with procedures and techniques to allow for both a high degree of control and a reasonable cycle period. Given this general test matrix, the experimental program began and continued as specimen design, control software, procedures and techniques were continuously refined. It was not the original intent of this experimental program to repeat tests for the sake of verifying repeatability, although in some cases, tests were repeated as a result of significant refinements.

3.4 Heat Information

The Hastelloy X specimens used in this study were fabricated from 19 mm (0.75 in.) diameter bar stock in 0.61 m (2.0 ft.) sections. This material was supplied and certified (heat ID #2G5161) by Universal–Cyclops Specialty Steel Division (UCSSD). The chemical composition was certified as conforming to Aerospace Material Specification (AMS) 5754H. Shown in Table 3.2 along with this specification is the chemical composition reported by UCSSD. Details of the material's solution heat treatment are as follows:

CHEMICAL COMPOSITION OF HASTELLOY ALLOY X*

	min#	max#	THIS HEAT
Carbon	0.05 -	0.15	0.069
Manganese	--	1.00	0.58
Silicon	--	1.00	0.48
Phosphorus	--	0.040	0.022
Sulfur	--	0.030	0.001
Chromium	20.50 -	23.00	21.11
Cobalt	0.50 -	2.50	1.72
Molybdenum	8.00 -	10.00	8.46
Tungsten	0.20 -	1.00	0.40
Iron	17.00 -	20.00	18.88
Boron	--	0.010	0.0040
Aluminum	--	0.50	0.06
Titanium	--	0.15	<0.02
Copper	--	0.50	0.09
Nickel	remainder		remainder

PERCENTAGES BY WEIGHT

* Hastelloy Alloy X is a registered trademark of the Cabot Corporation

\# Aerospace Material Specification AMS 5754H

Table 3.2 - Chemical Composition of Hastelloy X

(1) Bars are heated up to a temperature of 1175°C ±15°C (2150°F±25°F).

(2) Bars are held at this temperature for a time commensurate with their cross–sectional thickness but not less than 20 minutes.

(3)Bars are then cooled to room temperature at a rate equivalent to air cool or faster.

Other mechanical properties specific to this heat of Hastelloy X are given in Table 3.3.

3.5 Specimen Design

As previously mentioned, several experimental parameters were subject to change as a result of refining thermomechanical testing capabilities; specimen design was not excluded from this evolution. The initial specimen design employed for this study is shown in Figure 3.2 and will hereafter be referred to as specimen design #1. Specimen design #1 features a solid specimen, smooth shanks and a parallel working section of approximately 32 mm (1.25 in.). This specimen performed well for all in–phase experiments, although buckling was observed after approximately 500 cycles during the 800°C – 1000°C (1472°F to 1832°F) test. In contrast, a significant problem arose during out–of–phase tests involving temperatures greater than 600°C (1112°F), namely a cycle–by–cycle ratchetting phenomenon referred to as bulging or barrelling [6,37–41]. This geometric distortion was initiated after only a few hundred cycles and proceeded at an accelerated rate. With this changing cross–section, stress and strain measurements became highly unreliable. In order to collect reliable data under

ADDITIONAL PROPERTIES SPECIFIC TO THIS HEAT OF HASTELLOY ALLOY X[+]

HARDNESS: 159 / 170 BHN

GRAIN SIZE: 5 to 7

STRESS-RUPTURE PROPERTIES AT 815°C (1500°F):

APPLIED STRESS:	105 MPa (15000 psi)
STRESS-RUPTURE TIME:	54.8 hours
ELONGATION AFTER RUPTURE: MEASURED AT ROOM TEMPERATURE	99.2 percent

[+] All properties shown are in accordance with Aerospace Material Specification AMS 5754H

Table 3.3 - Additional Material Properties

SPECIMEN DESIGN # 1

THIS DESIGN FEATURES A SOLID SPICIMEN WITH A PARALLEL WORKING SECTION OF APPROXIMATELY 32 mm (1.25 in)

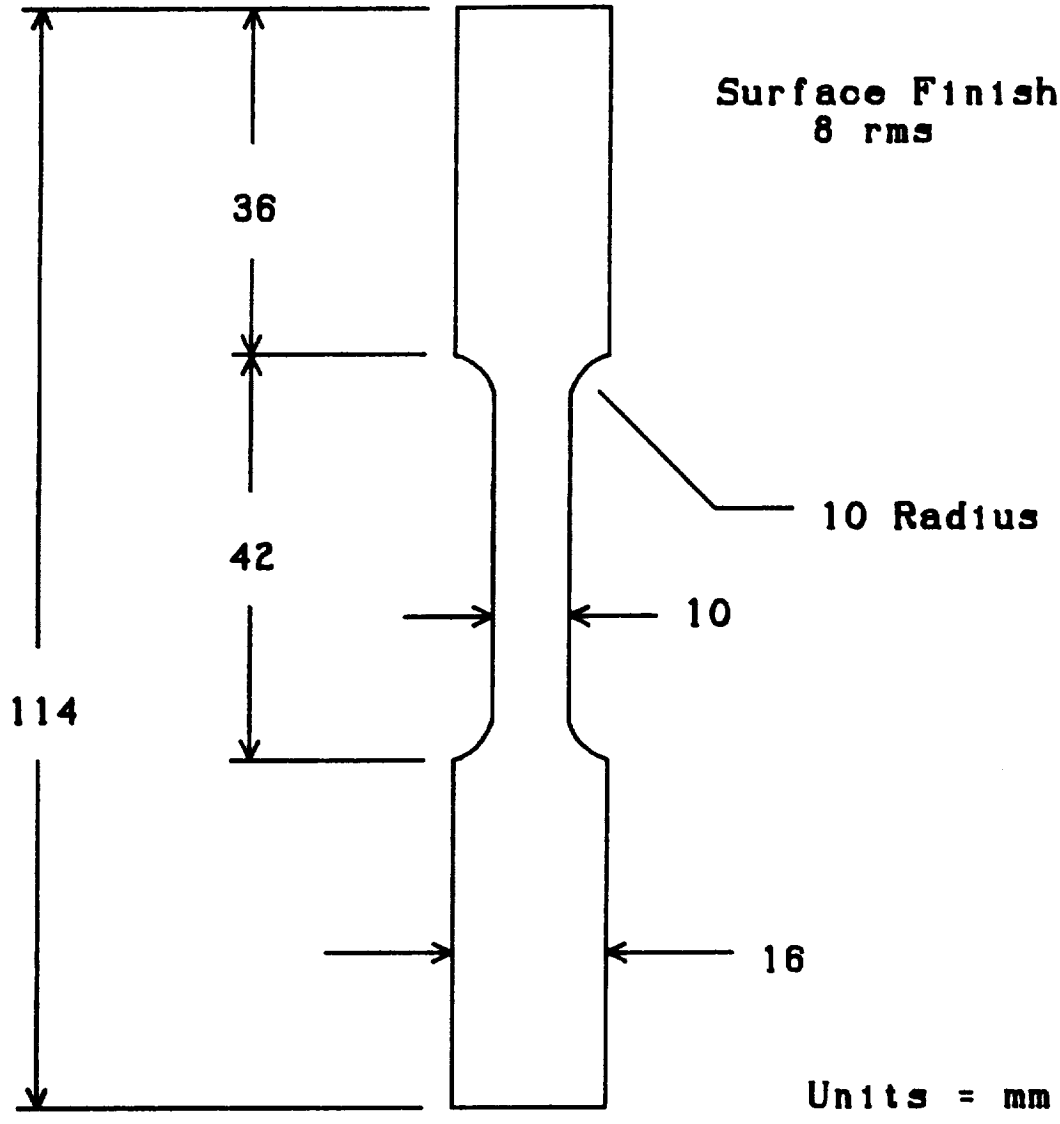

Figure 3.2 - Specimen Design # 1

upper–temperature out–of–phase conditions, it was necessary to solve or avoid this problem. Several months were devoted to identifying the cause and minimizing the effects of this phenomenon. Although that work is outside the scope of this paper, the findings had a major impact on several experimental aspects including specimen design. One finding having a direct impact on specimen design considerations is the following: dynamic thermal gradients (thermal gradients present during thermal cycling) played a significant role in promoting barrelling. Minimizing dynamic axial thermal gradients resulted in minimizing the barrelling, therefore, two major changes in specimen design were implemented to better accomplish this task. This new specimen design is pictured in Figure 3.3 and will hereafter be referred to as specimen design #2. Specimen design #2 features a thin walled tube specimen, smooth shanks, and an extended parallel working section of 51 mm (2 in.), approximately twice that of specimen design #1's. As compared with a solid specimen, the tube structure provides two major advantages, one, it allows the specimen to be heated and cooled at higher rates and two, its geometry inherently lowers the dynamic radial thermal gradients (although this quantity was never determined). The extended parallel working section of specimen design #2 provides enough axial length to fully accommodate the induction heater work coils used to heat the specimen (discussed in section 3.6.2). That is, the upper and lower coils do not "ride" upon the specimen's fillets and shoulders, as they did when positioned on specimen design #1; see Figure 3.4. By locating the induction heater work coils entirely within a section of constant geometry, the interpretation of coil adjustments (necessary to optimize the axial temperature profile) is greatly simplified. The topic of axial thermal profile optimization is further discussed in

SPECIMEN DESIGN # 2

THIS DESIGN FEATURES A THIN-WALLED TUBE SPECIMEN WITH A PARALLEL WORKING SECTION OF APPROXIMATELY 51 mm (2.0 in)

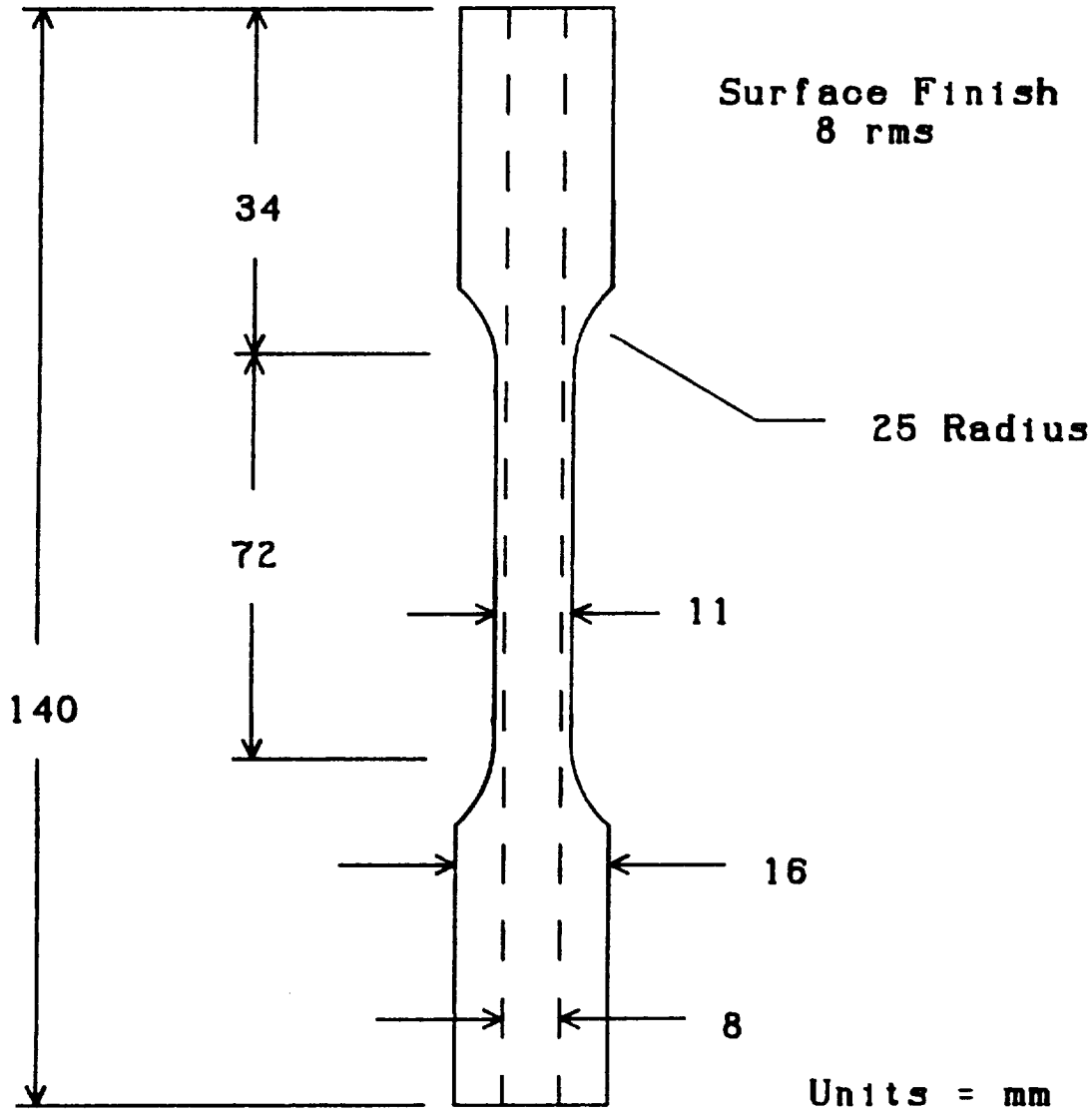

Figure 3.3 - Specimen Design # 2

SPECIMEN DESIGN #1 AND #2 SHOWN WITH INDUCTION COILS IN THEIR APPROPRIATE POSITIONS

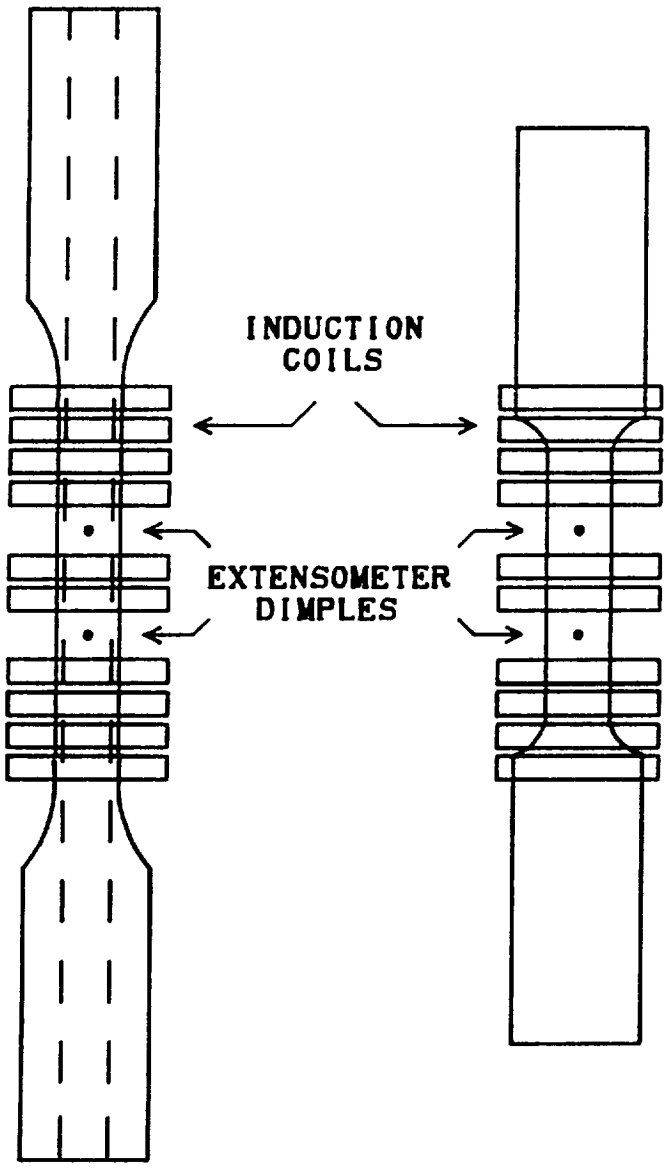

Figure 3.4 - Location of Induction Heater Coils

Section 3.7.2. As specimen design #2 aided in the control and minimization of barrelling, it was used for all out–of–phase experiments involving temperatures above 600° C (1112° F).

3.6 Experimental Equipment

3.6.1 General Comments

In axial–thermomechanical deformation experiments where the temperature is continuously changing throughout the cycle, thermal strains significantly contribute to the total axial strain, especially when large temperature ranges are traversed. This presents formidable difficulties with the control of total strain, temperature, and strain–temperature phasing. As this study addressed material deformation, and not fatigue life, it was important to significantly minimize the problems associated with these difficulties. The unique set of experimental hardware and software described below, combined with the proper test procedures, enabled this goal to be accomplished.

3.6.2 Hardware

All experiments conducted for this study were performed at the NASA Lewis High Temperature Fatigue and Structures Laboratory. A description of this facility can be found in reference [42]. An overall view of the test system used for these experiments is shown in Figure 3.5. This is a closed–loop electronic servo–hydraulic test system which features a two–post load frame. A ±222.4 N (±50 kip) capacity loadcell is integrally contained within the load frame crosshead, thus minimizing the length of the load train. This feature helps to maintain specimen stability under compressive loading. Another noteworthy

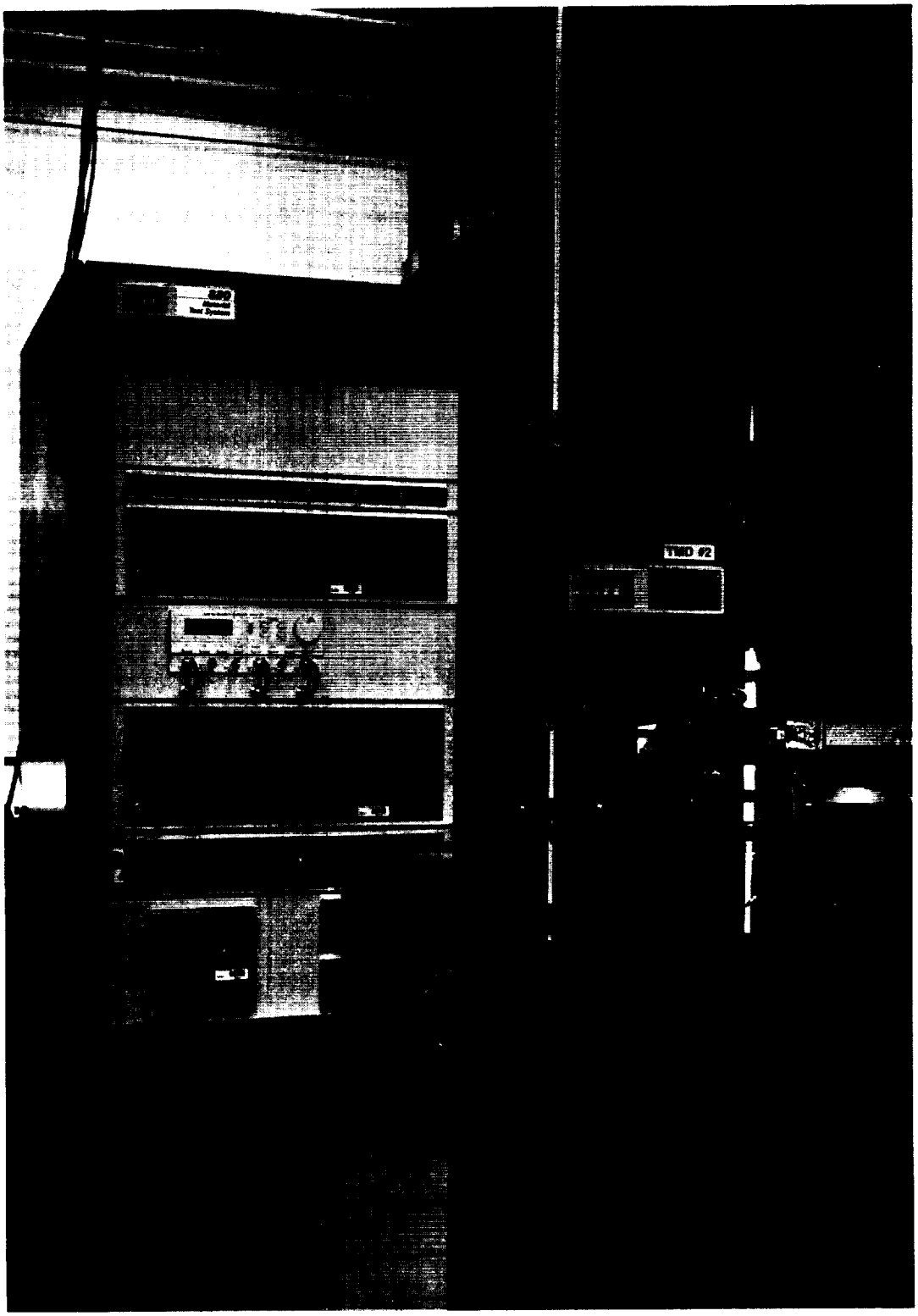

Figure 3.5 - Servo-Hydraulic Load Frame & Electronics

feature is that this load frame employs high pressure hydrostatic bearings to laterally stiffen the actuator piston. This high lateral stiffness aids in maintaining precise specimen alignment, which in turn minimizes off axis bending. Incorporated within the hydraulics are dual 37.9 lpm (10 gpm) servovalves. This combination allows articulate dynamic response to rapid command changes. The system is equipped with state–of–the–art digital electronics for local control, and connected to a 16–bit satellite minicomputer system for remote control. All tests are run under remote computer control via an analog/digital (A/D), digital/analog (D/A) interface device. Data acquisition is handled by the minicomputer on an internal hard disk system. The software used to control the test will be discussed in section 3.6.3. The remote computer control system enabled subtle adjustments (via the software) to controlling parameters which would not have been possible with a local function generator. Without these adjustments, precise strain/temperature phasing in the presence of a constant mechanical strain rate could not have been achieved. Thus, the computer control capability was essential in attaining the degree of control desired for these tests.

Figure 3.6 displays a close–up of the specimen and its immediate surroundings. The specimens are gripped with commercial water–cooled hydraulic grips incorporating collets designed for smooth shank cylindrical specimens. A smooth shank design (as opposed to a threaded shank design) was shown to be superior [43] in obtaining minimum specimen bending. Combining this feature, careful grip alignment and the hydrostatic bearing design, this test system is able to achieve precise axial alignment. Although the grips are water cooled for their own protection against the high temperatures, this water cooling

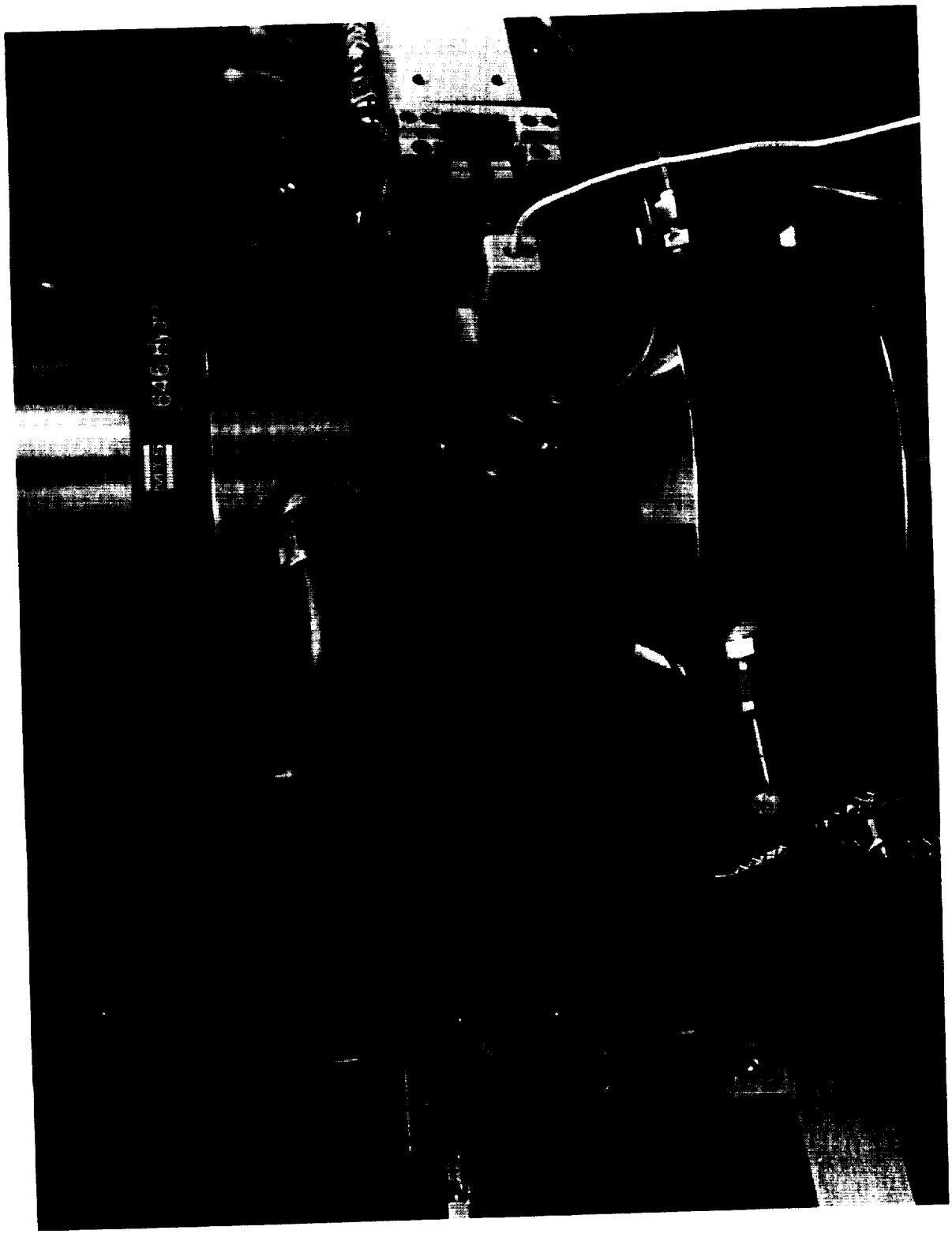

Figure 3.6 - Close-Up of Load Train

provided another important function during the thermomechanical cycle, namely, specimen cooling. The grips remove heat through the specimen's shanks to allow controlled temperature cycling. The cyclic temperature rate is predominantly dependent upon the cooling portion of the cycle; this became a limiting control factor during the "low" temperature tests. Forced air was not considered as a means of specimen cooling, as this method would have created intolerable thermal gradients within the gauge length section. Again, it is emphasized that the thermal gradients were found to promote specimen barrelling.

Also shown in Figure 3.6 is the commercially available extensometer used to measure axial strains. This axial extensometer employs a metallic flexure element in combination with a resistance based system to measure physical displacement. An axial gauge length of 12.7 mm (0.5 in.) is selected over a length of 25.4 mm (1.0 in.) simply because it is easier to control thermal gradients over the smaller length. For protection against the high temperatures, the extensometer is water–cooled, and further equipped with a water–cooled heat shield. Axial strains are sensed by conical point quartz probes extending from the extensometer. These probes require dimples imposed upon the specimen's surface for guidance and attachment. As the main interest of this study is thermomechanical deformation and not fatigue life, it is concluded that dimples will not influence material response.

Induction heating is used to heat the specimens. Hastelloy X is highly susceptible to this type of heating and this method is convenient for rapid heating and temperature cycling. Induction heating also allows relatively free access to the specimen's surface; this is necessary to accommodate the extensometer probes. Power is provided by a 5 kilowatt radio frequency (RF)

induction heater controlled in a closed loop system. This system includes a self–tuning temperature controller, operated either locally (manually), or remotely by the computer described above, and a controlling thermocouple as the temperature feedback sensor. Type K chromel–alumal thermocouple wires are spot–welded onto the specimen's surface to monitor the temperature at several predetermined points (thermocouple location is discussed in Section 3.7.2). The induction coil's position along the specimen dictates the thermal gradients present during testing. Highly localized "hot spots" can be created or eliminated by subtle coil adjustments. Hence, attaining a precise temperature profile, even over a 12.7 mm (0.5 in.) gauge section, can be an extremely tedious and time–consuming task. Traditionally, coils are constructed with a continuous single segment design in which spaces are created to accommodate the extensometer probes. This provides sufficient heating, but does not allow individual windings to be adjusted without affecting the entire coil. Therefore, coil movements directly interpreted as temperature changes along the specimen cannot be pursued in a systematic manner. In contrast, the induction heater work coils and support fixture used for this series of experiments, shown in Figure 3.7, is quite different. This system consists of three independently adjustable coil segments. Shown is a 3–2–3 winding configuration. This, as well as 4–1–4, and 5–2–5 configurations were employed throughout the experiments, depending upon specimen design and maximum cycle temperature. The coil segments are adjustable in the vertical, and radial sense, thereby allowing a straight–forward systematic approach to temperature modification at highly localized positions along the specimen. The coils are constructed from 3.175 mm (0.125 in.) outer diameter copper tubing and continuously water–cooled throughout the cycle.

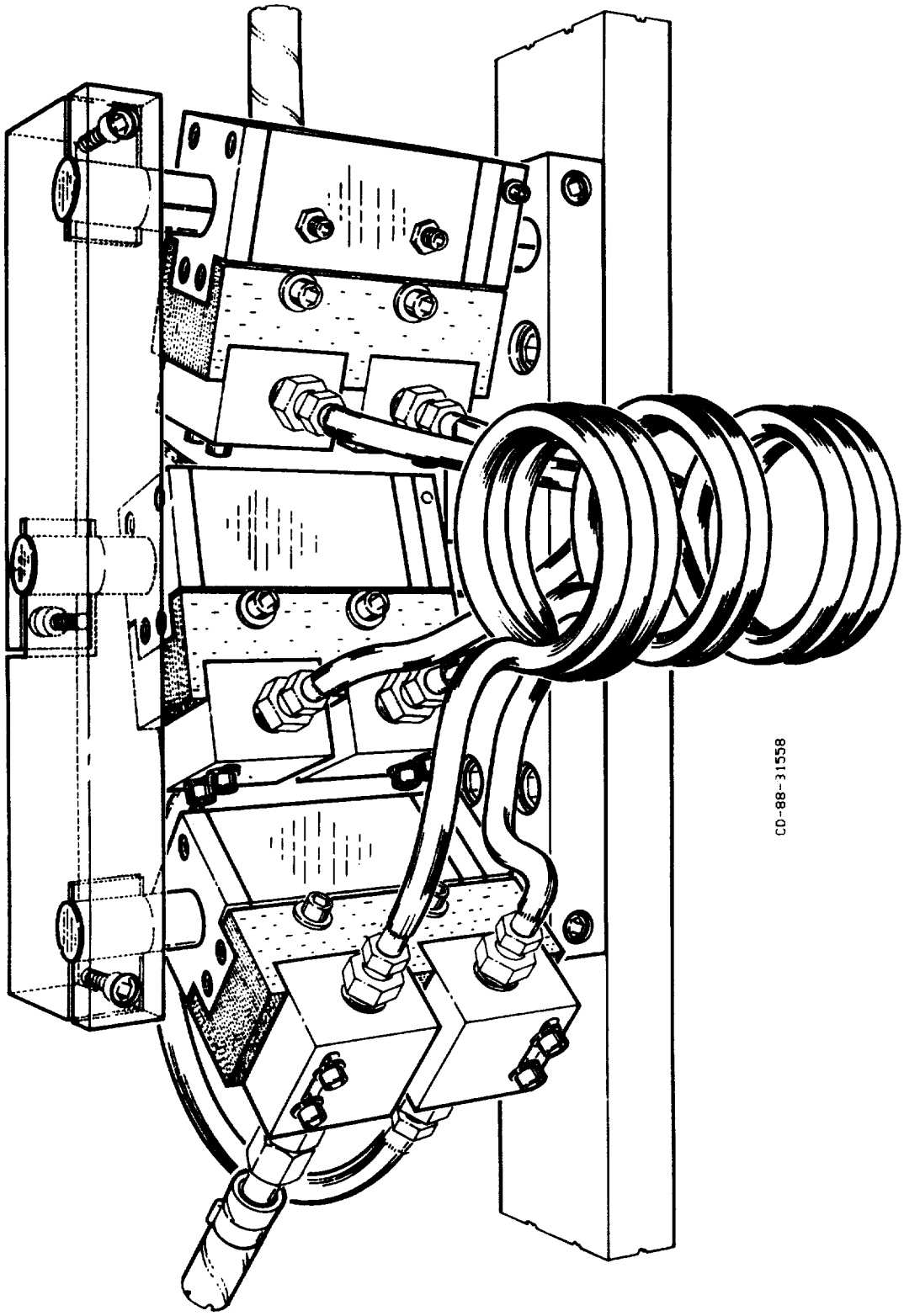

Figure 3.7 - Induction Coil Fixture

Electrically, the three coils are connected in series to the 5 kw induction heater. This advanced fixture enables proper temperature profiles to be obtained in a matter of hours, as opposed to days. A more comprehensive description of this fixture (developed at NASA Lewis Research Center) can be found in [44].

3.6.3 Software

The thermomechanical test control program is written in FORTRAN 77 and can be found in APPENDIX B. In general, the software had two basic functions, to control the loading functions (strain and temperature) and control data acquisition. Several changes were made throughout the study as improved experimental techniques were developed. The majority of these changes involved implementing improved methods of controlling and phasing (Section 3.7.2 and 3.7.3, respectively) mechanical strain and temperature. Control and phasing difficulties arise as a result of the time lag between temperature command and actual specimen temperature; this is most noticeable at command reversals. This problem is minimized through proper programming adjustments of the command waveforms, where the temperature lag can be anticipated. This subject is discussed further in Section 3.7. The software increments the controlling functions through real–time D/A calls. Calls were made at a rate of 100 per second.

Data acquisition is complicated by electrical noise present in the laboratory. The RF induction heaters are responsible for approximately ±5 mv peak–to–peak of high–frequency noise, and general laboratory low–frequency noise is approximately ±10 mv peak–to–peak. In the presence of this noise, direct data sampling results in "jagged" hysteresis loops, therefore, an interactive

routine was implemented to collect a point every A/D call (100 times per second), and then average a predetermined number of these points into one point before writing to the disk. This scheme averaged out the electrical noise present for any one given A/D sampling. As a general rule of thumb, 450 points/cycle (hysteresis loop) provided adequate resolution, therefore, the data sampling rate varied from 0.5 sec./point to 2.0 sec./point, depending upon the cycle time.

3.7 Experimental Procedures and Techniques

3.7.1 General Comments

Strain controlled axial–thermomechanical tests involving cyclic temperature conditions are not typically conducted in most experimental programs due to obvious difficulties. As a result, very little information is available in either the literature or existing test standards to use as a guide for procedures and techniques. Thus, in formulating the experimental procedures and techniques for this study, several options for each variable were thoroughly investigated and optimized as functions of specific equipment and material. Through the optimization of these individual considerations a well controlled systematic approach evolved.

3.7.2 Thermal Considerations

Several variables must be considered which relate solely to the thermal condition of the specimen. These variables include 1) locations for temperature monitoring and control, 2) thermal gradients (static and dynamic), 3) heating and cooling rates, and 4) thermal strain compensation under a fixed mechanical strain range. In order to conduct closely controlled thermomechanical

experiments, these inter–dependent variables must be optimized in a parallel manner. It is important to note that these variables will also be significantly influenced by specific test material and equipment.

During the process of adopting proper experimental procedures and techniques, considerable effort was placed on minimizing thermal gradients. This task, typically considered "good practice" when conducting well controlled high temperature tests, played a more significant role with this material. Gradients of seemingly insignificant quantities are instrumental in promoting specimen barrelling under high–temperature out–of–phase thermomechanical conditions. As barrelling progresses, and cross–sectional changes occur within the gauge section, engineering stress and strain calculations become unreliable. Thus, gradient control over the gauge section was essential.

The first step in controlling temperature gradients resides in one's ability to monitor temperature gradients. As previously stated, the tests utilized intrinsic thermocouples (spot–welded to the specimen's surface). Although fairly reliable, thermocouples are only capable of measuring temperatures at highly localized points along the specimen, specifically, the exact point of physical contact. This may prove to be a disadvantage, especially when induction heating is employed. Experience has shown that induction heater work coils can often create highly localized "hot" spots. It is important to place the thermocouples sufficiently close, so as to insure these "hot" spots are detected. After examining several possible configurations, a satisfactory arrangement was established and used throughout all the experiments; this thermocouple configuration is shown in Figure 3.8. An axial separation of 6.35 mm (0.25 in) provided adequate resolution for temperature monitoring. This eleven–thermocouple system

THERMOCOUPLE CONFIGURATION SHOWN ON SPECIMEN DESIGN #2 ALLOWS AXIAL AND CIRCUMFERENTIAL VERIFICATION OF THE SPECIMEN'S TEMPERATURE

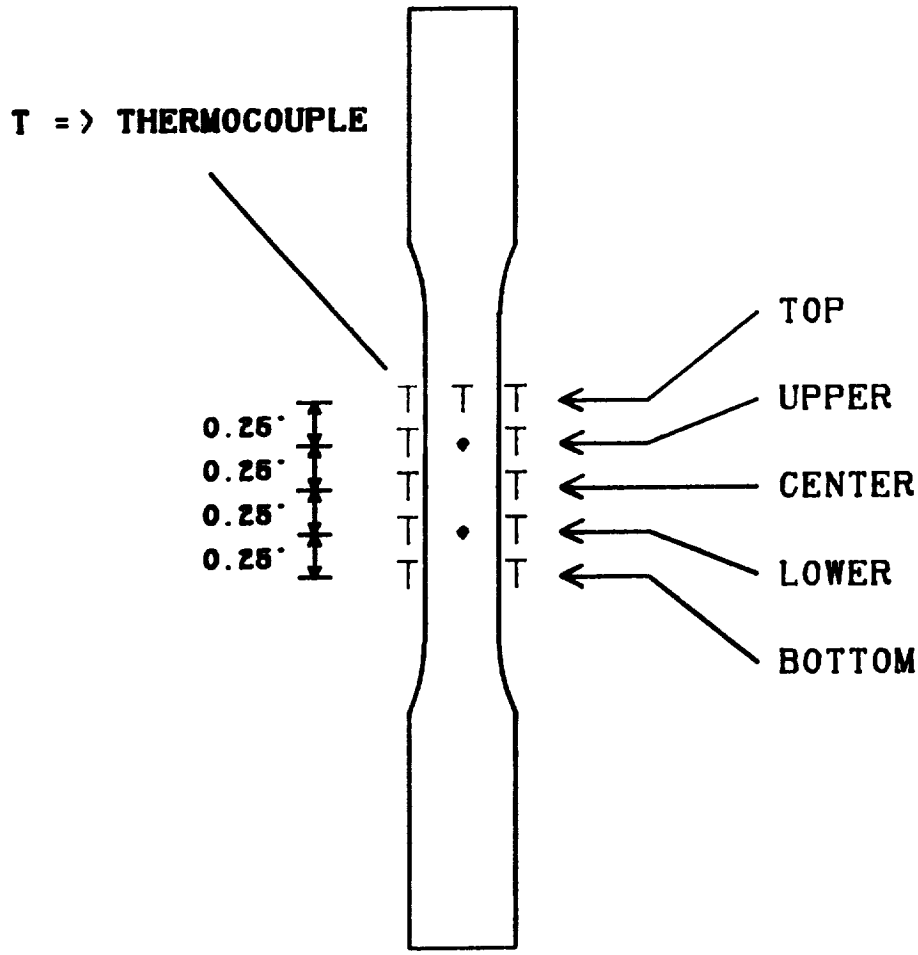

Figure 3.8 - Thermocouple Configuration

includes two sets of five on opposite sides of the specimen (180° circumferential separation), and one located on the back–side of the specimen (opposite the extensometer probes) to function as the feedback sensor for closed–loop temperature control. The redundant set of five allowed verification of the temperature in a circumferential sense as well as a check on the gradients present in the axial direction. For tests involving temperatures above 800°C (1472°F), a fine ceramic sleeve was placed over the portion of thermocouple wire within the induction heater work coils. Without this sleeve, the protective coating eventually becomes brittle and spalls from the thermocouple wire; this results in erroneous temperature readings.

The next step in gradient control is obtaining a "proper" static temperature profile. This objective must be divided into two major tasks. First, the "proper" static profile must be defined and second, induction work coil adjustments are made to obtain this desired static profile. At the onset of this investigation, it was assumed that minimized cyclic temperature gradients would result from initiating the test with a flat static profile at an intermediate temperature. For example, a test involving cyclic temperature conditions from 600°C (1112°F) to 800°C (1472°F) would begin with the full length of the gauge section as close to 700°C (1292°F) as possible. As there are no governing specifications for thermomechanical testing, this was viewed as a logical starting condition. By monitoring the temperature at the locations described above, it was revealed that the dynamic temperature profile did not remain flat. Depending upon temperature rate, and to a lesser degree magnitude, gradients as large as 15°C (27°F) were developed within the 12.70 mm (0.50 in) gauge section. More specifically [using a case where conditions promoted dynamic

gradients of 15°C (27°F)], the gauge length extremes (positions marked "upper" and "lower" on Figure 3.8) experienced temperatures 15°C (27°F) hotter at the maximum cycle temperature, and 15°C (27°F) cooler at the minimum cycle temperature, than that found at the mid–section of the gauge length (position marked "center" on Figure 3.8). In order to understand the factors creating these dynamic gradients, it is important to recall the means by which thermal cycling is accomplished. Specimen heating is induced by two major and one minor coil winding (i.e. 3–2–3, 4–1–4, 5–2–5); see Figure 3.7. The induction fields produced by the major coils are inherently stronger than that produced by the minor coil, thus, the specimen portions encircled by the major windings (just above and below the gauge section) will tend to heat faster. This condition could possibly be avoided by employing a separate closed–loop temperature controller for each of the zones (upper, middle and lower gauge area), but the control complications introduced by such a system (i.e. controller synchronization and strain–temperature phasing) may out–weigh the advantages. Specimen cooling is provided by the water cooled grips. As the specimen's ends are continuously cooled throughout the cycle, it is inevitable that a cool–hot–cool (top–center–bottom) thermal gradient will exist over the full length of the specimen. This type of cooling also promotes a variable cooling rate along the length of the specimen, namely, the ends cool faster that the mid–section. Thus, both a slightly accelerated heating and cooling rate exists at the gauge length extremes (as compared with the mid–gauge section). In addition to these symmetric anomalies, testing in air allows thermal convection currents to play a role in dynamic thermal gradients. A point located within the lower length of the specimen (position marked "lower" and below) typically requires more energy

than its counterpart within the upper length when a uniform temperature is desired. This effect can be countered under static (isothermal) conditions by proper coil segment and winding adjustments. However, dynamic (thermomechanical) conditions lead to accelerated heating rates within the upper length during the heating portion of the cycle, and accelerated cooling rates within the lower length during the cooling portion of the cycle. Adjustments can be made to minimize effects during the heating portion of the cycle, as here the induction heater work coils provide the means by which temperature conditions are changing. In contrast, during the cooling portion of the cycle where the coils are less active, and temperature change is dominated by the cool grips, coil adjustments are ineffective at controlling convection effects. Hence, gradients produced in this manner are most prevalent during the cooling portion of the cycle, as the minimum cycle temperature is approached.

Given these inherent complexities, it is impossible to cycle temperature without inducing gradients in the gauge length. At best, it is possible to eliminate gradients at a specific point in the cycle. The next step was to decide the location of this point. Three obvious points were considered: 1)average–cycle temperature, 2) maximum cycle temperature and 3) minimum cycle temperature; see Figure 3.9. In studying all three conditions, it was concluded that no one condition minimized gradients throughout the entire cycle. However, one finding established from the investigation on barrelling revealed that the rate and severity of this phenomenon increases as temperature increases under out–of–phase conditions. Combining this with the fact that thermal gradients are strong barrelling catalysts, a dynamic thermal profile exhibiting absolute minimum gradients at the maximum cycle temperature is the best possible

THREE POSSIBLE SCENARIOS FOR DYNAMIC TEMPERATURE PROFILE ALIGNMENT

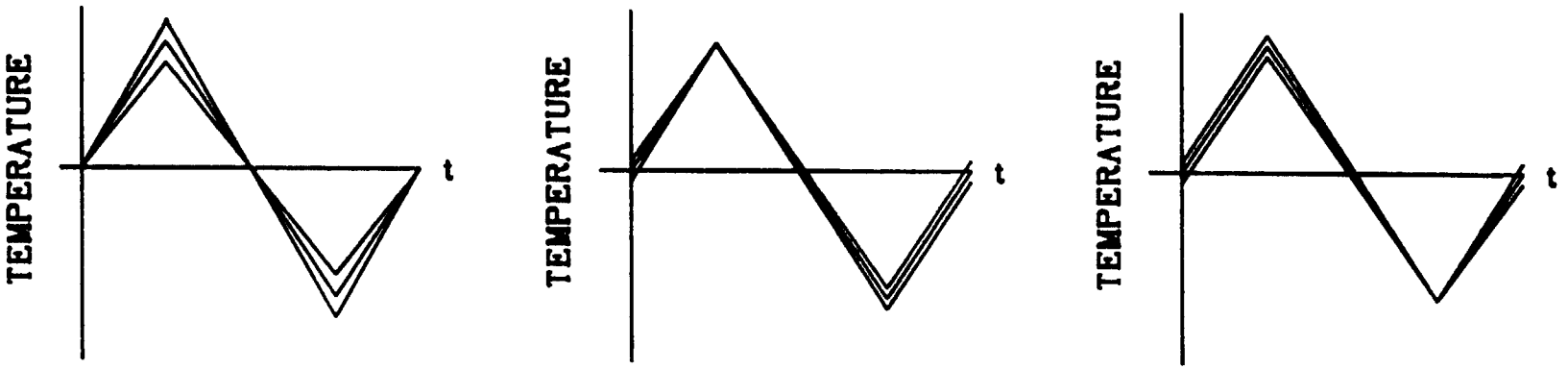

Align Temperatures such that gradients are minimized at average cycle temperature

Align Temperatures such that gradients are minimized at maximum cycle temperature

Align Temperatures such that gradients are minimized at minimum cycle temperature

THE CURVES REPRESENT TEMPERATURES AT THREE DIFFERENT AXIAL LOCATIONS WITHIN THE SPECIMEN'S GAUGE SECTION

Figure 3.9 - Temperature Profile Scenarios

condition. With this specific dynamic condition required, a corresponding mid–temperature static condition is postulated on the basis of anticipated temperature rates at various locations along the length of the specimen. The imposed gradient required for the proper static profile varied only slightly as a function of temperature magnitude. A typical static profile is shown in Figure 3.10.

Having defined a proper static profile, this condition is attained through induction work coil adjustments. Details of this procedure will not be included. The advanced induction heater work coil fixture employed here (discussed in Section 3.6.2) enabled this task to be accomplished with an accuracy of $\pm 1^{\circ}C$ ($\pm 2^{\circ}F$) within the gauge section. The specimen is then thermally cycled under zero load in order to monitor dynamic thermal gradients. This two–step procedure [1) adjust static profile, 2) cycle temperature] is repeated as necessary until the hot–end dynamic gradients are less than $\approx 2^{\circ}C$ ($\approx 4^{\circ}F$) within the gauge section. By minimizing the hot–end thermal gradients, high temperature out–of–phase tests were performed with minimal barrelling.

In the spirit of controlling dynamic thermal gradients, a concern arose involving temperature rate linearity. As locations were monitored for dynamic thermal gradients, it was discovered that in addition to their various heating and cooling rates, temperature rate linearity was not maintained. This deviation amplified dynamic gradients and created difficulties in subsequent data analysis. The closed loop temperature control system employs a thermocouple as the feedback sensor, hereafter referred to as the controlling thermocouple. Based on the difference between command and controlling thermocouple feedback, induction heater power is adjusted. By this means, specimen temperature is

A TYPICAL STATIC TEMPERATURE PROFILE NECESSARY TO OBTAIN MINIMIZED DYNAMIC TEMPERATURE GRADIENTS AT THE MAXIMUM CYCLE TEMPERATURE

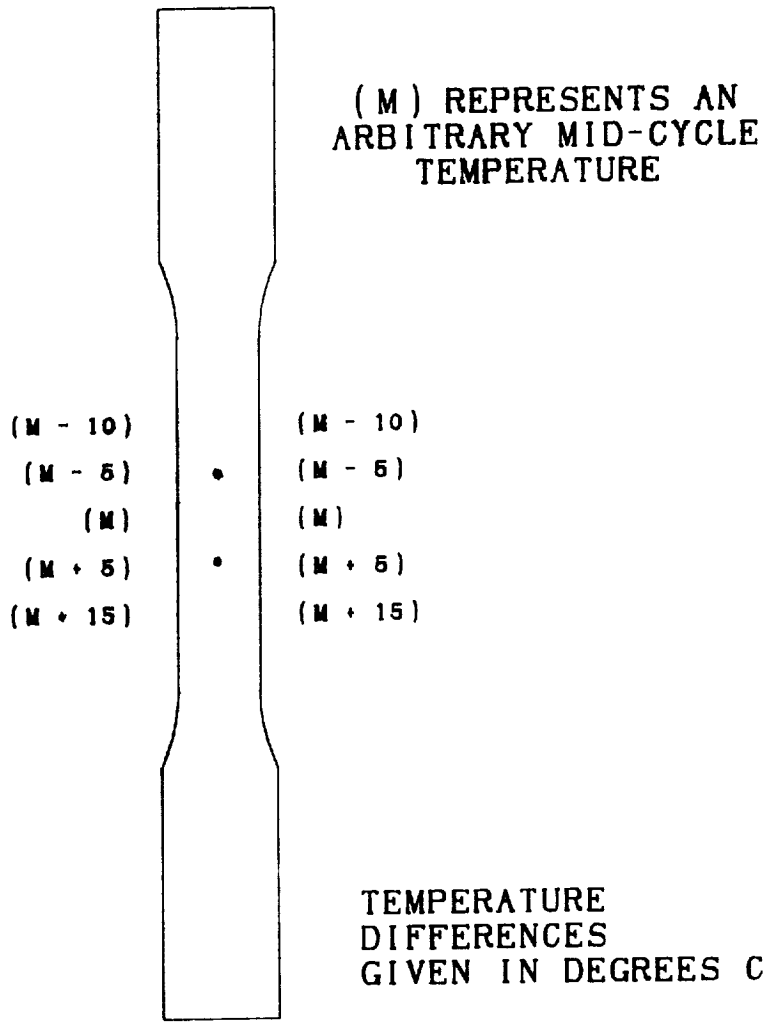

Figure 3.10 - A Typical Static Profile

controlled. Although greatly simplified, this description reveals the source of the observed deviation. Temperature (and resulting temperature rate) is controlled at the highly localized position of the controlling thermocouple, all other points along the specimen are strictly dependent. The point of control (location of the controlling thermocouple) is forced to follow the linear temperature command [i.e. $\frac{dT}{dt} = C$ or $\frac{d^2T}{dt^2} = 0$ throughout the cycle (in theory)], but the change in temperature rate at all other locations is influenced by many of the same factors leading to increased heating and cooling rates. Hence, the location of the controlling thermocouple influences the linearity of the temperature waveform at various locations. Traditionally, the controlling thermocouple is placed within the gauge length over which the strains and temperatures are measured, namely, at the center of the gauge length section (position marked "center" on Figure 3.8). Shown in Figure 3.11 is a thermal cycle from 600°C (1112°F) to 800°C (1472°F) where the "center" thermocouple is controlling. Here significant waveform distortions are revealed at both the "top" and "bottom" thermocouple locations, primarily after temperature reversals. This effect is explained by recalling that locations outside the gauge section have both a higher heating and cooling rate. Using the "cold" end of the cycle for illustration, the "center" temperature response is slow (relative to positions above and below), therefore, the time period required for temperature reversal response is relatively high compared to the "top" and "bottom" positions. The controller compensates for this lack of response (at the controlling thermocouple location) by increasing the induction heater power. The power required to maintain the command temperature rate at the center location has an over–powering affect at the other locations, thereby leading to a temporarily accelerated rate of change. Shortly

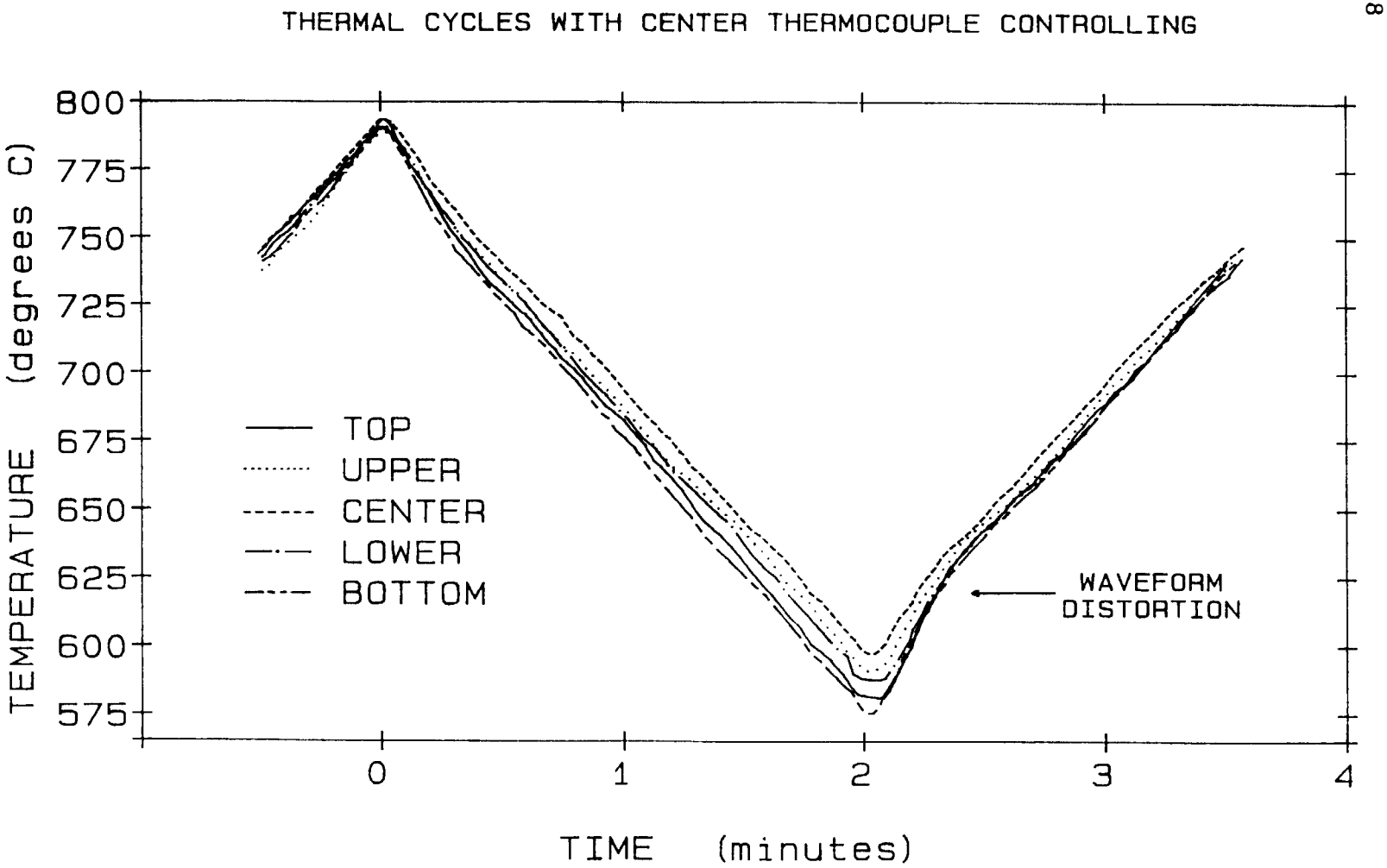

Figure 3.11 - Center Thermocouple Controlling

after this transition period, when the error between command and actual controlling thermocouple temperature is reduced, change in power commands return to steady increments and all locations along the specimen return to their respective linear rates (see Figure 3.11). Hence, the deviation in linear heating and cooling rates (amplifying dynamic thermal gradients) was promoted by the controlling thermocouple's "slow" response position. A possible solution was to place the controlling thermocouple at a "quick" response position. Shown in Figure 3.12 is a comparable thermal cycle with the controlling thermocouple at the "top" position. Obvious improvements are visible when controlling from this position. The control thermocouple is now more responsive (relatively) to power changes, thereby eliminating conditions of under/over–powering at other locations during temperature reversals. The variation in response with respect to position is now seen as a slight lingering of the "center" position during reversals, as linearity is not now forced at this position. Although effects leading to a form of non–linearity are still present, this control position does not promote under/over–powering upon temperature reversals, thus minimized dynamic thermal gradients are maintained.

Throughout the process of optimizing procedures and techniques, temperature rate had the most globally dominant effect; specifically, as temperature rate increased all other aspects became more difficult to control. Rates from 25°C/minute (45°F/minute) to 200°C/minute (360°F/minute) were investigated while monitoring dynamic gradients, temperature rate linearity and thermal strain compensation. A rate of 25°C/minute (45°F/minute) allowed the highest degree of control for all three, but created a cycle time of 16 minutes and a mechanical strain rate of $1.25 \times 10^{-5} s^{-1}$. An acceptable compromise was

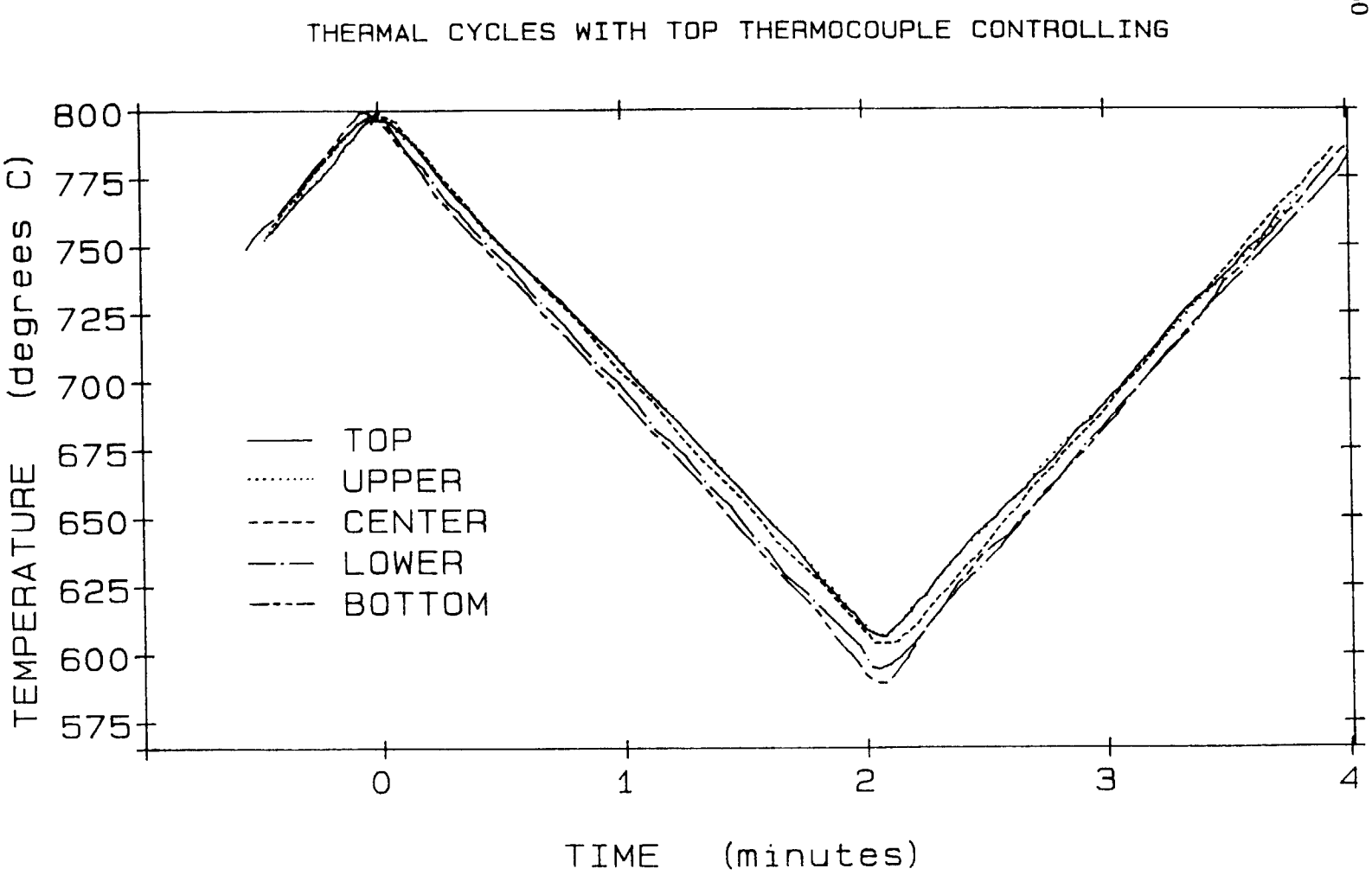

Figure 3.12 - Top Thermocouple Controlling

established at 50°C/minute (90°F/minute), where a high degree of control was still maintained with a more reasonable cycle time of 8 minutes, and a mechanical strain rate of $2.5x10^{-5}s^{-1}$. Therefore, most tests were performed at this temperature rate. Four tests originally conducted with a temperature rate of 100°C/minute (180°F/minute) [4 minute cycles with a mechanical strain rate of $5.0x10^{-5}s^{-1}$] are reported herein. These tests were not repeated with the slower temperature rate, as the results are believed to be satisfactory.

The thermal considerations discussed above have been centered around minimizing temperature gradients. As this difficulty is entirely a function test conditions, theoretically, under idealized conditions, this problem could be eliminated. In contrast, the final thermal consideration discussed pertains to difficulties arising from a characteristic material response, namely, thermal strain. Thermal strain plays a significant role in the experimental procedures and techniques as a result of two imposed control conditions. First, in an effort to study the thermomechanical dynamic strain aging characteristics of Hastelloy X, the tests are performed under strain control. The difficulty here arises due to the fact that thermal strain has a first order affect on the total strain in the axis of control (longitudinal); thus dynamic temperature conditions complicate total strain control parameters such as rate, range and response. Effects of this type are most evident when phasing problems exist between thermal strain (temperature) and mechanical strain (see Section 3.7.3). Second, in order to make a "direct" comparison between thermomechanical and isothermal behavior, the thermomechanical tests are conducted with the same "stress inducing strain range" as the isothermal tests. In an isothermal strain controlled test, the strain component producing stress in the specimen is the total strain component, as it is

the only dynamic strain component present once the the specimen is brought up to test temperature under zero load (dT = 0 during the test). In a thermomechanical strain controlled test, the strain component producing stress is that in addition to (or opposed to) the thermal strain component, hereafter referred to as the mechanical strain component (ϵ_m);

$$e_t - \epsilon_{th} = \text{"stress inducing strain"} = \epsilon_m$$

where e_t and ϵ_{th} are the total and thermal strain, respectively. Thus, in order to make comparisons of stress response, it was desired that the mechanical strain in the thermomechanical tests equal the total strain in the isothermal tests. To perform a test with a fixed mechanical strain range, proper compensation must be made for thermal strains. Three techniques were examined and evaluated, these are 1) equal partitioning of expected total thermal strain range, 2) associating a previously recorded thermal strain based on time as the mapping function and 3) employing a function f(T) to calculate in–situ thermal strains "on the fly". All three methods were possible through the software driven remote computer control used in these tests.

The first method (equal partitioning) relies upon the assumption that the induced thermal strains are linear with respect to temperature and time. The thermal strain range is acquired by thermal cycling under zero load. As maximum/minimum temperatures may vary [$\approx \pm 1^{\circ}C$ ($\approx \pm 2^{\circ}F$)] from one cycle to the next, maximum/minimum thermal strains will correspondingly vary, therefore, an average strain range is obtained after several cycles. The range is subdivided into equal increments corresponding to real–time command adjustments (100 times per second) issued during the test. These increments are simply added to (in–phase) or subtracted from (out–of–phase) the desired

mechanical strain increments, thereby obtaining the total strain increments. If the temperature range is relatively small [i.e. 200 °C (360°F)], the assumption of a linear relationship between thermal strain and temperature is well founded for this material. However, the assumption of linearity between thermal strain and time is not valid during temperature reversals. This is a result of the inability to maintain a linear temperature rate during reversals (discussed above). Consequently, a constant increment of thermal strain is added or subtracted, when actual temperature changes dictate a different amount. This condition ultimately results in slight over–straining or under–straining of the specimen. If phasing problems between temperature and strain do not exist, this over/under–straining effect is extremely difficult to detect from the hysteresis loops.

The second method investigated employs time as a mapping function to thermal strain, and relies upon the assumption of a constant relationship between time and thermal strain (temperature). As before, thermal strain is monitored as temperature is cycled under zero load. Strains are recorded along with their corresponding cycle time value. For example, with an eight minute cycle (480 seconds) and a sampling rate of 0.01 seconds, 48000 sets of time–thermal strain data points are recorded $[(t_1,\epsilon_{th_1}).....(t_{48000},\epsilon_{th_{48000}})]$. This time–thermal strain array is then used throughout the entire test to ascertain thermal strains on the basis of a given time increment in the cycle. One advantage over the previously described method is observed during temperature reversals. The time–thermal strain array reflects the nonlinear thermal strain rate which occurs at this critical point, thus the previously experienced over/under straining effects are minimized. However, although cyclic temperature commands remain constant

with respect to time, this is not necessarily the case between actual specimen temperature (actual thermal strain) and time. This gives rise to the main disadvantage of this technique. Small specimen temperature deviations of approximately 1–2°C (2–3°F) can be experienced from cycle to cycle. Correspondingly, small thermal strain variations are experienced. These small variations can not be properly handled do to the rigidly fixed nature of the time–thermal strain array.

Disadvantages of both methods described above directly result from their inability to compensate for varying in–situ temperature conditions. This promoted the investigation of a third method where thermal strains are calculated "on the fly" as a function of temperature. This method relies mainly upon the assumption that the function f(T) is capable of representing the thermal strains. The function is based upon a coefficient of thermal expansion which relates the strains measured over the 25.4 mm (0.5 in) gauge section to a single temperature measurement. The first step is to decide on a proper location for this temperature feedback. After evaluating several locations along the length of the specimen, as well as cases where temperatures were averaged over several locations, it was noted that all locations ("top" through "bottom" on Figure 3.8) performed adequately when coupled with an appropriate coefficient of thermal expansion, until a temperature reversal was encountered. Due to each location's unique temperature response during reversal (discussed earlier), one location's temperature was better able to maintain a linear relationship, namely the "top" position. This location's comparatively quick response nature made it most suitable for use in a linear thermal strain equation;

$$\epsilon_{th} = \alpha T + \mathbb{C}$$

Here, α represents the coefficient of thermal expansion (CTE), and $\mathbb{C}$ is an appropriate constant. Having decided upon the "top" location for temperature feedback, the specimen is thermally cycled under zero load to obtain a CTE associating this particular temperature feedback to the strains experienced over the gauge section. To insure the CTE is correct, the specimen is again thermally cycled, but this time in strain control, where the thermal strain equation is commanding the "compensating" strains. Shown in Figure 3.13 is a typical thermal strain cycle under these conditions. Theoretically, zero stress conditions should be maintained throughout the cycle. As can be seen from Figure 3.13, minimal stress (deviations along the Y axis) is developed. Conditions were felt to be well controlled if the induced stress is contained within ±1% of the maximum stress experienced during the test; this was typically the case. After proper verification of the CTE, the thermal strain equation is used to independently calculate thermal strains throughout the test. The total strain command is then generated by summing two independent functions (thermal strain and mechanical strain). Both subtle changes in temperature range, and a non–linear thermal strain rate are properly handled by this less rigid technique. Of the three thermal strain compensation techniques described, the thermal strain equation (described last) is best capable of maintaining accuracy under potentially varying conditions, thus, it was employed throughout this investigation.

3.7.3 Phasing Considerations

In addition to the thermal considerations discussed above, axial–strain controlled thermomechanical tests are also strongly influenced by the techniques used to phase temperature and strain. As a consequence of first order coupling

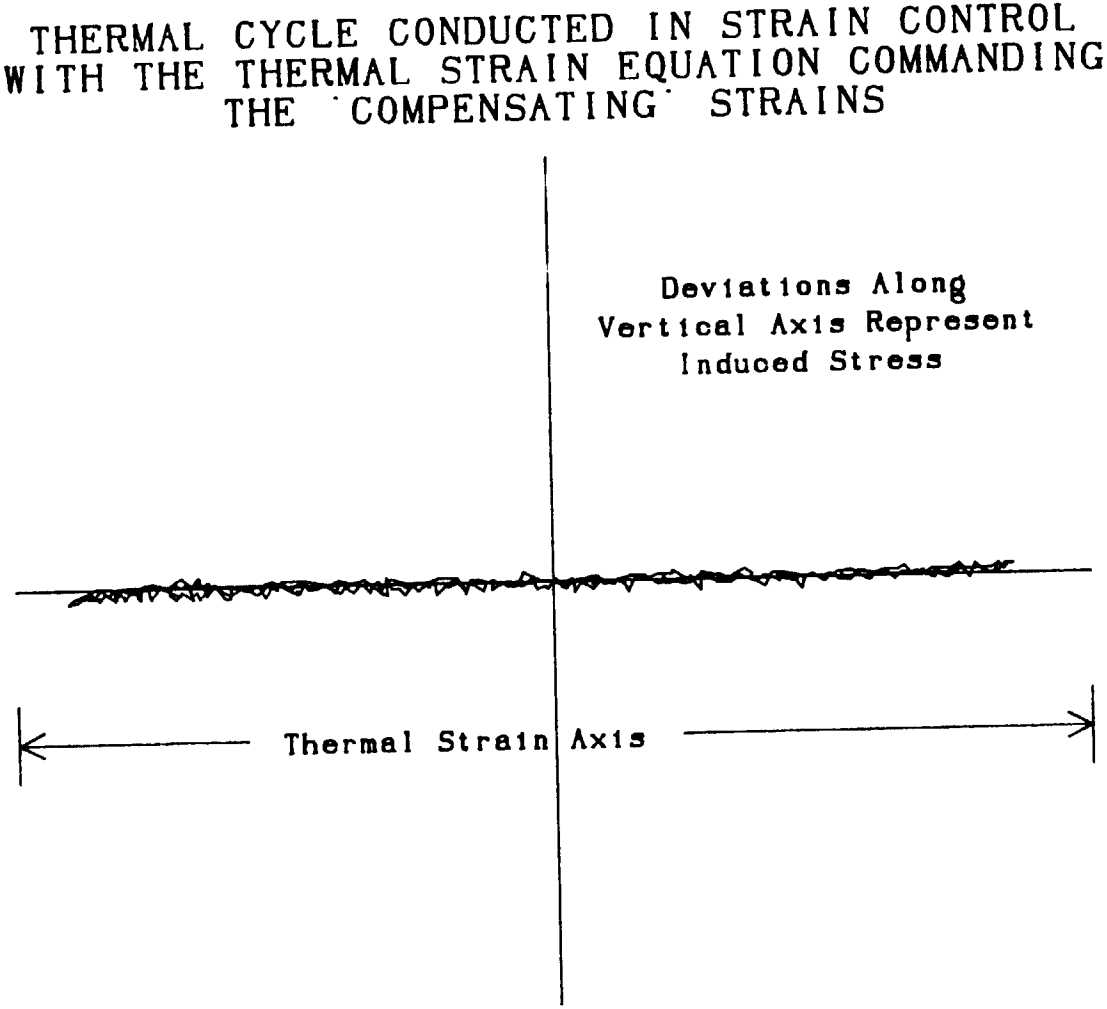

Figure 3.13 - Thermal Strain Compensation

effects between temperature and axial strain (thermal strain), improper phasing will result in distorted hysteresis loops and a fluctuating strain rate. Also, as these tests are strain controlled, phasing problems promote extensive control difficulties.

Phasing problems arise as a result of command–response lag time differences between strain and temperature. Command–response lag time is defined here to be the real time elapsed between issuing a command and obtaining the desired specimen condition. In general, the command–response lag time is dictated by specific equipment characteristics. The load frame system utilized in this study (Section 3.6) is capable of articulate real time response upon command reversals. Thus, the mechanical component (mechanical strain) is assumed to be near immediate, and exhibit a negligible command–response lag time. Alternatively, the command–response lag time for temperature is comparatively large. This lag period is further amplified when immediate command reversals are issued, such as those encountered with a triangular or "sawtooth" command waveform. Consequently, it is at the reversal points where phasing difficulties are most prominent. The temperature command–response lag time can be minimized with the appropriate equipment and specimen geometry (discussed earlier), but in comparison, may still have a duration several orders of magnitude larger than that of the mechanical components'; thus, inappropriate phasing conditions will exist. In this investigation, emphasis was placed on developing methods for ensuring appropriate phasing (0° for in–phase conditions and 180° for out–of–phase conditions) between temperature and strain based on actual specimen response.

Three phasing techniques were evaluated under the following criteria. First, phasing accuracy was defined as the capability of ensuring that the specimen's maximum and minimum mechanical strain occurs simultaneously with the specimen's maximum and minimum temperature (in–phase) or minimum and maximum temperature (out–of–phase), respectively. Second, as these tests are strain controlled, and analyzed most often on the basis of stress–mechanical strain response, it is important that the phasing method maintains a constant mechanical strain rate.

The first technique investigated is defined here as the time–based method. The control variables are phased on the basis of command waveform where the common mapping function is real–time. The variables are commanded simultaneously with respect to cycle time, but independently of each other. Thus the command waveforms are perfectly phased. This method is commonly employed as it does not require the use of a computer. Two properly connected function generators can issue the commands simultaneously. Although exact command phasing is ensured, the specimen response phasing is usually quite poor. This is a direct result of the comparatively slow command–response time of temperature, particularly during command reversals. More specifically, a temperature rate of 50°C/minute (90°F/minute) resulted in a phase shift greater than 10 seconds during command reversals. The exact magnitude of the shift was dependent upon the general temperature regime; low temperatures [200° C to 400°C (392°F to 752°F)] promoted increased command response lag periods, and therefore increased phase shifts. Although the independent time–based method was not used here for obvious reasons, it can be used with moderate success with forced air cooling and/or a less "demanding" control waveform (i.e. sine wave).

The second technique investigated involves slaving the mechanical strain command to the temperature response. This method utilizes the fact that the command–temperature response time is much longer than that of the mechanical strains'. Therefore, the mechanical strain increment is commanded after its corresponding temperature condition is achieved. Performing this sequence requires a computer to continually read the specimen's temperature through an Analog to Digital (A/D) conversion. The digital temperature reading is then used to calculate and command a corresponding mechanical strain. This method maintains precise response phasing throughout the entire cycle. However, the disadvantage of this technique can be seen when viewing the mechanical strain rate. As a result of forcing the mechanical strain rate to emulate (in proper proportion) the temperature rate, both signals experience a significant rate fluctuation during command reversals. The mechanical strain rate now reveals the first lethargic rate, and then accelerated rate, typically associated with the temperature response during reversal. This inconsistent mechanical strain complicates subsequent analysis, and in extreme cases, is evidenced by distorted stress–mechanical strain hysteresis loops.

The final method developed to control phasing employs the best features of the two previously described techniques. Intermittent dependent and independent temperature commands are issued with the emphasis placed on maintaining a constant mechanical strain rate. The mechanical strain is calculated by an independent function, ensuring a constant rate throughout the cycle. During portions of the cycle which are not in the vicinity of command reversals, a master/slave, mechanical strain/temperature relationship is used to calculate the temperature command. At a pre–specified point just prior to a

command reversal (i.e. 5 to 10 seconds prior), the temperature command is de–coupled from the mechanical strain and forced to reverse prematurely. The degree of prematurity is related to the temperature command–response lag time in such a way that the temperature response reversal occurs simultaneously with the mechanical strain reversal. As a result of the premature reversal, the temperature command waveform is pushed "ahead" of the mechanical strain waveform. This offset prevents the two commands from being re–coupled into their previous master/slave relationship. Therefore, a slightly decreased temperature increment ($\approx$ 90% of the slave command increment) is used after the response reversal, until the strain command waveform regains synchronization with the temperature command waveform. Synchronization of the two command waveforms occurs approximately 2 minutes after response reversal; at this point, the mechanical strain and temperature command calculations are re–coupled into their master/slave relationship. By making use of dependent and independent mechanical strain/temperature commands , and subtle variations in temperature rate, precise response phasing can be maintained in the presence of a constant mechanical strain rate. As this phasing technique allowed the greatest amount of accuracy, it was employed throughout all the tests.

3.7.4 A Systematic Experimental Approach

After having developed and verified a mature set of testing procedures and techniques, these complex tests can be conducted in a straight–forward systematic manner. The following sequential steps were used as a guide in setting up and performing the experiments for this study.

1) The specimen is cleaned and measured to obtain an accurate cross–sectional area in the gauge section.

2) Two dimples (indentations) are imposed upon the specimen's surface. These dimples define the gauge section and serve as guides for the extensometer probes.

3) Thermocouples are spot welded to the specimen's surface at predetermined locations.

4) The specimen is gripped in the load train and slowly brought up to test temperature under zero load, in load control.

5) If necessary, coarse induction coil adjustments are made to obtain a "reasonable" static temperature profile at the average test temperature.

6) The specimen is thermally cycled under zero load over the appropriate temperature range. Fine adjustments (as required) are made to the induction coils until the desired dynamic temperature profile is obtained.

7) The coefficient of thermal expansion (CTE or α) is calculated with respect to the temperature feedback of the controlling thermocouple. If the CTE is relatively constant over the test temperature range, a linear function is formulated to calculate the thermal strains (i.e. $\epsilon_{th} = \alpha\ T + \mathbb{C}$). If large temperature ranges are traversed, it is usually the case that the CTE is not constant. In such cases, a piecewise–linear function was found to perform well as the thermal strain compensation equation. Higher–order polynomials did not "behave" well enough to maintain the high degree of control necessary.

8) The thermal strain compensation equation is verified by subjecting the specimen to thermal cycles under strain control; here the strain command is calculated by the thermal strain "compensation" equation. If the equation is accurately predicting the specimen's thermal expansion, the specimen will not experience any loading. Adjustments are made (if necessary) to the thermal strain compensation equation until a "zero" load state is maintained throughout the cycle.

9) The specimen is subjected to small loads at various pre–selected isothermal temperatures in order to obtain the elastic modulus as a function of temperature.

10) Full thermomechanical testing is initiated. If the test involves fully reversed mechanical loading, the experiment is most easily initiated from the average cycle temperature. All data collection (load, strain & temperature) is handled by the computer. As a backup, a strip chart (load vs. time & strain vs. time) and periodic X–Y recordings (hysteresis loops: load vs. strain) are maintained throughout the test.

11) The definition of test completion may vary with respect to the material behavior for each test. Tests involving temperatures greater than ≈ 600°C (≈ 1100 °F) typically developed fatigue cracks at the extensometer dimple locations prior to 1500 cycles. Upon visual detection of such cracks, the tests were considered complete. Tests involving temperatures less than ≈ 600°C (≈ 1100°F) were capable of withstanding several thousand cycles (involving several weeks) before initial fatigue cracking was detected. As a result of time

constraints, this condition could not be satisfied. Therefore, test completion was declared when no significant change in material behavior (i.e. stress range, inelastic strain,...etc.) occurred over several hundred cycles.

12) Upon test completion, the specimen is carefully inspected and measured to quantify any changes in geometry. Note: If conditions are suspect of promoting cyclic instabilities (i.e. specimen barrelling), the specimen's geometry should be carefully monitored throughout the test. This may require periodic test interruptions for measurements.

13) Metallographic examination should be performed to asses any microstructural changes.

CHAPTER 4

EXPERIMENTAL RESULTS : PHENOMENOLOGICAL AND METALLURGICAL

4.1 Introduction

Experimentally determined material properties used for thermomechanical test control and data reduction are discussed and compared with those obtained from previous isothermal experiments. The complex isothermal hardening trends observed by Ellis et al [36] reveal the significant dynamic strain aging experienced by Hastelloy X. These hardening trends are directly related to well documented (see Chapter 2) microstructural changes. General microstructural characteristics revealed under isothermal conditions are discussed and associated with three designated temperature regimes ("low", "middle", and "high"). Thermomechanical data is introduced phenomenologically and metallurgically with comparisons to isothermal data. Unique thermomechanical trends are discussed and identified with physical instabilities experienced in the microstructure. Emphasis is placed on relating thermomechanical path dependence observed in the phenomenological data to the microstructural physics. Note: All isothermal data shown was generated by Ellis et al [36] at the NASA Lewis Fatigue and Structures Laboratory.

4.2 Pertinent Material Properties

In order to perform the axial–strain controlled thermomechanical tests, the longitudinal thermal strains must be accounted for and properly compensated. This is done during the test by a pre–determined thermal strain compensation equation (see Section 3.7.2 and Section 3.7.4) This equation is uniquely established for each specimen by stepping the temperature through $10^{\circ}C$ ($18^{\circ}F$) increments over the range for that specific test. (Each test's equation was only valid over the test temperature range, as this was sufficient to accurately perform the test.) The resulting strains (thermal strains) were used to calculate a corresponding coefficient of thermal expansion (CTE). Listed in Table 4.1 are the mean coefficient of thermal expansion values calculated for the various thermomechanical experiments, accompanied by established handbook values. This data is also shown graphically in Figure 4.1.

Data reduction schemes employ the experimental CTE to extract the thermal strains (ϵ_{th}) from the total strain (e). The resulting mechanical strain component (ϵ_m) can be "directly" compared with strain values from appropriate isothermal tests. In the same context, data reduction schemes can employ elastic moduli (E) to calculate the elastic strain component. This allows the mechanical strain component to be subdivided into an elastic (ϵ_{el}) and inelastic (ϵ_{in}) part.

$$e = \epsilon_m + \epsilon_{th} \qquad \text{where } \epsilon_m = \epsilon_{el} + \epsilon_{in}$$

$$\text{and further } \epsilon_{el} = \frac{\sigma}{E}$$

Hence

$$e = \frac{\sigma}{E} + \epsilon_{th} + \epsilon_{in}$$

The elastic modulus is assumed to be a function of only temperature, and therefore remain constant throughout an isothermal test ($\frac{dT}{dt} = 0 \Rightarrow E(T) = \mathbb{C}$). This is obviously not the case in a thermomechanical test where temperature is

MEAN COEFFICIENT OF THERMAL EXPANSION FOR HASTELLOY X

TEMPERATURE (Degrees C)	HANDBOOK VALUES	THERMOMECHANICAL HEAT
93	13.9	
204	14.1	
300		14.6
316	14.2	
427	14.7	
500		15.1
537	15.1	
648	15.4	
700		16.3
760	15.9	
871	16.2	
900		16.7
982	16.6	

Mean values established from room temperature

Values shown at 1 X 10^{-6} C^{-1}

Table 4.1 - Mean Coefficient of Thermal Expansion

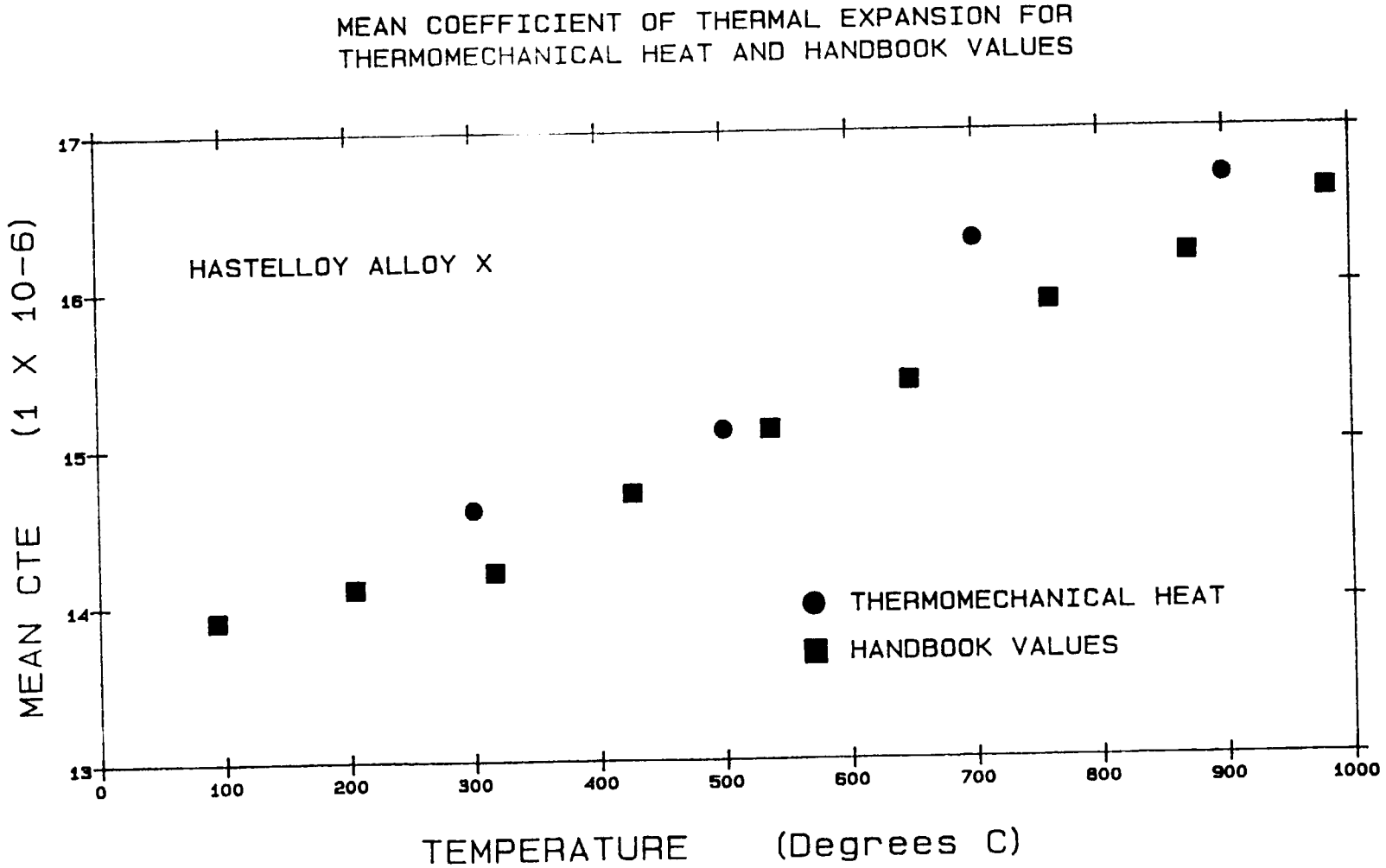

Figure 4.1 - Mean Coefficient of Thermal Expansion

continously changing. Here, if the mechanical strain component is to be subdivided, the elastic modulus must be calculated as a function of the variable temperature. This function is typically formulated from various isothermal moduli obtained at intermittent temperatures. A high–order polynomial provides sufficient interpolating accuracy. Tabulated in Table 4.2 are the various elastic moduli for this heat of Hastelloy X, as well as the values from the isothermal heat and handbook. These values are also shown in Figure 4.2. In general, the data taken from thermomechanical specimens exhibits an elastic modulus which is consistently higher than either the isothermal specimen values or the handbook values (the difference being approximately 3 to 5 percent). This minor deviation may be attributed to heat–to–heat variations in chemical composition.

4.3 Isothermal Deformation

4.3.1 Phenomenological Observations

A primary objective of this experimental study is to investigate the hardening characteristics of Hastelloy X under full thermomechanical conditions. It was noted earlier that Hastelloy X is typical of a class of materials which exhibit dynamic strain aging [1]. This phenomenon has been reported in other commonly used materials such as stainless steels [45–48]. It is typical of these materials to exhibit complex isothermal hardening trends over their full working temperature range. Shown in Figures 4.3 through 4.5 are plots of stress range verses cycle for isothermal deformation tests on Hastelloy X. All isothermal tests were performed with controlled cyclic strain amplitudes of ±0.3 %. A constant strain rate of 0.0001 s^{-1} was generated by a triangular command waveform.

ELASTIC MODULUS VALUES FOR HASTELLOY X

TEMPERATURE (Degrees C)	HANDBOOK VALUES	ISOTHERMAL HEAT	THERMOMECHANICAL HEAT
21	207	209	
93	201	201	
200			209
204	192	192	
300			197
316	185	187	
400			190
427	176	178	
482	170	179	
500			182
537	166	173	
593	160	174	
600			174
648	155	162	
700			167
704	150	157	
760	145	153	
800			157
871	135	135	
900			148
982	124	131	
1000			129

Modulus values given in GPa

Table 4.2 - Elastic Modulus Values

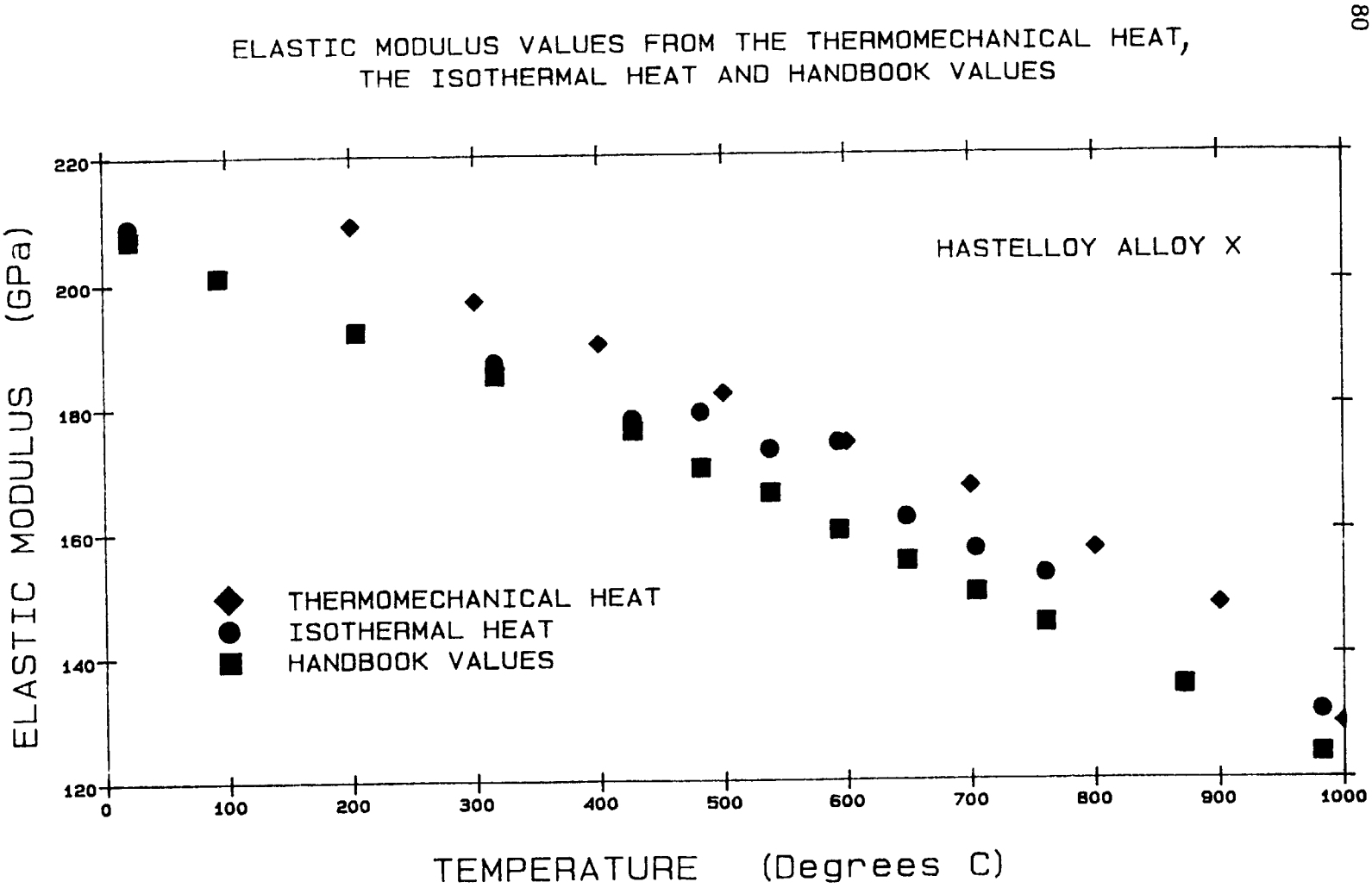

Figure 4.2 - Elastic Modulus Values

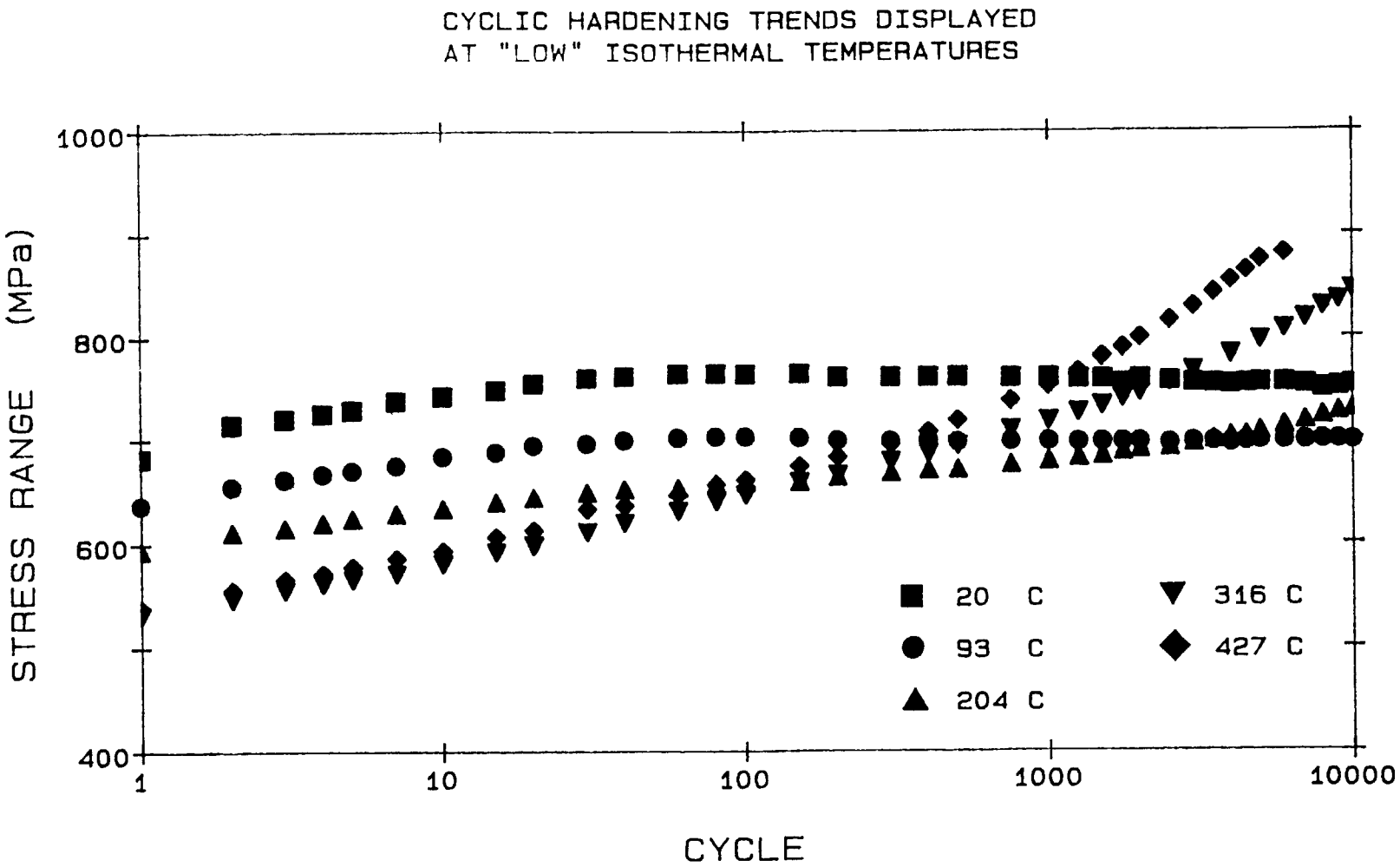

Figure 4.3 - Isothermal Hardening Trends in the 'Low' Temperature Regime

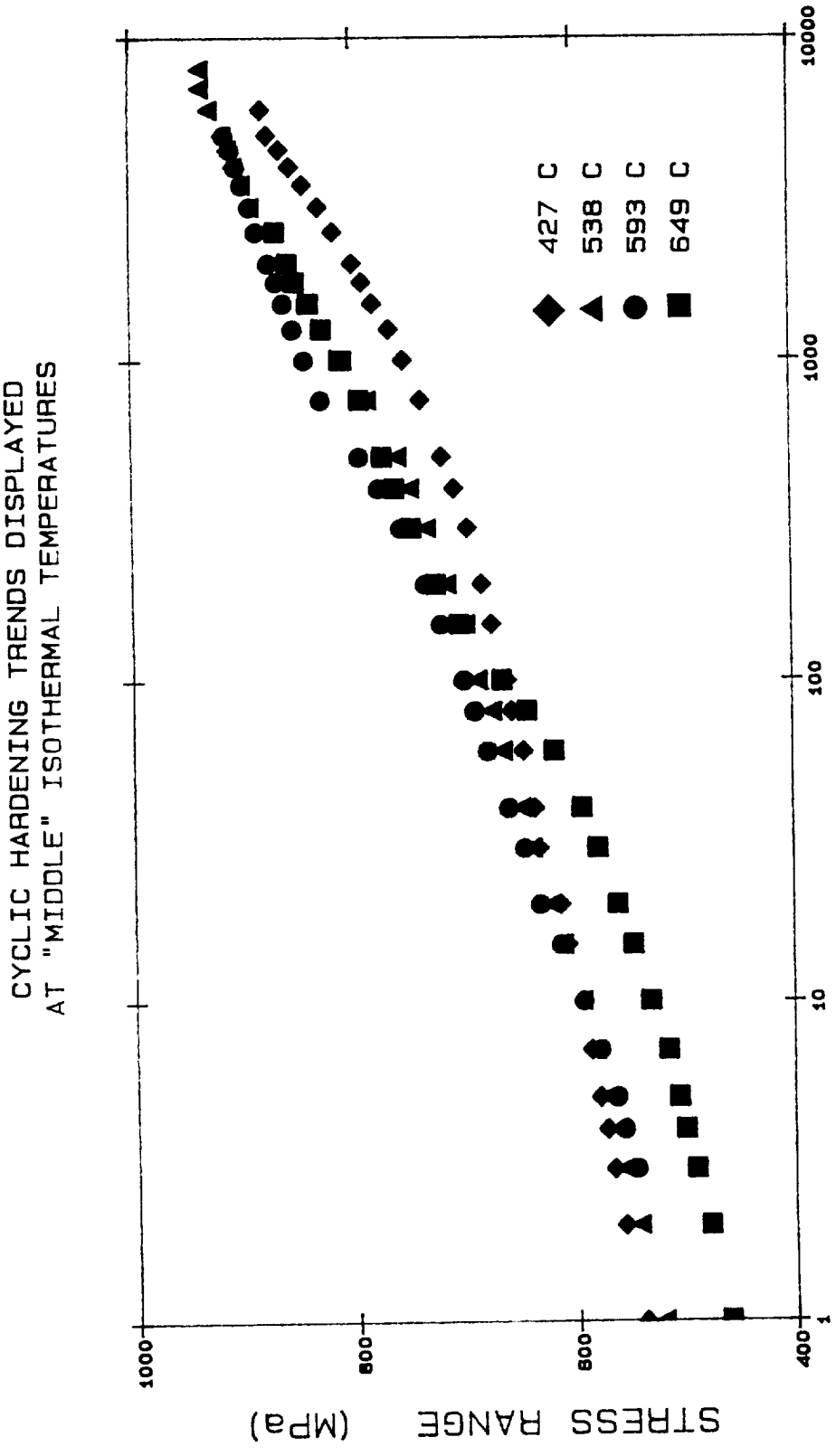

Figure 4.4 - Isothermal Hardening Trends in the 'Middle' Temperature Regime

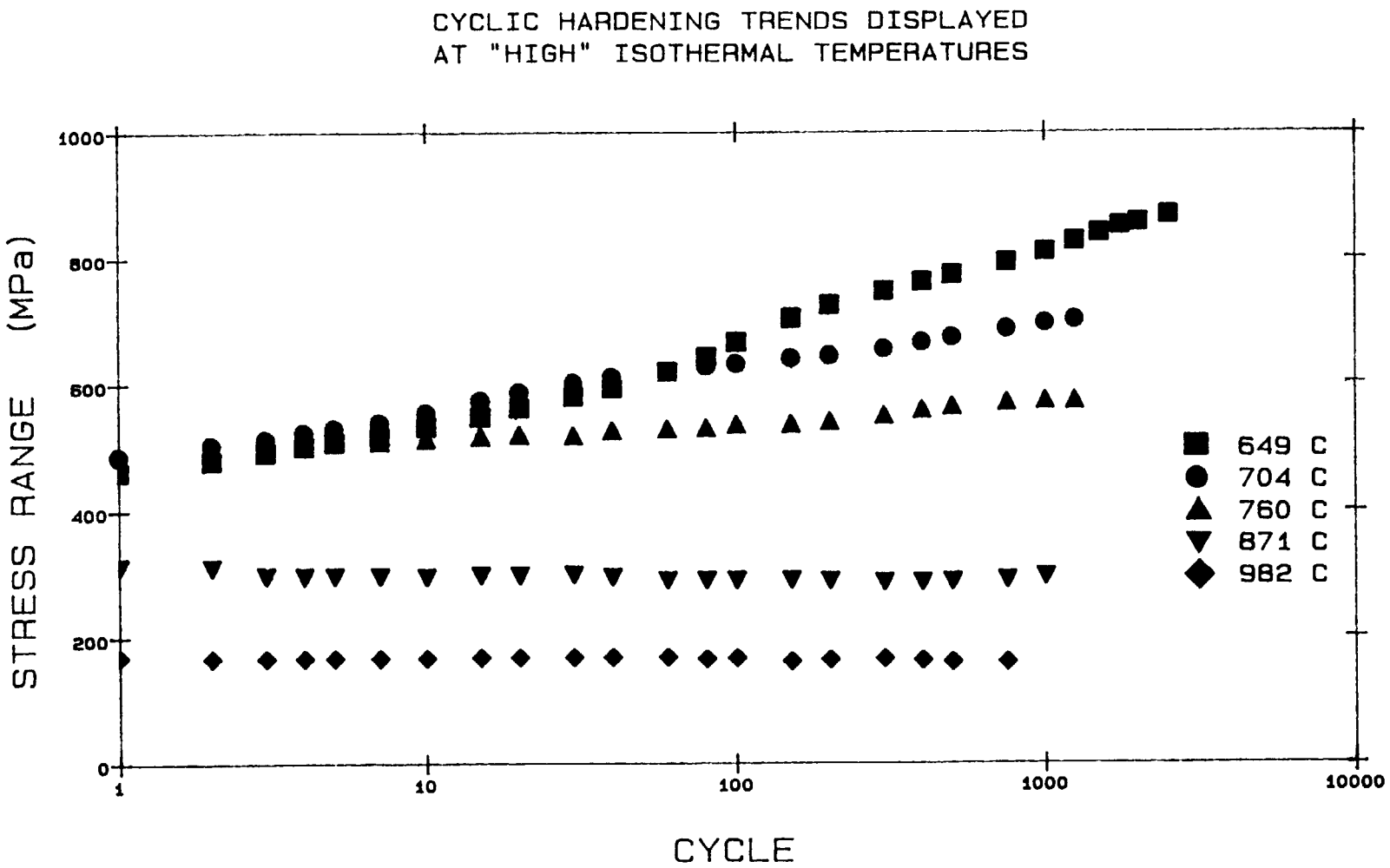

Figure 4.5 - Isothermal Hardening Trends in the 'High' Temperature Regime

Because these tests are strain controlled, the stress range (or amplitude) is allowed to increase (harden) or decrease (soften) freely. Hence, this type of plot illustrates hardening/softening characteristics of the material and therefore, the curves are typically referred to as hardening or softening curves. Figures 4.3 through 4.5 represent hardening trends over three generalized temperature regimes, namely, "low", "middle", and "high" respectively. At 93°C (200°F) (Figure 4.3), the material exhibits an overall hardening of less than 3 percent. This "near" cyclicly neutral response changes dramatically as temperatures increase. Tests performed at 204°C (400°F) and 316°C (600°F) shown an increase in stress range of 22 percent and 60 percent, respectively. This trend continues through the "low" temperature regime, with an increase in stress range of 66% realized at 427°C (800°F).

The "middle" temperature regime (Figure 4.4) is that from approximately 400 °C (750°F) to 650°C (1200°F). This regime encompasses what is typically referred to as the dynamic strain aging peak or simply the immediate temperature vicinity at which dynamic strain aging effects result in a maximum stress range and/or a maximum increase in stress range. The established isothermal hardening trend continues beyond the 427°C (800°F) condition and peaks at approximately 650°C (1200°F) where the increase in stress range is greater than 85 percent. In addition to the dramatic hardening range, the curves display a sigmoidal hardening rate which further complicates an accurate description of the materials behavior.

As the dynamic strain aging peak temperature is surpassed [i.e. $T \geq$ 650°C (1200°F)], the percent increase in stress range drops from over 85 at 650°C (1200°F), to 44 at 704 C(1300 F). The decrease continues until eventually

cyclic softening occurs during tests performed at 870°C (1600°F) and above. The phenomenological effects of dynamic strain aging on Hastelloy X are best summarized in plots such as those shown in Figures 4.6 and 4.7. Here the vertical axis changes from percent increase in stress range to stress range magnitude, respectively. Both display a well defined strain aging peak at approximately the same temperature.

4.3.2 Microstructural Observations

Microstructural examination was performed [35] on several of the isothermal tests shown in Figures 4.3 through 4.5. This work employed optical microscopy and transmission electron microscopy to identify metallurgical characteristics influencing the complex hardening behavior of Hastelloy X. General microstructural characteristics are uniquely associated with the three temperature regimes discussed above. These general characteristics can be illustrated by viewing one test from each of the three regimes. Microstructures representing the "low", "middle", and "high" temperature regimes are typified by microstuctures observed from the tests performed at 93°C (200°F), 538°C (1000°F) and 871°C (1600°F), respectively.

Shown in Figure 4.8 is a typical microstructure taken from the 93°C (200°F) isothermal test specimen. Micrographs from this specimen show a random dispersion of M_6C (molybdenum rich) carbides. One such carbide formation is shown in Figure 4.8, and appears as a relatively large circular black object. This secondary phase is typically present in the "as received" material, as noted by several of the authors reviewed in Chapter 2. The imposed test conditions (temperature and mechanical loading) do not appear to have affected

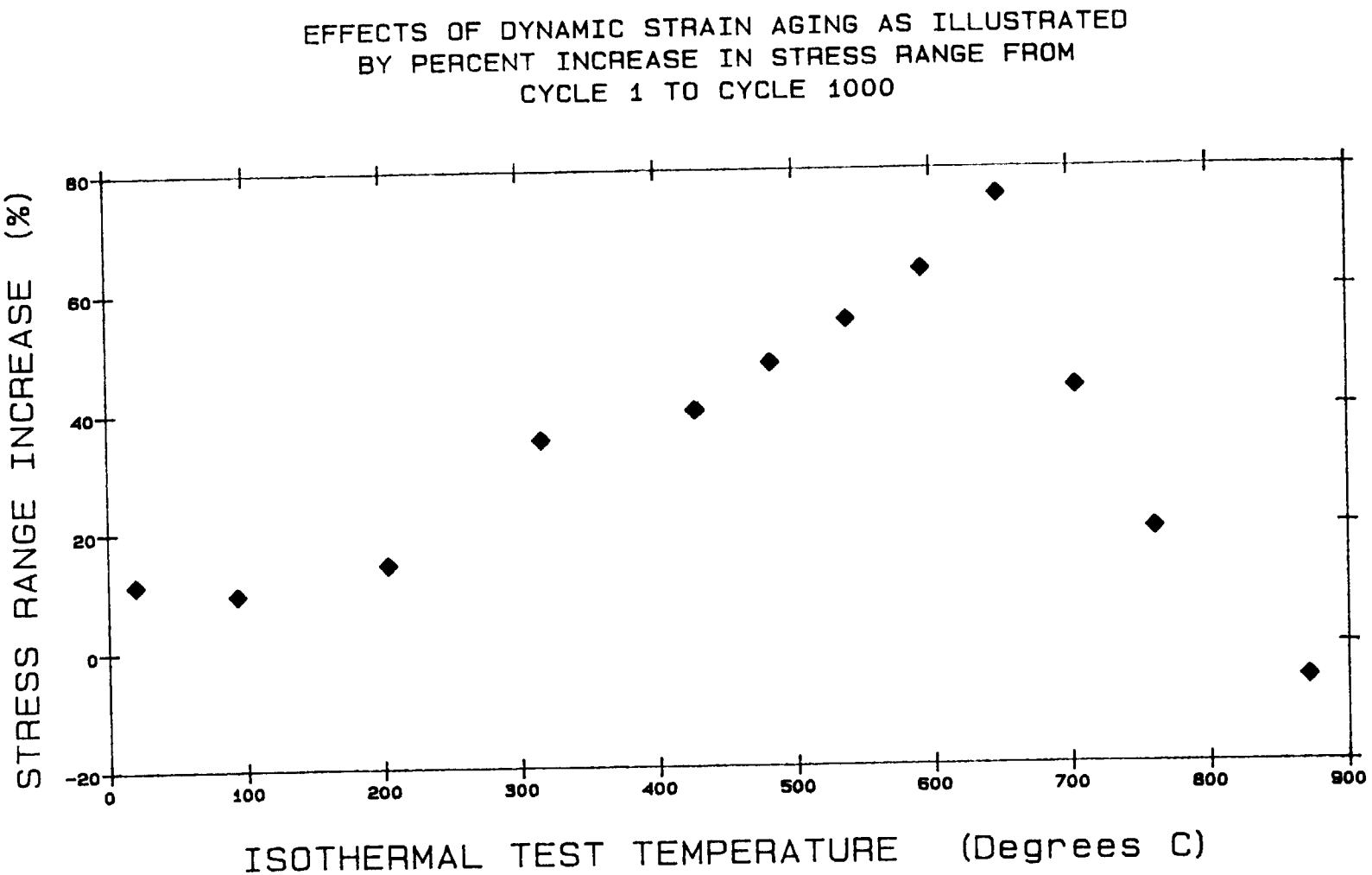

Figure 4.6 - Isothermal Dynamic Strain Aging Peak: Percent Increase Basis

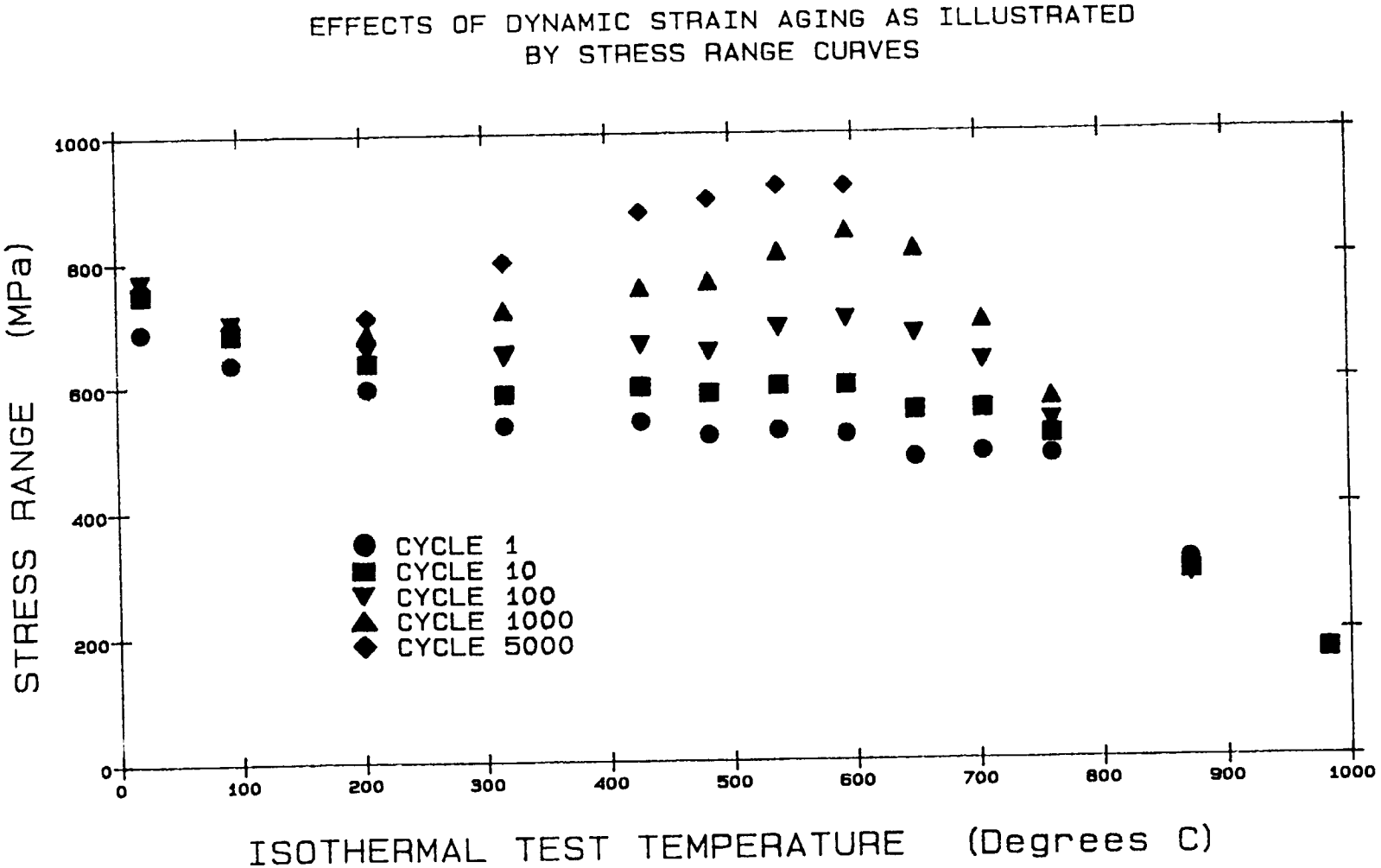

Figure 4.7 - Isothermal Dynamic Strain Aging Peak: Stress Range Magnitude Basis

A TYPICAL MICROSTRUCTURE TAKEN FROM THE 93 C ISOTHERMAL TEST SPECIMEN

Magnification = 15 500 X

The microstructure shown here is typical of those displayed by specimens tested in the "low" temperature regime

- Relatively low dislocation density
- Sparse distribution of M_6C carbides (found in the "as received" material)
- The $M_{23}C_6$ carbide phase is not present

Figure 4.8 - 93 C Isothermal Microstructure

the M_6C carbide phase, and no new phases are present. This suggests that the material remained metallurgically stable throughout the test. A relatively low dislocation density is also evident in the microstructure. This physical characteristic is compatible with the phenomenological trend of mild cyclic hardening, typically associated with the "low" temperature regime.

Shown in Figure 4.9 is a typical microstructure taken from the 538°C (1000°F) isothermal test specimen. With the aid of transmission electron microscopy, a new, extremely small phase is detected and identified as a $M_{23}C_6$ (chromium rich) carbide phase. However, at this magnification (Figure 4.9), the individual carbides are not visually detectable. The precipitation of a new phase confirms that the material has experienced a form of metallurgical instability. During material deformation, their presence interferes with the "normal" movements of the mobile dislocations. This pinning effect decreases the mobile dislocation density and correspondingly increases the immobile dislocation density. The result is a microstructure which is much stronger, and consequently, more resistant to plastic deformation. Precipitation of the $M_{23}C_6$ phase requires temperatures above approximately 500°C (932°F). However, the amount and rate of precipitation is influenced by several factors. Temperature exposure time plays a role in phase precipitation. This may be expected, as precipitation is a diffusion–type process. Mechanical deformation has been shown to also play a significant role in carbide precipitation [24,28]. This is a result of the dislocations' powerful effect on lowering the nucleation barrier and becoming the preferred nucleation sites. As precipitation occurs, the carbides energetically prefer to locate in the vicinity of mobile dislocations. Hence, The $M_{23}C_6$ phase is found to be well dispersed in intragranular locations.

A TYPICAL MICROSTRUCTURE TAKEN FROM THE 538 C ISOTHERMAL TEST SPECIMEN

Magnification = 15 500 X

The microstructure shown here is typical of those displayed by specimens tested in the "middle" temperature regime

- Extremely high dislocation density
- Very small $M_{23}C_6$ carbides have precipitated intragranularly at mobile dislocation sites resulting in dislocation pinning and blocking
- This microstructure is typically associated with the maximum hardening effects of dynamic strain aging

Figure 4.9 - 538 C Isothermal Microstructure

In addition to these strengthening carbides, micrographs taken from this specimen exhibit an extremely high dislocation density [much greater than that found at 93°C (200°F)]; this feature is clearly evidenced in Figure 4.9. This increased dislocation density also inhibits mobile dislocation movement, further amplifying the overall strengthening effect. In conclusion, the microstructural characteristics are fully compatible with the extreme phenomenological hardening experienced in the "middle" temperature regime.

Microstructures of specimens tested in the "high" temperature regime are typical of that shown in Figure 4.10. This micrograph was taken from the 871°C (1600°F) isothermal test specimen. The high temperature conditions have promoted considerable dissolution of the original M_6C carbides, which are now less numerous. The $M_{23}C_6$ carbides are easily detected at much lower magnifications as a result of having undergone considerable physical growth. This phase also appears to have migrated, or possibly re–precipitated at cell boundaries and twin boundaries. Thermal recovery processes, such as dislocation climb, are evidenced by the formation of large cells and subcells with low dislocation densities. Here, the dislocations are predominantly located at cell and twin boundaries, displaying well ordered arrangements. The depleted intragranular regions (in the presence of high thermal agitation) provide a microstructure which offers little resistance to deformation. This effect is seen as a phenomenological "weakening" of the material, consistent with trends observed in the "high" temperature regime.

A TYPICAL MICROSTRUCTURE TAKEN FROM THE 871 C ISOTHERMAL TEST SPECIMEN

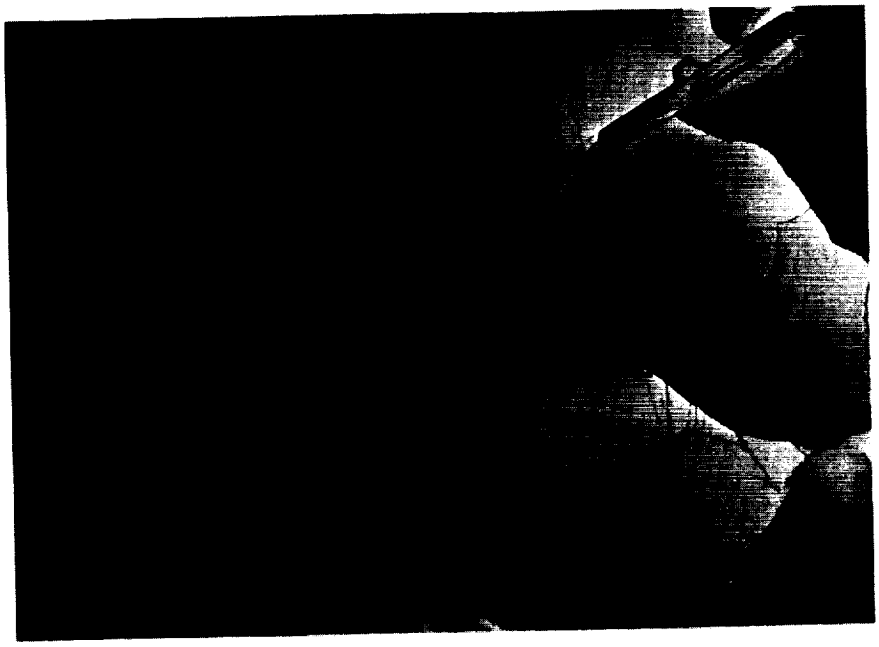

Magnification = 8 300 X

The microsturcture shown here is typical of those displayed by specimens tested in the "high" temperature regime

- Large cell and subcell structures
- Low intragranular dislocation density
- Dislocations predominantly located at grain boundaries in orderly arrangements
- $M_{23}C_6$ carbides have evolved into a much larger state

Figure 4.10 - 871 C Isothermal Microstructure

4.4 Thermomechanical Deformation

4.4.1 Phenomenological Observations

The thermomechanical test matrix can be divided into four major temperature regimes, namely, 200°C to 400°C (392°F to 752°F), 400°C to 600°C (752°F to 1112°F), 600°C to 800°C (1112°F to 1472°F), and 800°C to 1000°C (1472°F to 1832°F). Tests involving both in–phase and out–of–phase conditions were conducted at each of these ranges. One of the main objectives of this study is to determine if the thermomechanical hardening trends of Hastelloy X are similar to those found under isothermal conditions. A difficulty arises here when attempting to compare thermomechanical data with isothermal data. This is because a single thermomechanical test involves a wide range of temperatures and a single isothermal test by definition involves a single temperature. Methodology typically used involves presenting the thermomechanical data along with "bounding" isothermal data. Here "bounding" refers to the upper and lower test temperature. For example, a thermomechanical test with a temperature range from 200°C to 400°C (392°F to 752°F) is presented in comparison with isothermal tests performed at 200°C (392°F) and at 400°C (752°F). This technique is used for comparison of phenomenological trends (i.e. hardening range and rate) and material deformation (hysteresis loops).

Initial comparisons of material response will be made on the basis of stress range verses cycles. Shown in Figure 4.11 are results from thermomechanical tests performed with a temperature range from 200°C to 400°C (392°F to 752°F). The four curves represent data taken from an in–phase test, out–of–phase test, and the two bounding isothermal tests. Here, both in–phase and out–of–phase test conditions produce initial stress ranges

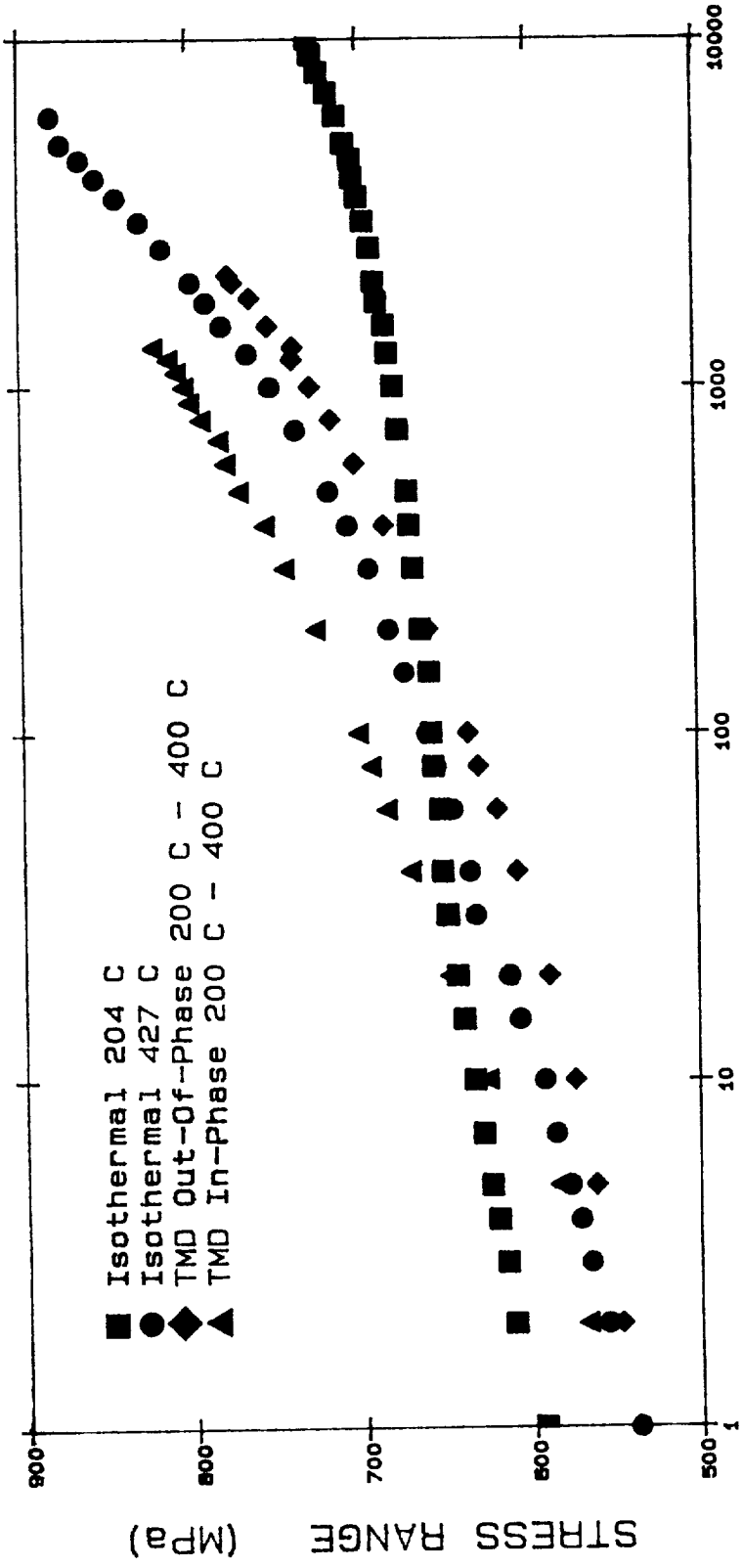

Figure 4.11 - Thermomechanical Stress Range Response at 200 C to 400 C

comparable to the 427°C (800°F) isothermal test. The out–of–phase data displays a relatively steady and gradual log–based increase in stress range, where both the range and rate are closely approximated by the 427°C (800°F) isothermal data throughout the test. However, early in the test, the in–phase specimen experiences a much higher hardening rate. This enables the in–phase data to exceed the bounding isothermal curves after approximately 40 cycles. Once having established this comparatively high stress range, the in–phase test continues to harden with a rate comparable to that of the 427°C (800°F) isothermal test. Consequently, the in–phase hardening path shown in Figure 4.11 remained outside the boundaries established by the isothermal data.

The next thermomechanical data discussed is that involving a temperature range from 400°C to 600°C (752°F to 1112°F). It is important to note that the "hot" end of the thermomechanical cycle is in the immediate vicinity of the isothermal dynamic strain aging peak temperature (see Figure 4.6 and Figure 4.7). This concurrence will be shown to have a significant bearing upon the microstructural physics and resulting phenomenological observations. Shown in Figure 4.12 are the thermomechanical results from the 400°C to 600°C (752°F to 1112°F) temperature range. As before, the in–phase, out–of–phase, and bounding isothermal tests are shown. At first view, a significant observation can be made; the material subjected to thermomechanical loading hardened to a stress range well beyond that experienced under isothermal conditions. Thermomechanical hardening trends established in this temperature range also show a greater deviation from the isothermal trends than their counterparts had shown in the 200°C to 400°C (392°F to 752°F) range. Initially, the thermomechanical hardening range and rate closely resemble that displayed by

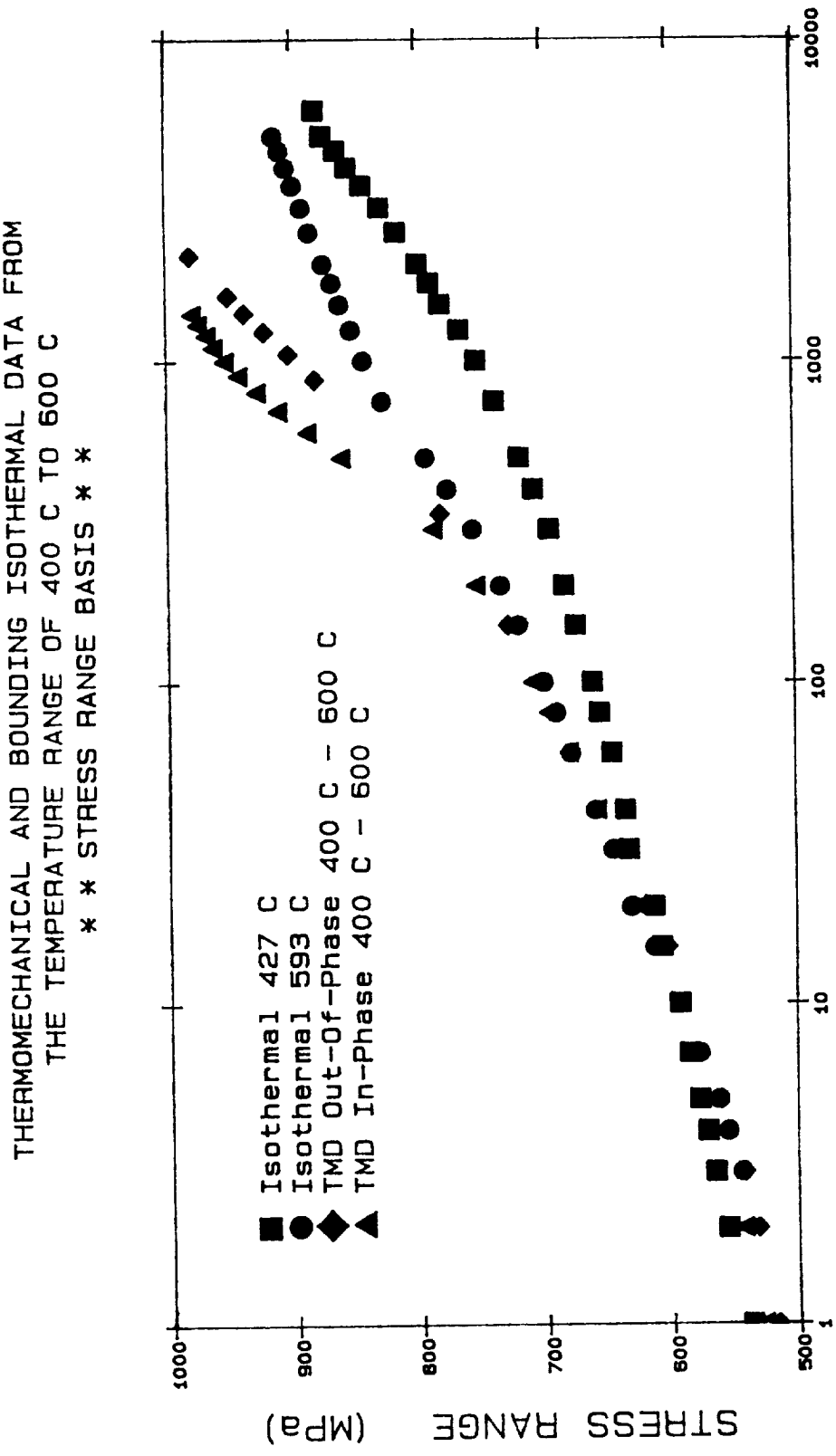

Figure 4.12 - Thermomechanical Stress Range Response at 400 C to 600 C

the 593°C (1100°F) isothermal data. At approximately 400 cycles, both the in–phase and out–of–phase tests begin to show an increased hardening rate [relative to the 593°C (1100°F) isothermal rate] which was maintained throughout the test. Again, as found in the 200°C to 400°C (392°F to 752°F) temperature range, in–phase conditions display stress ranges which are higher than those obtained under out–of–phase conditions.

Shown in Figure 4.13 are the data obtained from in–phase, out–of–phase, and bounding isothermal tests in the temperature range from 600°C to 800°C (1112°F to 1472°F). Initial stress ranges experienced by both the in–phase and out–of–phase tests resemble those found in the isothermal test performed at 593°C (1100°F). However, the thermomechanical data did not remain even remotely coincidental with either of the isothermal paths. This observation is contrary to those made from the tests performed below 600°C (1112°F). The one correlation which was maintained pertained to the hardening rate. Here, the thermomechanical data was found to harden at a rate representative of the test performed at 815°C (1500°F). Specifically, all three tests show an insignificant amount of hardening, and appear to be near cyclicly neutral. With respect to the thermomechanical tests, this suggests that the thermal recovery effects associated with temperatures in the vicinity of 800°C (1472°F) are strong enough to nullify the hardening effects associated with temperatures in the vicinity of 600°C (1112°F). In contrast to the thermomechanical trends revealed at lower temperatures, the in–phase and out–of–phase data maintain a strong correlation throughout the entire test. This again suggests that the thermal recovery effects are overriding other factors

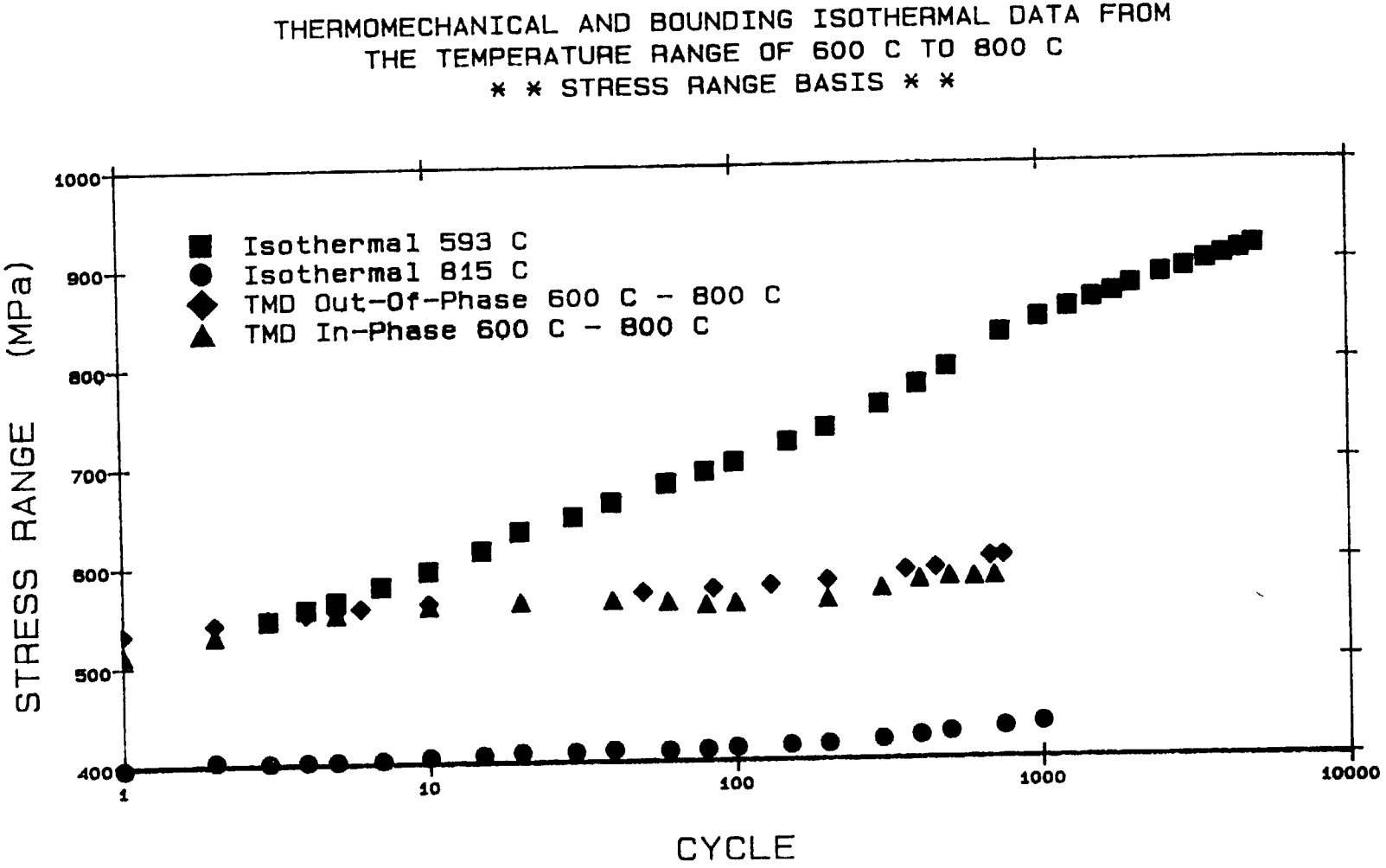

Figure 4.13 - Thermomechanical Stress Range Response at 600 C to 800 C

which may lead to differences between compressive and tensile behavior. In general, the overall thermomechanical hardening trends are well bounded by the trends revealed under isothermal conditions.

The final temperature range examined is that from 800°C to 1000°C (1472°F to 1832°F). The data is given in typical fashion in Figure 4.14. At these high homologous temperatures, the material will tend to flow freely and offer little resistance to mechanical deformation. Here thermal recovery effects completely nullify any hardening behavior and, consequently, cyclic softening is commonly displayed. The thermomechanical hardening trends are typified by the isothermal data, with respect to both stress range and hardening rate.

Two noteworthy difficulties were encountered during the thermomechanical tests. First, the significant drop in stress range experienced by the in–phase test after cycle 100, is attributed to the onset of specimen buckling. The specimen design employed here (design #1) was not adequate for this particular case of loading, and as a result, specimen stability was not maintained throughout the entire test. Second, the out–of–phase test experienced specimen barrelling [37–41]. However, through the use of thermal gradients (see Section 3.7.2), the barreling was forced to occur primarily outside the specimen's gauge section. Therefore, the results reported here are felt to be accurate and reliable.

One phenomenological trend was consistently displayed throughout all four temperature ranges. The thermomechanical hardening rates were dominated by the "hot" end of the cycle. The hardening rate of the bounding "hot" isothermal test is notable more representative of the thermomechanical hardening rate (in comparison with the bounding "cold" isothermal test).

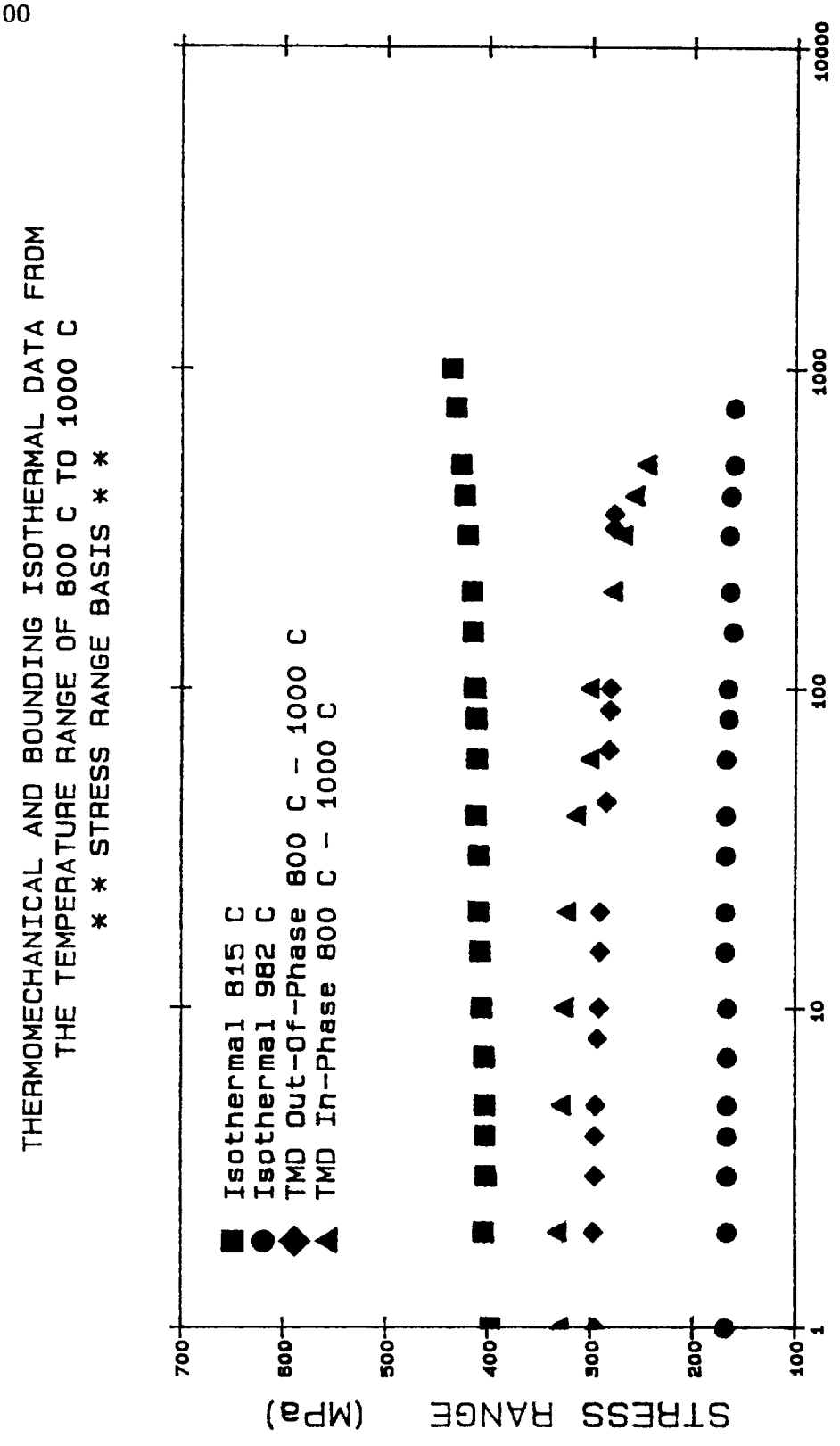

Figure 4.14 - Thermomechanical Stress Range Response at 800 C to 1000 C

This behavior is best illustrated in Figure 4.12 by the 400°C to 600°C (752°F to 1112°F) thermomechanical tests and the 593°C (1100 F) isothermal test. The visual advantage here arises from the coincidental nature of the three curves.

Upon reviewing the stress range verses cycle plots described above (Figures 4.11 through 4.14), the thermomechanical results can be generalized into two main categories, namely, results which were "contained" within the bounding isothermal tests, and results which were not well bounded. The thermomechanical tests performed at temperatures above 600°C (1112°F) exhibited behavioral trends which appear to be dominated by thermal recovery effects. Hence, their general behavior is somewhat "predictable" given the appropriate isothermal tests. With this in mind, these tests will not be analyzed further on a phenomenological basis. This is not to imply that other forms of this data (i.e. hysteresis loops and inelastic strain plots) cannot be used to gain insight into the various differences between thermomechanical and isothermal deformation. But rather, it is suggested here that the results do not have significant bearing upon the objective of this study. In contrast, the thermomechanical tests performed at temperatures below 600°C (1112°F) involve behaviors which could not have been predicted from the bounding isothermal data. In these cases, a more detailed analysis of the phenomenological trends will be pursued in an effort to better understand the mechanisms of such behavior.

Plots of stress range versus cycle serve well to illustrate general hardening trends, but hidden within the composition of the stress range are the two individual amplitudes. For fully reversed isothermal tests, both stress amplitudes (tensile and compressive) are well represented by simply halving the

stress range. This methodology relies upon the assumption that material hardens similarly in tension and compression; a safe assumption for this and most materials. Therefore, trends observed in the stress range (at full magnitude) are exactly those observed in the stress amplitudes (at half magnitudes). However, this is most likely not the case for fully reversed thermomechanical tests. Here, as a result of dynamic temperature conditions, the strength of the material (stress–strain relationship) is constantly changing. And more importantly, the difference in this relationship is at a maximum at the two opposing amplitudes. Given this condition, a thermomechanical cycle will almost certainly involve asymmetric stress amplitudes. Therefore, trends represented by the stress amplitudes may vary considerably (depending upon the temperature range) from those displayed by the stress ranges. With this in mind, the thermomechanical tests of interest are further analyzed on the basis of stress amplitudes.

A methodology similar to that used in the stress range plots will be used to make comparisons between isothermal and thermomechanical stress amplitude trends. The stress amplitudes established at the "cold" temperature of the cycle will be compared with stress amplitudes from the bounding "cold" isothermal test. Likewise, the stress amplitudes established at the "hot" end of the thermomechanical cycle will be compared with data taken from an appropriately bounding "hot" isothermal test. The signs associated with the thermomechanical stress amplitudes will be plotted as they naturally occurred during the test. For example, an out–of–phase thermomechanical test from 200°C to 400°C (392°F to 752°F) will involve positive stress amplitudes occurring at the 200°C (392°F) end of the cycle and negative stress amplitudes occurring at the 400°C (752°F) end of the cycle. Thus, positive stress

amplitudes will be shown from the bounding "cold" isothermal test, and negative stress amplitudes will be shown from the bounding "hot" isothermal test.

Shown in Figure 4.15 is data taken from the 200°C to 400°C (392°F to 752°F) out–of–phase thermomechanical test, plotted along with appropriate isothermal stress amplitudes. Upon viewing the "hot" end of the cycle, the thermomechanical hardening trend is seen to be well bounded and closely approximated by the 427°C (800°F) isothermal data. However, the stress amplitudes incurred at the "cold" end of the thermomechanical cycle exceed the isothermal level at approximately cycle 100. This increased hardening rate [relative to the 204°C (400°F) isothermal hardening rate] is maintained and enables the "cold" thermomechanical stress amplitude to harden well above what may have been expected at this temperature. This out–of–phase test was shown to be well bounded in the stress range plot (Figure 4.11). The scatter appearing late in the test (Figure 4.15) is not a typical material response. These "steps" or "jogs" in the data were caused by unanticipated test interruptions.

Shown in Figure 4.16 is a comparable plot illustrating the stress amplitude trends of the in–phase thermomechanical test performed from 200°C to 400°C (392°F to 752°F). Recalling from the earlier discussion and Figure 4.11, this condition was found to promote hardening ranges which were not bounded by the isothermal stress ranges. Figure 4.16 displays tremendous agreement between the "hot" stress amplitudes of the thermomechanical data and the 427°C (800°F) isothermal stress amplitudes. However, the "cold" end of the in–phase thermomechanical cycle is shown to harden well beyond the 204°C (400°F) isothermal stress amplitudes. This trend was revealed in the 200°C to 400°C (392°F to 752°F) out–of–phase experiment, but to a lesser degree. For

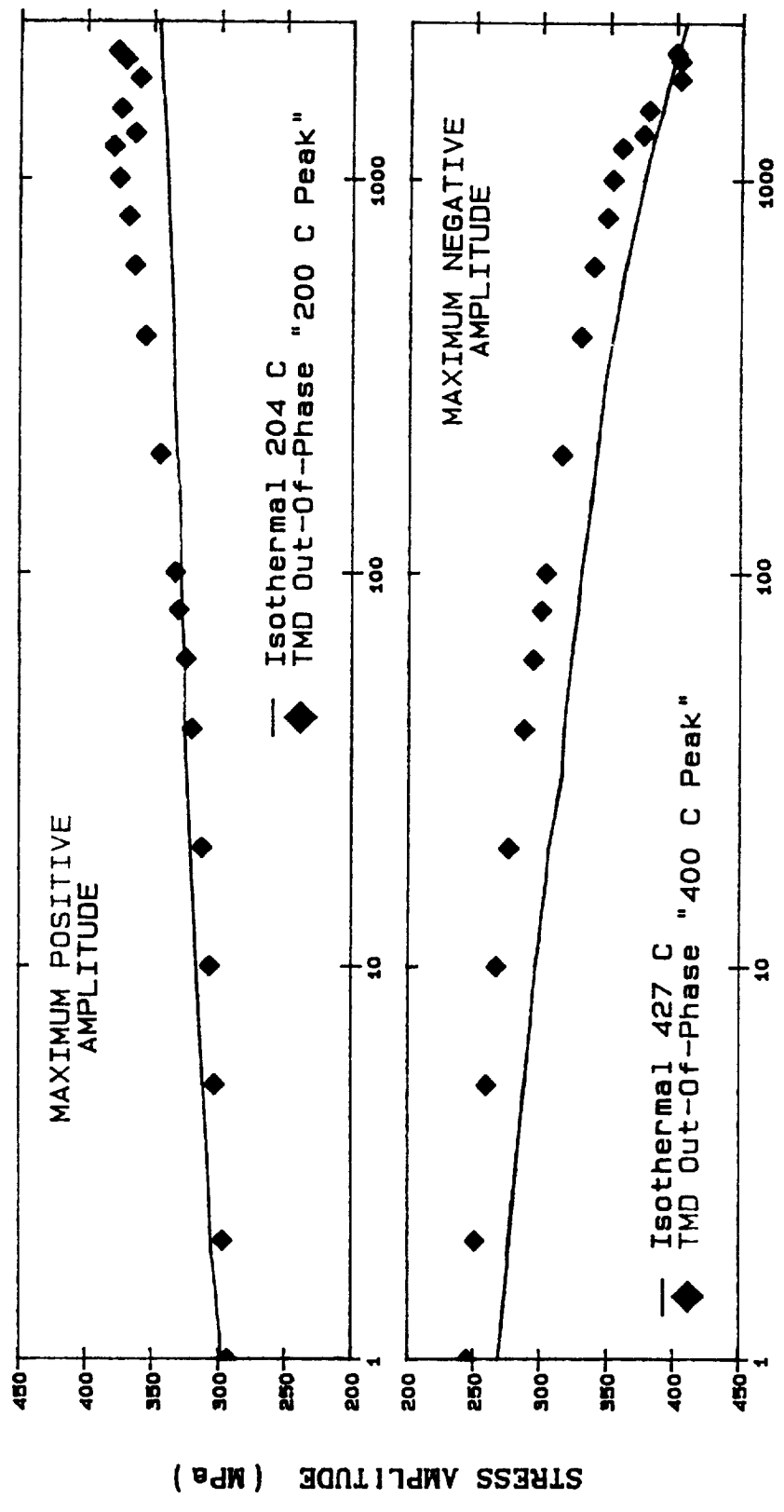

Figure 4.15 - Stress Amplitudes for 200 C to 400 C Out-Of-Phase Conditions

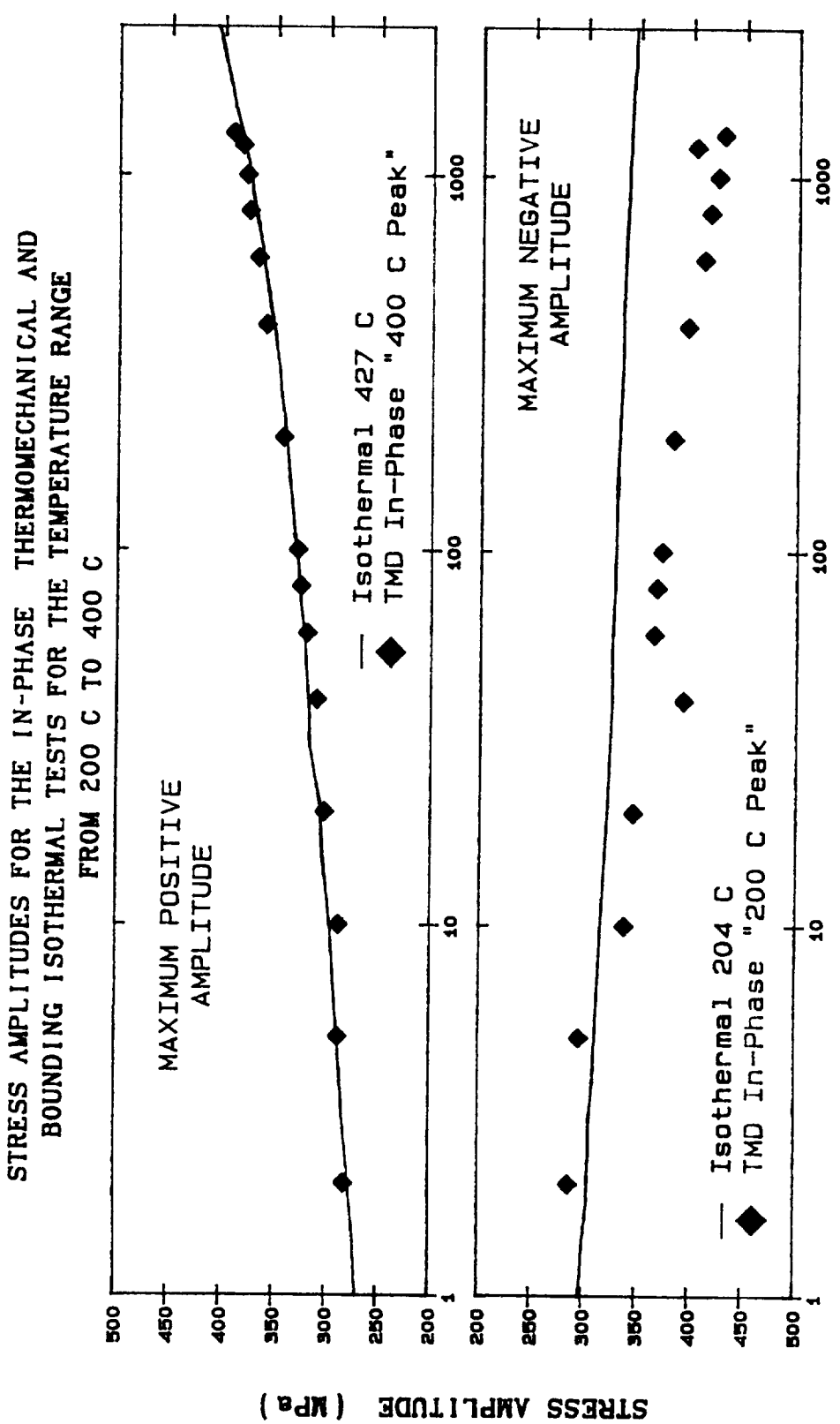

Figure 4.16 - Stress Amplitudes for 200 C to 400 C In-Phase Conditions

the in–phase condition, the "cold" end hardening is severe enough to actually surpass the hardening which occurred at the "hot" end of cycle, and thus also surpassing the hardening observed in the 427°C (800°F) isothermal test. It is this occurrence which enables the stress range to exceed that which is displayed by the 427°C (800°F) isothermal test.

Shown in Figure 4.17 are the stress amplitude trends established in the 400°C to 600°C (752°F to 1112°F) out–of–phase thermomechanical experiment. Recalling from earlier discussion and Figure 4.12, the stress ranges experienced by both the in–phase and out–of–phase data were not bounded by isothermal trends. As seen in Figure 4.17, the thermomechanical amplitude trends established in the previous temperature range are also shown here. The "hot" stress amplitudes follow precisely along the path established by the 593°C (1100°F) isothermal test, whereas, the thermomechanical "cold" stress amplitudes clearly show significant deviation from the 427°C (800°F) isothermal test. More specifically, the "cold" stress amplitude is found to harden well beyond that which is experienced at 593°C (1110°F) under isothermal conditions. This event takes on added significance because the temperature of 593°C (1110°F) represents the dynamic strain aging peak temperature. At no other isothermal temperature does Hastelloy X experience a greater increase in hardening. Thus, the 400°C (752°F) thermomechanical stress amplitudes found here reveal a material behavior which is never experienced under isothermal conditions.

Shown in Figure 4.18 are similar plots representing the in–phase thermomechanical response. So as not to belabor the point, it is sufficient to say that the exact same trends and state of events are revealed here. However, one

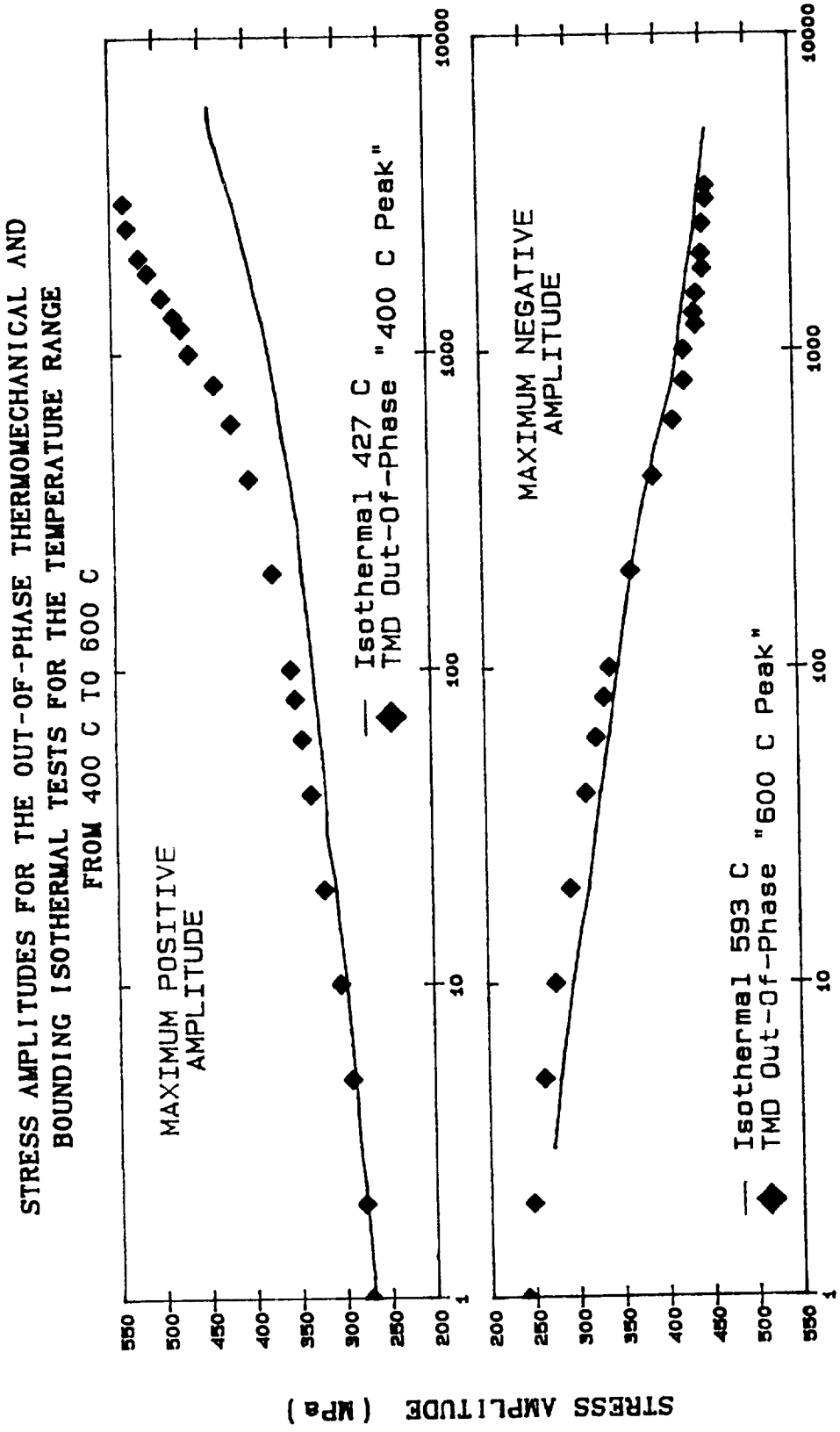

Figure 4.17 - Stress Amplitudes for 400 C to 600 C Out-Of-Phase Conditions

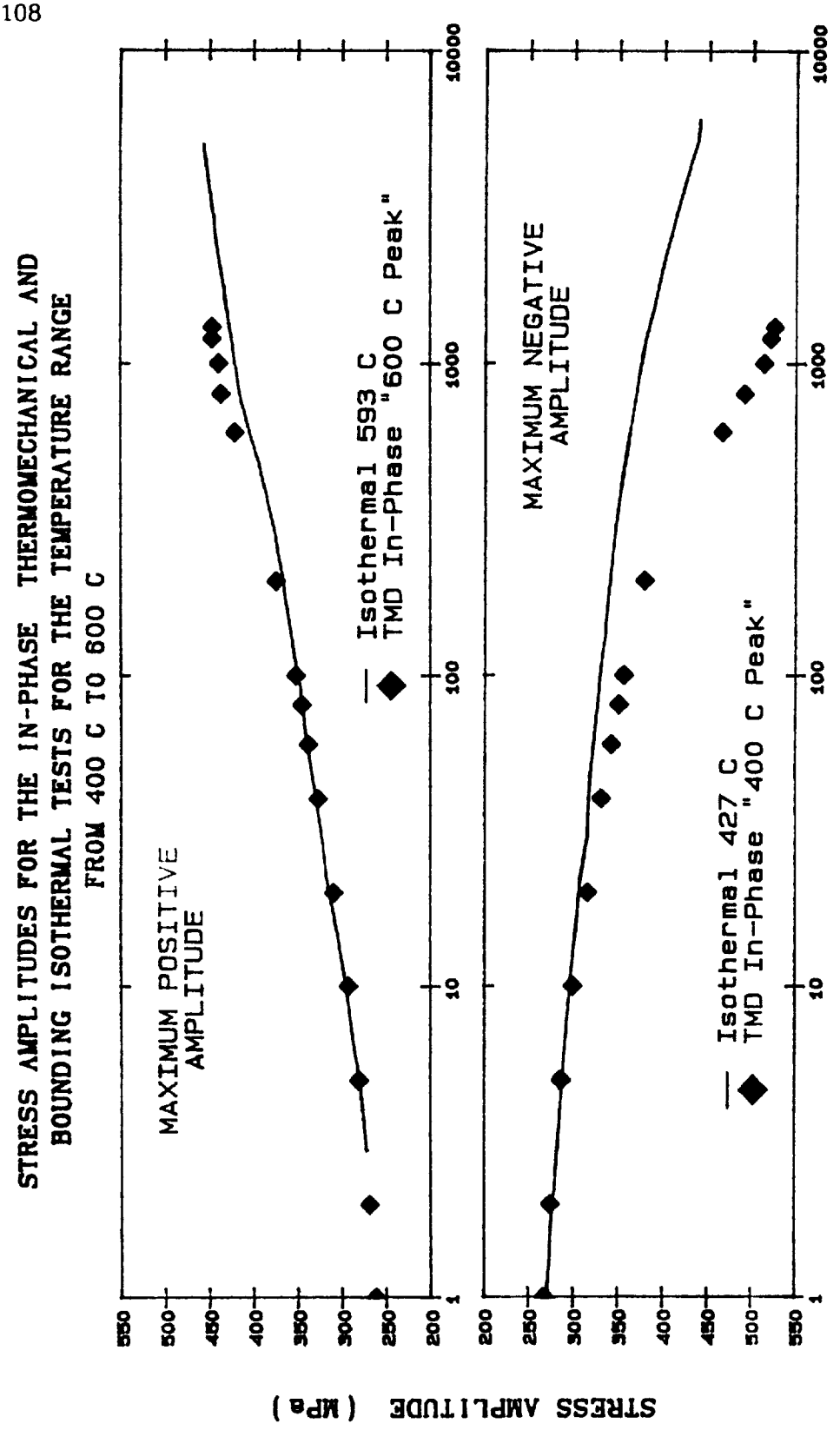

Figure 4.18 - Stress Amplitudes for 400 C to 600 C In-Phase Conditions

noteworthy difference between the out–of–phase and in–phase response exists, namely, the "cold" amplitude was found to harden more severely in the in–phase test.

The phenomenological thermomechanical hardening trends examined portray a consistent story. Tests conducted below 600°C (1112°F) are shown to harden with rates similar to those display by their respective bounding "hot" isothermal tests. In most cases, these tests were shown to exceed the hardening ranges set forth by the isothermal data. Upon further analysis, the extreme hardening behavior was found to be occurring at the "cold" end of the cycle. By viewing the isothermal database, it is the "cold" end of the thermomechanical cycle which is least expected to exhibit the majority of hardening. Thermomechanical tests conducted above 600°C (1112°F) revealed hardening trends which were well bounded by their respective bounding isothermal tests. It was concluded that material behavior at these relatively high temperatures is influenced by dominant thermal recovery effects.

4.4.2 Microstructural Observations

Although several significant conclusions can be made about the macroscopic thermomechanical behavior (based on the clear phenomenological trends exhibited) of Hastelloy X, little can be concluded about the mechanisms driving this unique behavior. More specifically, the question remains: What enables this material to exhibit these unique hardening trends under thermomechanical conditions ? This question is answered through a microstructural investigation. Here physical mechanisms will be identified and shown to support, and promote the observed phenomenological trends.

Shown in Figures 4.19 and 4.20 are micrographs taken from the out–of–phase 200°C to 400°C (392°F to 752°F) thermomechanical test. This test is performed in what was previously referred to as the "low" isothermal temperature regime [T $\leq$ 400°C (752°F)] in Section 4.3 Therefore, initial comparisons will be made with the isothermal microstructure presented as being typical of this temperature regime (see Figure 4.8). Similar to the isothermal microstructure, the thermomechanical microstructure contained a sparse presence of the M_6C carbide phase. As stated before, this phase is typically found in the "as received" material, and does not necessarily suggest that phase precipitation has occurred during the test. Also similar to the isothermal "low" temperature microstructure, the $M_{23}C_6$ phase was not present. [It is this phase ($M_{23}C_6$) which is responsible for promoting the dynamic strain aging.] However, unlike the isothermal microstructure, the 200°C to 400°C (392°F to 752°F) microstructure displays a very high dislocation density. This contrast is illustrated by comparing Figure 4.19 with Figure 4.8, where the magnification levels are identical. Figure 4.20 displays this same general area, where a much higher magnification enables the individual dislocations to be viewed. Under isothermal conditions, this high dislocation density is typically associated with tests performed at or above 400 C°(752°F). This suggests that the physics of the thermomechanical microstructure are dominated by events which tend to occur at the hottest temperature of the cycle, even though over 95 percent of the cycle period is spent below this temperature. Given this high dislocation density [not typically associated with temperatures below 400°C (752°F)], the unique phenomenological hardening trends can be explained. Recalling Figures 4.15 and 4.16, the "hot" end stress amplitudes were found to follow the bounding "hot"

A TYPICAL MICROSTRUCTURE TAKEN FROM A
200 C to 400 C THERMOMECHANICAL TEST SPECIMEN

Magnification = 15 500 X

This thermomechanical microstructure exhibits features associated with isothermal tests performed at approximately 400 C

- Extremely high dislocation density
- Sparse scattering of M_6C carbides
- The $M_{23}C_6$ phase is not present

Figure 4.19 - 200 C to 400 C Thermomechanical Microstructure at 15 500 X

A TYPICAL MICROSTRUCTURE TAKEN FROM A 200 C to 400 C THERMOMECHANICAL TEST SPECIMEN

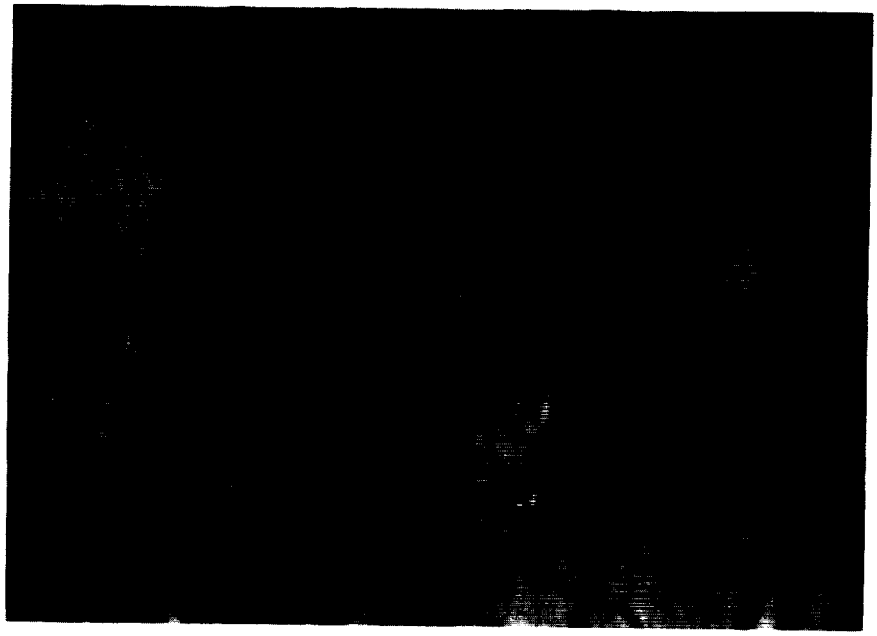

Magnification = 142 600 X

- Higher magnification enables individual dislocations to be viewed
- Even without the $M_{23}C_6$ carbide phase, the dense, tangled nature of the dislocation structure promotes significant hardening

Figure 4.20 - 200 C to 400 C Thermomechanical Microstructure at 142 600 X

isothermal data. The reason for this trend is now clear because the two microstructures have been shown to be very similar. However, upon viewing the "cold" end amplitudes, it was shown that the trend is not similar to that exhibited by the bounding "cold" isothermal test. This is a consistent result, as the two microstructures are significantly different. The thermomechanical microstructure is physically more dense, and thus "stronger" than that which is present during the 204°C (400°F) isothermal test. Now, considering that this "400°C (752°F) microstructure" is experiencing comparable strains at much lower temperatures, it has the potential to harden, not only equal to, but above the amplitudes displayed at 400°C (752°F). The increased hardening [in excess of that seen at 400°C (752°F) under isothermal conditions] results from a decreased thermal agitation in the microstructure. This same effect is that which causes a material's modulus (strength) to be inversely proportional to temperature. Thus, the phenomenological trends are well supported by the physical nature of the microstructure.

Shown in Figures 4.21, 4.22 and 4.23 are typical micrographs taken from the out–of–phase 400°C to 600°C (752°F to 1112°F) thermomechanical specimen. This temperature range is representative of the "middle" temperature regime discussed in Section 4.3. The isothermal temperature selected as typifying microstructures in this regime was 538°C (1000°F) (Figure 4.9). In general, the thermomechanical microstructure is very similar to that from the isothermal test. Here, Figure 4.21 and Figure 4.9 display micrographs taken at identical magnifications. Both microstructures contain high dislocation densities. Viewing individual dislocations requires a much higher magnification, such as that shown in Figure 4.22. This dark field image (so called) illustrates the

A TYPICAL MICROSTRUCTURE TAKEN FROM A 400 C to 600 C THERMOMECHANICAL TEST SPECIMEN

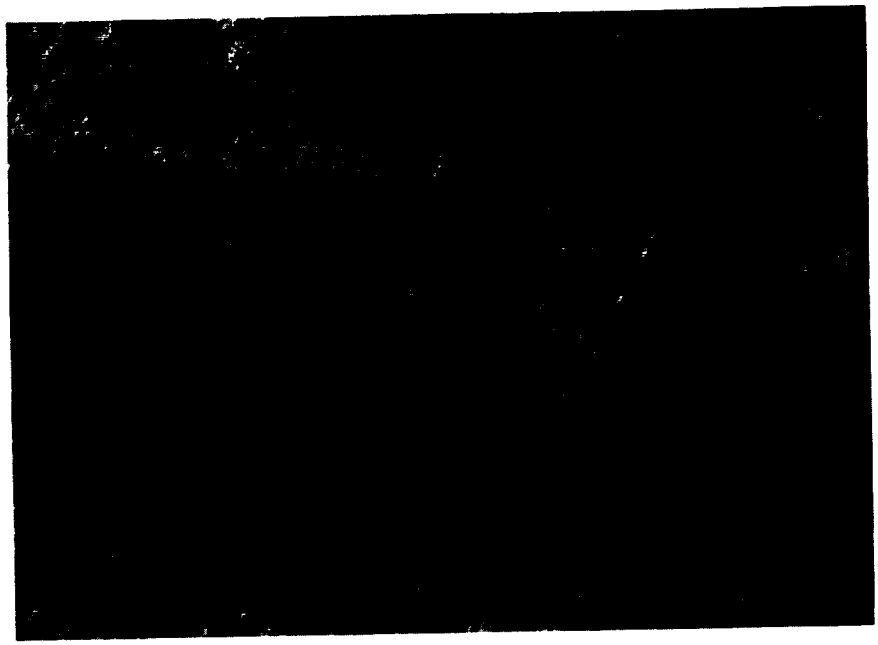

Magnification = 15 500 X

This thermomechanical microstructure exhibits features associated with isothermal tests performed in the vicinity of the dynamic strain aging peak temperature

- Extremely high dislocation density
- Intragranular regions infested with small $M_{23}C_6$ carbides effective at pinning dislocations
- This microstructure is typically associated with the maximum hardening effects of dynamic strain aging

Figure 4.21 - 400 C to 600 C Thermomechanical Microstructure at 15 500 X

A TYPICAL MICROSTRUCTURE TAKEN FROM A
400 C to 600 C THERMOMECHANICAL TEST SPECIMEN

Magnification = 142 600 X

- Higher magnification enables individual dislocations to be viewed
- Dark field image reveals dislocations as white or light curvilinear objects

Figure 4.22 - 400 C to 600 C Thermomechanical Microstructure at 142 600 X: Dislocations

A TYPICAL MICROSTRUCTURE TAKEN FROM A
400 C to 600 C THERMOMECHANICAL TEST SPECIMEN

Magnification = 142 600 X

- This magnification enables the very small $M_{23}C_6$ phase to be displayed
- Dark field image reveals individual $M_{23}C_6$ carbides in white

Figure 4.23 - 400 C to 600 C Thermomechanical Microstructure at 142 600 X: Carbides

dislocations as white, or light curvilinear segments. A significant amount of small $M_{23}C_6$ carbides have precipitated intragranularly at dislocation sites. This phase is evident (in white) in Figure 4.23, where a different view of dark field imagery is shown. Again, a sparse distribution of the comparatively large, original M_6C phase was found to be present. There are no obvious differences between the thermomechanical and isothermal microstructures. With this in mind, the phenomenological trends are re–examined. Recalling Figures 4.17 and 4.18, the "hot" end amplitudes strongly agree with the bounding "hot" isothermal amplitudes. This again is a result of the similar microstructures. In contrast, the bounding "cold" isothermal test displays a microstructure which is drastically different from that shown in Figures 2.21 through 4.23. The $M_{23}C_6$ phase requires a temperature of approximately 500°C (932°F) to initiate precipitation. This "threshold" temperature is obviously never experienced during isothermal tests performed at, or just above 400°C (752°F). Consequently, the hardening experienced by such isothermal tests is not aided by the presence of this secondary phase. Thus, the hardening trend established by the 427°C (800°F) isothermal test is a function of the degree of thermal agitation and the high dislocation density (no $M_{23}C_6$ carbides). It is now clear that the "cold" end amplitudes of the thermomechanical cycle should exceed the amplitudes experienced by the 427°C (800°F) isothermal test. This, resulting from the presence of the $M_{23}C_6$ phase which provides a high degree of dislocation pinning. It is also evident why the "cold" amplitudes of the thermomechanical test are capable of exceeding those experienced at the "hot" end (and thereby exceeding those displayed by the bounding "hot" isothermal test). Here, the same microstructure (inundated with $M_{23}C_6$ carbides) is forced to deform an

equal amount (fully reversed strain) in the presence of a much lower degree of thermal agitation. This forced deformation will now require a much higher stress. By linking the microstructural physics with the dynamic temperature condition, the unique phenomenological trends are well supported.

Thermomechanical tests involving temperatures above 600°C (1112°F) exhibited phenomenological trends which were strongly influenced by thermal recovery processes. These trends are well supported by the microstructures shown in Figures 4.24 through 4.27. Shown in Figures 4.24 and 4.25 are micrographs taken from the out–of–phase 300°C to 800°C (572°F to 1472°F) thermomechanical test specimen. The large temperature range does not influence the physics of the microstructure as much as the magnitude of the upper temperature. This trend was consistent in all the thermomechanical tests, as the microstructures were shown to be dominated by features typically associated with the bounding "hot" isothermal tests. Therefore, this microstructure (Figures 4.24 and 4.25) is represented as typifying those found in the 600°C to 800°C (1112°F to 1472°F) thermomechanical test specimens. Here, signs of extensive thermal aging are present. Figure 4.24 reveals large cell structures containing a moderate intragranular dislocation density. The $M_{23}C_6$ phase is found at intragranular locations, however, the higher temperatures have caused the $M_{23}C_6$ carbides to dramatically increase in size (as seen under high temperature isothermal conditions). This increase in size (relative to the previous temperature range) is best illustrated by comparing Figures 4.25 and 4.23, while noting their respective magnification levels. This morphogenetic evolution is part of a process often referred to as microstructural "overaging", by authors reviewed in Chapter 2. Given this microstructure and the relatively high

A TYPICAL MICROSTRUCTURE TAKEN FROM A 300 C to 800 C THERMOMECHANICAL TEST SPECIMEN

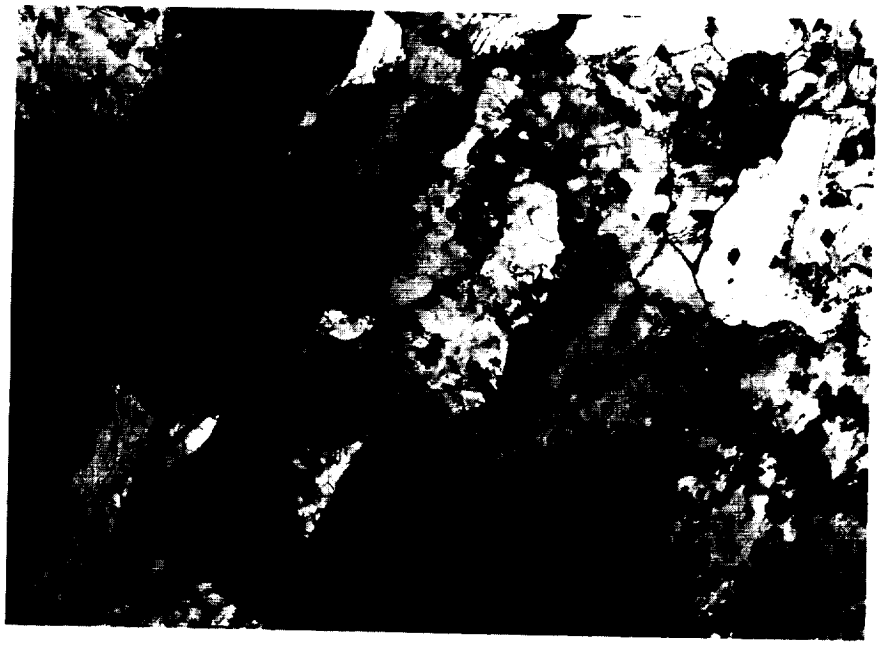

Magnification = 15 500 X

This thermomechanical microstructure exhibits features associated with isothermal tests performed at approximately 800 C

- Moderate intragranular dislocation density
- Large cell structures
- $M_{23}C_6$ phase is present at intragranular locations but now reveal a considerable increase in size
- This microstructure exhibits initial stages of thermal recovery and overaging effects

Figure 4.24 - 300 C to 800 C Thermomechanical Microstructure at 15 500 X

A TYPICAL MICROSTRUCTURE TAKEN FROM A 300 C to 800 C THERMOMECHANICAL TEST SPECIMEN

Magnification = 50 000 X

- $M_{23}C_6$ carbides displayed here are much larger than those found when tests are performed at or below the dynamic strain aging peak temperature
- This 300 C to 800 C microstructure is clearly shown to be dominated by the "hot" test temperature

Figure 4.25 - 300 C to 800 C Thermomechanical Microstructure at 50 000 X

A TYPICAL MICROSTRUCTURE TAKEN FROM A 300 C to 1000 C THERMOMECHANICAL TEST SPECIMEN

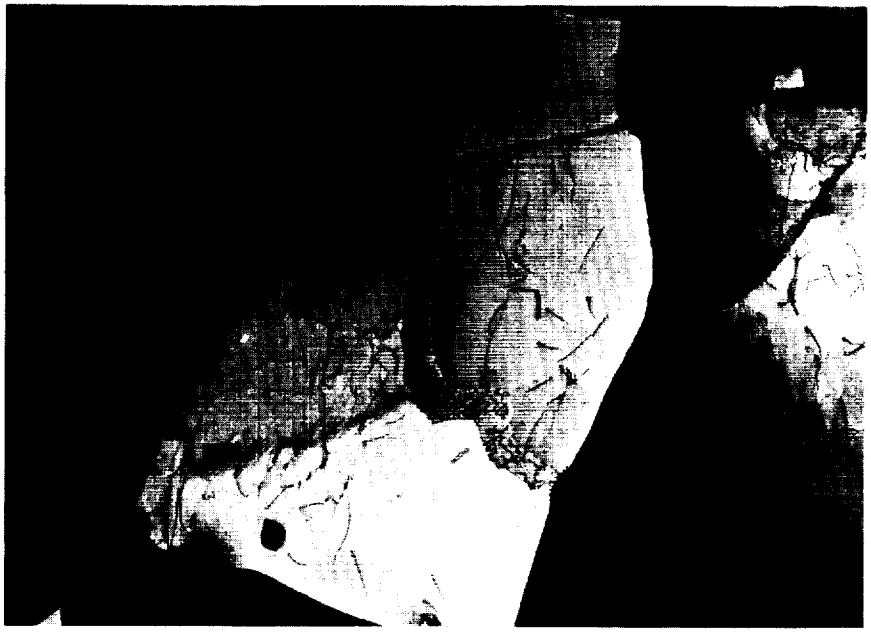

Magnification = 15 500 X

This thermomechanical microstructure exhibits features associated with isothermal tests performed at approximately 1000 C

- Low intragranular dislocation density
- Dislocations predominantly located at cell boundaries in well ordered arrangements
- Large cell and subcell structures
- Large $M_{23}C_6$ carbides are present

Figure 4.26 - 300 C to 1000 C Thermomechanical Microstructure at 15 500 X

A TYPICAL MICROSTRUCTURE TAKEN FROM A 300 C to 1000 C THERMOMECHANICAL TEST SPECIMEN

Magnification = 6 500 X

- This "low" magnification micrograph reveals several large cells
- Large $M_{23}C_6$ carbides have migrated and / or re-precipitated at cell and twin boundaries
- Extensive thermal recovery and overaging effects are clearly evident

Figure 4.27 - 300 C to 1000 C Thermomechanical Microstructure at 6 500 X

temperatures, it is not surprising that the specimen undergoes minimal hardening. It is important to reiterate, that even though the 300°C to 800°C (572°F to 1472°F) thermomechanical tests pass through the dynamic strain aging peak, the "hot" temperatures are able to "wash out" the previously efficient hardening mechanisms.

Shown in Figures 4.26 and 4.27 are micrographs taken from the out–of–phase 300°C to 1000°C (572°F to 1832°F) thermomechanical test. Arguments identical to those used for the 300°C to 800°C (572°F to 1472°F) test enable this microstructure to represent others which have experienced temperatures near 1000°C (1832°F) (i.e. microstructure is dominated by "hot" end). These micrographs reveal features similar to those found in the isothermal test performed at 871°C (1600°F), namely, effects of thermal recovery and overaging. Large cells and subcell structures are evident. Large $M_{23}C_6$ carbides are present, but have migrated and/or re–precipitated at cell boundaries. Intragranular regions are predominantly vacant of dislocations. Subjected to loading, this "empty" cell structure is typically associated with extensive intragranular deformation and plastic flow. The majority of dislocations present are found at cell and twin boundaries, in well ordered arrangements. This microstructure is consistent with phenomenological trends which exhibit little, if any hardening, and cyclic softening.

4.5 Additional Thermomechanical Data/Results

This investigation into the thermomechanical deformation of Hastelloy X has produced a wealth of unique data. Those results which were found to be pertinent to the objectives of this study have been included above. However, a significant amount of data produced in conjunction with this investigation was

not presented. Further, the results included above were intentionally presented in a manner which focuses on the thermomechanical hardening trends and dynamic strain aging effects. Little attention was given to individual deformation cycles. Individual hysteresis loops were collected at intermittent cycles, and analyzed on the basis of total, mechanical, elastic and inelastic strain. For example, Figures 4.28 and 4.29 reveal a series of hysteresis loops which have been reduced to display only the mechanical strains and inelastic strains, respectively. These loops display deformation experienced by the in–phase 400°C to 600°C (752°F to 1112°F) thermomechanical specimen. Upon viewing these plots, the extreme hardening is evidenced by the increasing stress amplitudes. Also, the inelastic strain is shown to decrease dramatically as the hardening progresses. Subtle features, such as the shift in inelastic mean strain shown in Figure 4.29, are important aspects of the material's response. Information of this type is most valuable when quantifying mathematical deformation models, such as that which is discussed in Chapter 5. Hence, data in this form will be published at a later date in an effort to describe, in greater detail, the deformation behavior of Hastelloy X.

4.6 Experimental Conclusions

The experimental conclusions formulated from this study have evolved from a detailed analysis of both isothermal and thermomechanical behavior. Both forms of phenomenological testing proved to exhibit extremely complex hardening trends. Further, several thermomechanical phenomenological trends were unique to the full spectrum of trends established under isothermal conditions. In order to understand these trends, and explain the

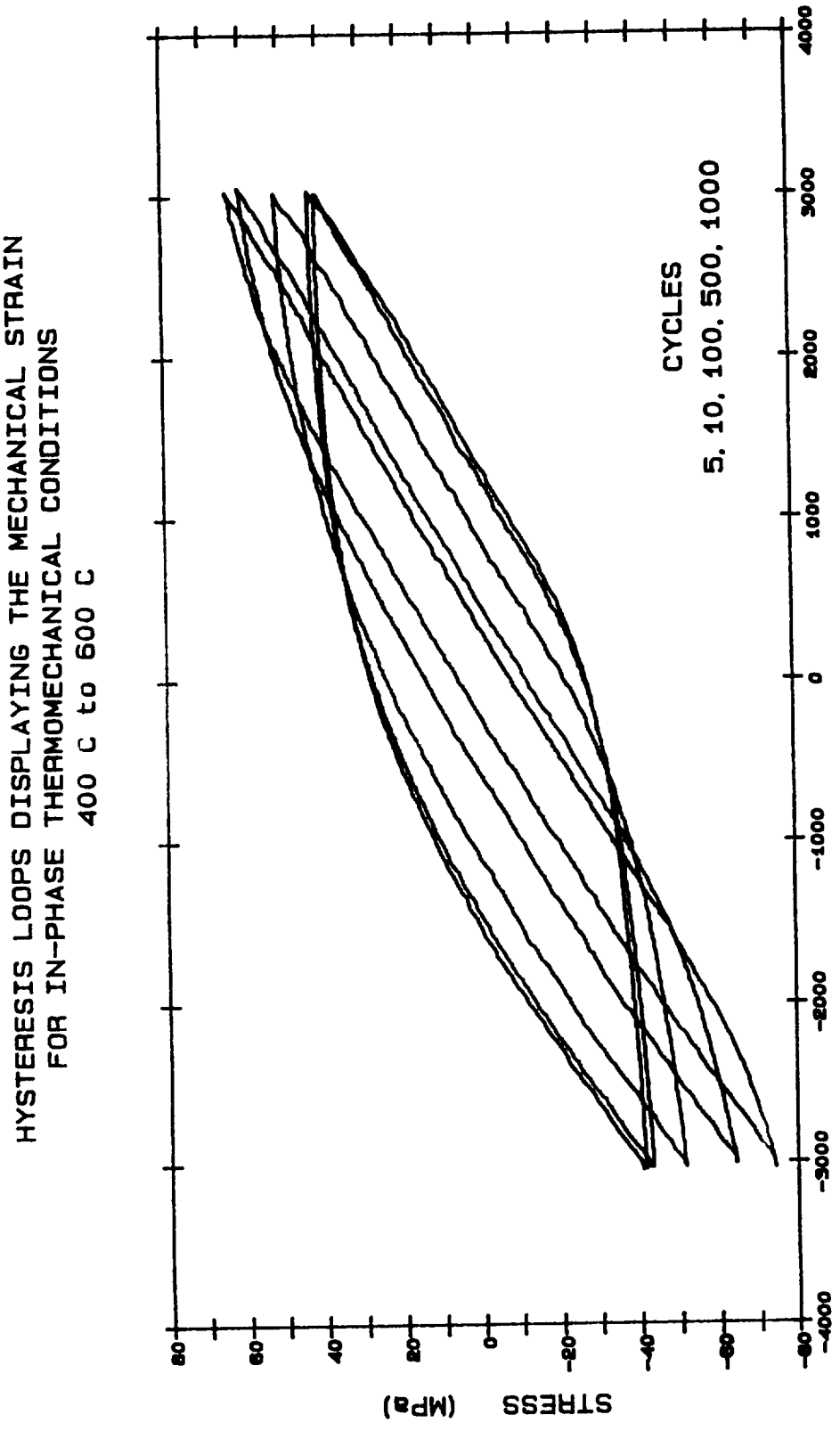

Figure 4.28 - Mechanical Strain Hysteresis Loops for In-Phase Thermomechanical Test: 400 C to 600 C

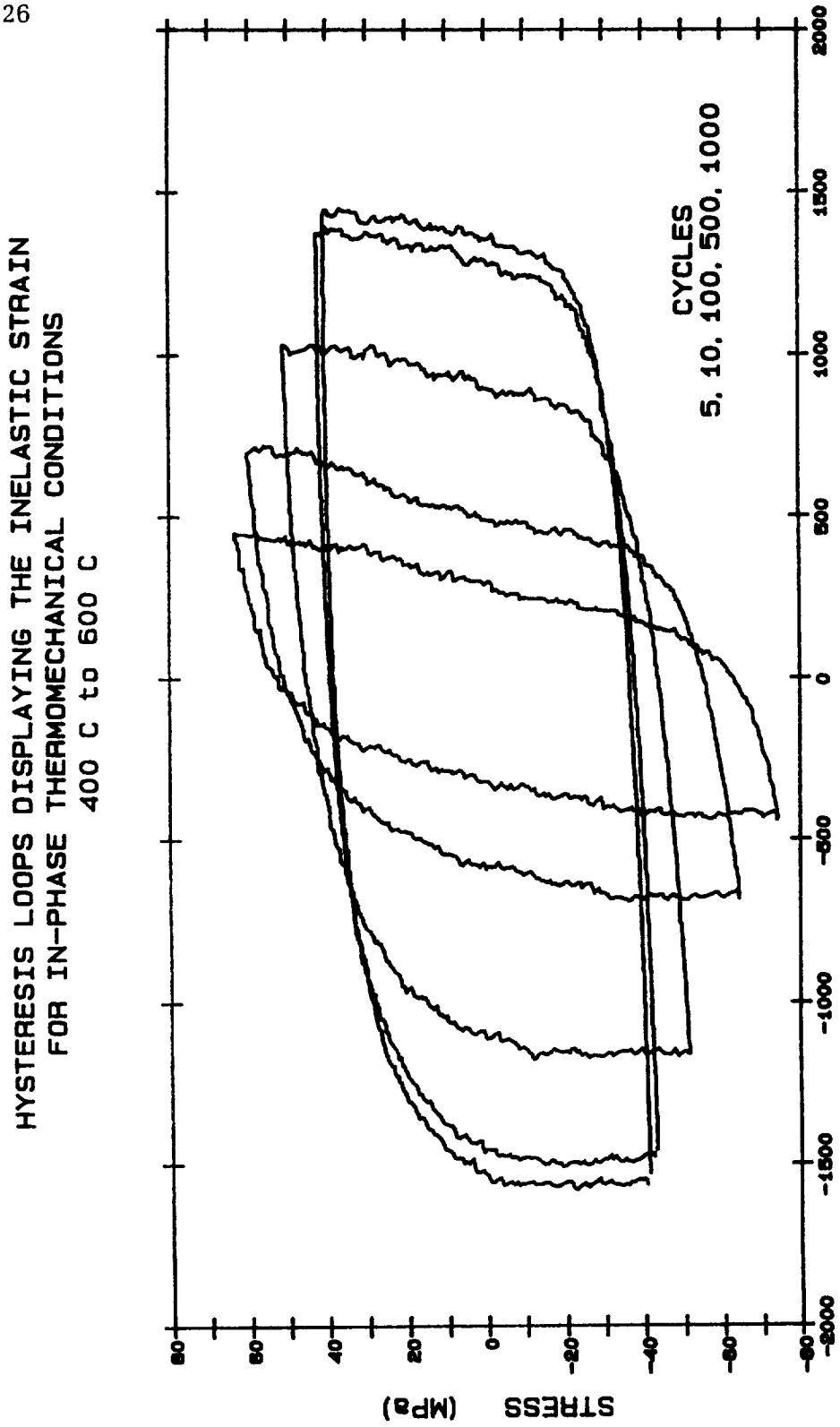

Figure 4.29 - Inelastic Strain Hysteresis Loops for In-Phase Thermomechanical Test: 400 C to 600 C

thermomechanical uniqueness, a detailed microstructural analysis was required. By linking the various aspects of this investigation, a clear, consistent description and explanation is formulated.

Complex isothermal hardening trends are found to be promoted by a well documented phenomenon called dynamic strain aging. In Hastelloy X, this phenomenon is promoted by metallurgical instabilities occurring in the form of a carbide phase precipitation. The intragranular precipitation of this phase ($M_{23}C_6$) results in efficient dislocation pinning, and thus material hardening. The isothermal dynamic strain aging peak is defined at approximately 600°C (1112°F). A $M_{23}C_6$ phase precipitation threshold temperature exists at approximately 500°C (932°F). At temperatures below this threshold ("pre–peak" temperatures), hardening is promoted by increasing dislocation densities (where dislocation density is shown to be greater with each increasing isothermal test temperature). At temperatures above the peak regime of 550°C to 650°C (1022°F to 1202°F), thermal recovery effects were shown to dominate the physics of the microstructure. This resulted in mild cyclic hardening at temperatures in the vicinity of 700°C to 800°C (1272°F to 1472°F) and eventually cyclic softening at isothermal temperatures above 800°C (1472°F).

Thermomechanical tests conducted entirely below the strain aging peak temperature, revealed unique hardening trends (with respect to the isothermal database). The unique behavior (extreme hardening) was found to be occurring at the "cold" end of the thermomechanical cycle. Here, hardening amplitudes were greater than those observed in either of the bounding isothermal tests. This phenomenological trend was explained by microstructural investigations. Microstructural physics were found to be dominated by effects associated with

the "hot" end of the cycle. For pre–peak temperatures, the "hot" end microstructure is that which has the greatest potential for hardening. Thus, by straining this "hot" microstructure under conditions of decreased thermal agitation (i.e. at "cold" temperatures), the material was able to harden beyond trends seen under isothermal conditions.

Thermomechanical tests involving temperatures above the strain aging peak temperature [i.e. $T \geq 650^{\circ}C$ ($1202^{\circ}F$)], were shown to exhibit mild cyclic hardening and eventually (as the maximum cycle temperature increased), cyclic softening. This trend was substantiated by microstructural examination where, again, the cycle's "hot" temperature was found to dominate the physical structure. Here thermal recovery effects and thermal overaging were evident. Microstructures exhibited intragranular vacancies, decreased dislocation densities, and large ineffective (with respect to hardening) carbides.

CHAPTER 5

THERMOVISCOPLASTIC MODELING IN THE PRESENCE OF METALLURGICAL INSTABILITIES

5.1 Introduction

5.1.1 General Comments

Constitutive modeling concerns mathematically representing a material's macroscopic behavior as dictated by stress, displacement and temperature. General mathematical frameworks for representing high temperature characteristic material response have evolved into what are referred to as unified viscoplastic theories. Here, "unified" implies that all aspects of inelastic behavior (creep, relaxation, plastic deformation) are represented as occurring interactively, and thereby accountable in a single flow law defining the"unified" inelastic strain rate. (Earlier theories separated the inelastic strain into time–independent and time–dependent components.)

Several unified constitutive theories have been proposed over the past ten years, including those by Miller [12], Chaboche [49], Robinson [2,3], Walker [11], Bodner et al [50] and Krieg et al [13]. The basic differences in these models can be broken down into three general areas. First, the theories display differences in their assumptions of directional hardening. For example, the inelastic strain rate may assume directional dependency from either the deviatoric stress, or an "effective" deviatoric stress. The latter allows past

deformation history to affect the directional hardening of the inelastic strain rate. Second, differences exist in the criteria used to define the onset of inelastic behavior (i.e. yield criterion). Several theories neglect a "completely elastic" regime, resulting in a non–zero inelastic strain rate for very small amounts of stress. In contrast, those theories which employ a yield criterion introduce a non–zero inelastic strain rate only beyond some prescribed threshold shear stress, hence, clearly defining a yield surface. The third major difference involves the assumption that the yield surface has the properties of a potential. A potential based mathematical framework for constitutive equations is one where the inelastic strain rate and evolution of state can be expressed in terms of the gradient of a potential (Ω) of stress, state and temperature [51]. It is this class of equations which is central to this investigation. In particular, a potential based model proposed by Robinson [2,3] is introduced, and extended to qualitatively predict the macroscopic effects of the metallurgical instabilities discussed in Chapter 4.

5.1.2 Robinson Model

The constitutive theory proposed by Robinson [2,3] features flow and evolutionary laws derivable from a dissipation potential function. This potential/normality structure has been shown [51,2] to assure desirable continuum properties such as uniqueness of solution, stability and convergence in structural problems. Early versions of this model were utilized in assessing the creep–plasticity characteristics of structural metals at high temperatures. In general, under high homologous temperature conditions ($T \geq 0.5\ T_m$ where T_m = melting temperature), a material will not experience isotropic work hardening.

Thus the internal scalar state variable associated with isotropic hardening history (i.e. "drag stress") is taken to be constant, or initially saturated. This typically enables the material behavior to be described with a single tensorial internal state variable accounting for kinematic hardening (i.e. "internal stress" or "back stress"). Therefore, isothermal and high temperature non–isothermal conditions were, and are well addressed with early versions of this model which feature a single evolving internal state variable.

In more recent work [19], the Robinson model was extended to qualitatively account for forms of thermomechanical path dependence. Here, thermomechanical path dependent behavior was observed in a series of simple step–wise non–isothermal tests [18]. The model was adapted by appropriately formulating an evolutionary equation for the scalar state variable which accounts for the isotropic hardening history. Specifically, a temperature rate term was included in the drag stress evolutionary equation which allowed for thermomechanical history dependence. This extension was shown to successfully predict the qualitative trends and thermomechanical path dependence observed in the cited tests.

The tests performed within this investigation involve a series of comprehensive "full" thermomechanical tests. Several unique thermomechanical trends were caused by the metallurgical instabilities and dynamic strain aging experienced by Hastelloy X. These macroscopic events and their phenomenological manifestations are described in Chapter 4. Robinson's model in its present form is not adequate to represent such trends.

Effort here is placed on extending the latest form of this model to qualitatively predict the phenomenological hardening trends displayed under full thermomechanical conditions.

The specific changes proposed here include the introduction of a third state variable and a corresponding evolutionary law. This additional state variable simulates the physical thermomechanical hardening trends associated with dynamic strain aging. In general, this new form enables the isotropic hardening rate to saturate earlier over certain thermomechanical paths. Also, with generic forms as proposed, the thermomechanical isotropic hardening and hardening rate can exceed the isothermal values. Thus, the maximum bounding isothermal stress ranges and amplitudes are able to be exceeded under certain thermomechanical conditions. The changes suggested here do not represent the only possible solution to predicting these unique thermomechanical trends. Different approaches to modeling thermomechanical behavior in the presence of metallurgical instabilities are found in [55] and [56]. However, the adaptation employed here was closely guided by microstructural observations and physics, and to the first order, reveals qualitatively accurate predictions of the thermomechanical response of Hastelloy X.

5.2 Mathematical Framework of Robinson Model

The general mathematical framework employed in the Robinson model has evolved from a class of constitutive equations derived from gradients of a dissipation potential function Ω.

$$\Omega\,(\sigma_{ij},h_{\alpha},T) \quad \alpha = 1,2,.....n \tag{5.1}$$

$$\dot{\epsilon}_{ij} = \frac{\partial\Omega}{\partial\sigma_{ij}} \tag{5.2}$$

$$\dot{h}_{\alpha} = -H_{\alpha}(h_{\alpha},T)\,\frac{\partial\Omega}{\partial h_{\alpha}} \quad \text{(no sum on } \alpha) \tag{5.3}$$

Here σ_{ij} is the Cauchy stress, $\dot{\epsilon}_{ij}$ is the inelastic strain rate, $h_{\alpha} = h_1,h_2,...$ are internal state variables which record the deformation history, H_{α} are functions of the internal state variables h_{α}, and T is the temperature. Equations (5.2) and (5.3) are referred to as the flow law and evolutionary law(s) respectively.

Models developed from this potential/normality structure have been shown [52] to be consistent with a simple thermodynamic formalism. This framework has been used [2,3,53,54] as a starting point for various viscoplastic models of isotropic and anisotropic metals.

A further specialization of this basic framework is one which allows for both isotropic and kinematic hardening. The general mathematical structure of such a theory is shown below.

$$\Omega = \Omega\,(\sigma_{ij},\alpha_{ij},\kappa,T) \tag{5.4}$$

$$\dot{\epsilon}_{ij} = \frac{\partial\Omega}{\partial\sigma_{ij}} \tag{5.5}$$

$$\dot{\alpha}_{ij} = -h(\alpha_{kl},T)\,\frac{\partial\Omega}{\partial\alpha_{ij}} \tag{5.6}$$

$$\dot{\kappa} = -H(\kappa,T)\,\frac{\partial\Omega}{\partial\kappa} + \Theta(T)\,\dot{T} \tag{5.7}$$

Here, the hereditary nature of the material is recorded through the use of two internal state variables α_{ij} and κ. Equation (5.6) is the evolutionary law for the internal stress α_{ij}. This second order symmetric tensor α_{ij} is a measure of the

material's kinematic hardening, and physically represents an average opposing macrostress with origins in the material's dislocation microstructure. Equation (5.7) is the evolutionary law for the drag or threshold stress κ. This scalar variable κ is associated with isotropic hardening, and physically represents a measure of the microstructural dislocation density. This extension of the potential framework accounts for spontaneous changes in the isotropic state variable κ with changes in temperature, hence, a spontaneous change in the yield surface associated with a change in temperature. This feature (i.e. the inclusion of the $\dot{T}$ term) is necessary to represent the thermomechanical path dependence observed in [18,19]. Also, this form is consistent with the formal thermomechanical development found in [52].

For initially isotropic materials, Ω can be taken [2,53,54] to depend upon the principal invariants of deviatoric stress quantities through scalar functions F and G.

$$\Omega = \Omega(F,G,T) = \theta_f(T) \int f(F)dF + \theta_g(T) \int g(G)\, dG \tag{5.8}$$

where $$F = \frac{J_2}{\kappa^2} - 1 \qquad J_2 = \frac{1}{2}\,\Sigma_{ij}\,\Sigma_{ij} \qquad \Sigma_{ij} = s_{ij} - a_{ij} \tag{5.9}$$

$$G = \frac{J_2}{\kappa_0^2} \qquad J_2 = \frac{1}{2}\,a_{ij}\,a_{ij} \tag{5.10}$$

$$\dot{\epsilon}_{ij} = \frac{\theta_f(T)}{\kappa^2}\, f(F)\, \Sigma_{ij} \tag{5.11}$$

$$\dot{a}_{ij} = h(G)\, \dot{\epsilon}_{ij} - \theta_g(T)\, r(G)\, a_{ij} \tag{5.12}$$

where $$r(G) = h(G)\, g(G)$$

$$\dot{\kappa} = \Gamma(\kappa,T)\dot{W} + \circledast(T)\, \dot{T} \tag{5.13}$$

where $$\dot{W} = \Sigma_{ij}\, \dot{\epsilon}_{ij}$$

Here, θ_f and θ_g are usually taken as Arrhenius type functions. As the main interest here is cyclic (isotropic) hardening, emphasis is placed on the evolution equation for the isotropic hardening variable κ (equation 5.13).The form presented above allows for the thermomechanical path dependence identified in [19] with contributions to the evolution of κ from effective inelastic work (W) and temperature (T).

In [19], the function $\circledast(T)$ was taken as an Arrhenius form

$$\circledast(T) = \frac{-Q_0}{T} e^{-Q_0[T_*^{-1} - T^{-1}]} \tag{5.14}$$

where T_* represents a reference temperature, and Q_0 represents an "activation energy". The function $\Gamma(\kappa,T)$ was taken as

$$\Gamma(\kappa,T) = \Gamma_0(T)p(Z) \ldots\ldots p(0) = 0 \tag{5.15}$$

$$\text{where} \qquad Z(\kappa,T) = \frac{\kappa_s(T) - \kappa}{\kappa_s(T) - \kappa_0(T)} \tag{5.16}$$

The function $\kappa_0(T)$ is the initial value of the state variable κ (before mechanical cycling) and taken as

$$\kappa_0(T) = \kappa^* - [1 - e^{-Q_0(T_*^{-1} - T^{-1})}] \tag{5.17}$$

$$\text{where} \qquad \kappa^* = \kappa_0(T_*)$$

$\kappa_s(T)$ is the saturated value of κ after extended cycling and $\Gamma_0(T)$ is a measure of the rate of hardening. Possible forms of the function p(Z) are

$$p(Z) = A\, Z^{n} \tag{5.18}$$

and

$$p(Z) = A\,[1 - e^{(-Z)}] \tag{5.19}$$

By selecting appropriate forms for $\kappa_s(T)$ and $\Gamma_o(T)$ (such as those shown in Figure 5.1 and 5.2, respectively),the isothermal hardening behavior associated with dynamic strain aging is represented. Specifically, the maximum hardening (κ or $\Delta\sigma$) and hardening rate ($\frac{d\,\kappa}{dW}$ or $\frac{d(\Delta\sigma)}{dN}$) are experienced at some intermediate "peak" temperature T_p.

5.3 Proposed Extension

The constitutive formulation discussed above was shown to be capable of qualitatively predicting several key features exhibited by Hastelloy X. These include, appropriate isothermal dynamic strain aging trends, and forms of thermomechanical path dependence exhibiting spontaneous shifts in the yield surface. It is the case however, that this functional form is not adequate to represent the unique thermomechanical trends exhibited and discussed in chapter 4. Specifically, metallurgical instabilities experienced by Hastelloy X are promoted by temperatures in the strain aging peak vicinity. Upon experiencing such temperatures in the presence of mechanical straining, high immobile dislocation densities are established in the microstructure. This has been shown to result primarily from the $M_{23}C_6$ carbides, and their ability to pin dislocations. Once having created this "strong" microstructure, subsequent decreases in temperature result in hardening rates and magnitudes greater than those experienced under any isothermal conditions. It is this specific feature which is in need of representation.

APPROPRIATE FORMS OF $\kappa_s(T)$ AND $\Gamma_o(T)$ WHICH REPRESENT THE ISOTHERMAL HARDENING BEHAVIOR ASSOCIATED WITH DYNAMIC STRAIN AGING

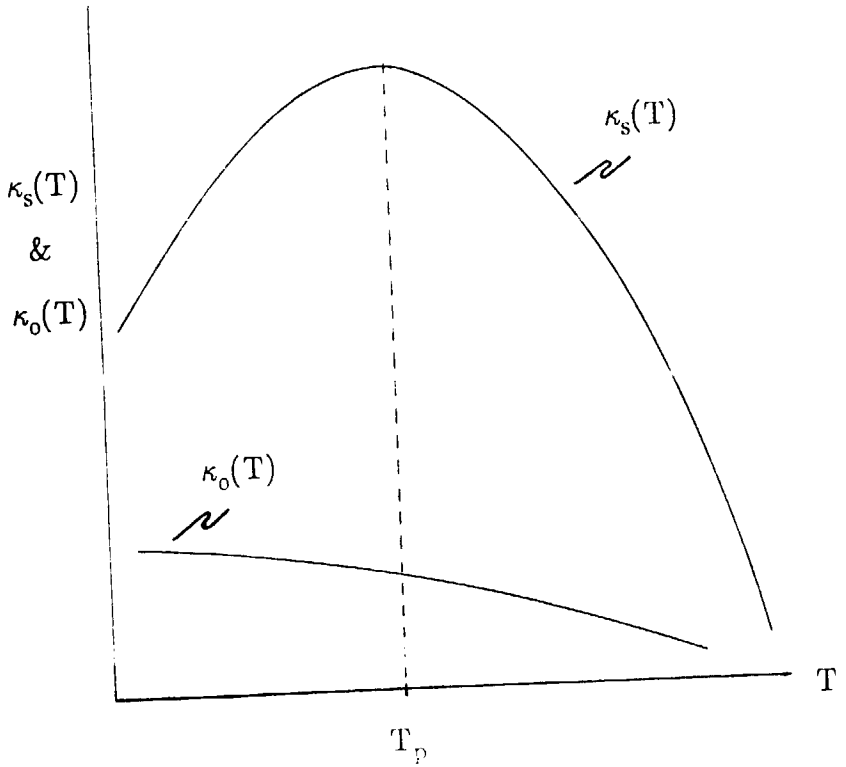

Figure 5.1 – Initial and Saturation Forms of $\kappa(T)$

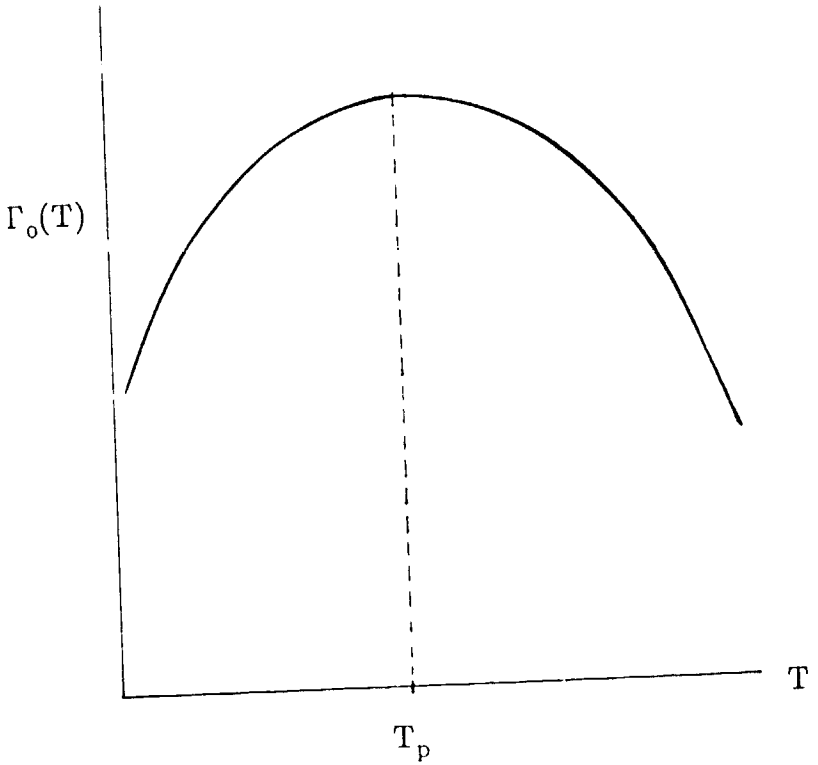

Figure 5.2 – Form of $\Gamma_o(T)$

In an effort to represent the thermomechanical features observed in this study, an additional state variable β is introduced. The evolutionary law proposed is as follows:

$$\dot{\beta} = \Psi(T)\,\dot{W} - \phi(T) \tag{5.20}$$

where $$\Psi(T) = A\, e^{\left[\frac{-(T-T_p)^2}{\rho}\right]} \tag{5.21}$$

and $$\phi(T) = B\, e^{[Q_r(T_r^{-1}-T^{-1})]} \tag{5.22}$$

where T_p represents the dynamic strain aging peak temperature, Q_r and T_r are an activation energy and reference temperature for recovery effects, respectively, and A, B and ρ are material constants. The functions $\Psi(T)$ and $\phi(T)$ are plotted in Figure 5.3. $\Psi(T)$ is non–zero only near the peak aging temperature T_p. Thus, the first term in Equation (5.20) is also non–zero only when the temperature is in the vicinity of T_p. Further, the first term contributes to $\dot{\beta}$ only if effective inelastic work is being incurred ($\dot{W} \neq 0$). This structure is consistent with the "dynamic" nature of the strain aging phenomenon.This framework accounts for the macroscopic hardening effects caused by the presence of the $M_{23}C_6$ carbide phase, where time spent in the vicinity of the peak temperature accompanied by inelastic work enable this phase to precipitate.

The function $\phi(T)$ is an Arrhenius form that accounts for thermal recovery of β when the temperature exceeds the peak temperature T_p and mechanisms such as dislocation climb become significant. Time at temperature above T_p leads to $\dot{\beta} < 0$ in Equation (5.20) and allows for partial or complete erasure of hardening ($\beta > 0$) that may have occurred by exposure to cycling at

APPROPRIATE FORMS OF $\Psi(T)$ AND $\phi(T)$ WHICH REPRESENT THE UNIQUE THERMOMECHANICAL FEATURES ASSOCIATED WITH DYNAMIC STRAIN AGING

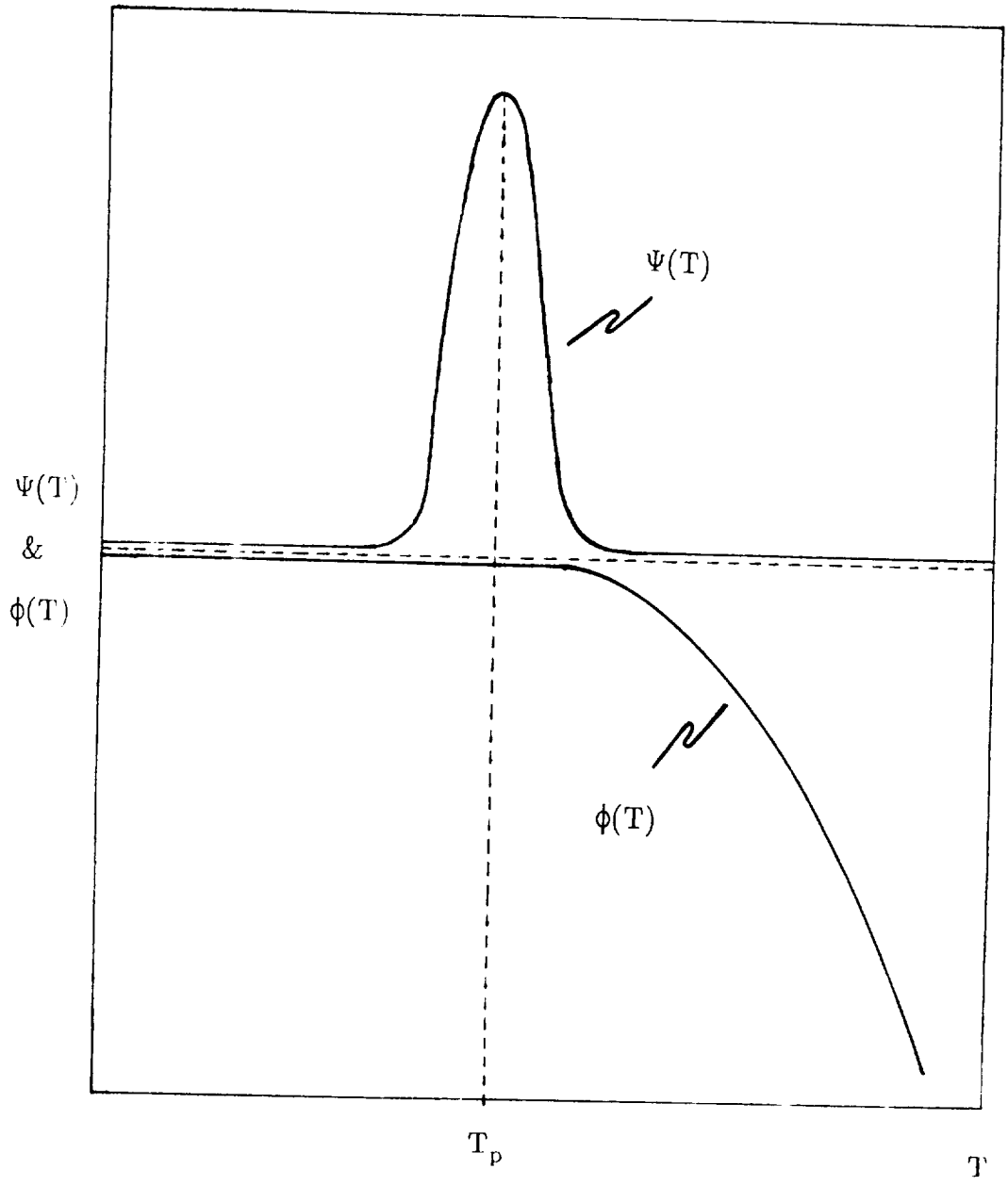

FIGURE 5.3 – Appropriate Forms of $\Psi(T)$ and $\phi(T)$

temperatures near T_p. This mathematical framework is able to simulate the observed thermal recovery and overaging effects exhibited in the microstructure of Hastelloy X, where the $M_{23}C_6$ carbides are seen to coalesce, enlarge and migrate to grain boundaries, thus "erasing" their hardening potential.

The function Γ in the evolution law for κ (see Equations 5.13, 5.15 and 5.16) is taken to include dependence on β through the functions $\kappa_s(<\beta>,T)$ and $\Gamma_o(<\beta>,T)$.

$$<\beta> = \begin{cases} \beta \; ; \; \beta > 0 \\ 0 \; ; \; \beta \leq 0 \end{cases}$$

This dependence is proposed as illustrated in Figures 5.4 and 5.5. With $\beta = 0$, κ_s and Γ_o will maintain their respective forms illustrated in Figures 5.1 and 5.2. As β increases according to its evolution equation, κ_s and Γ_o evolve as shown in Figures 5.4 and 5.5.

As an example of thermomechanical response, assume the dynamic strain aging peak temperature (T_p) occurs at approximately 600°C (1112°F). Under thermomechanical cycling over a temperature range say, from 400°C to 600°C (752°F to 1112°F), the upper temperature falls precisely on T_p, the ensuing growth of β with both time and cycling allows for enhanced hardening and hardening rate at lower temperatures [i.e. 400°C (752°F)], where under isothermal cycling the hardening is minimal. Hence, this proposed form is able to qualitatively predict the unique thermomechanical trends observed in Chapter 4.

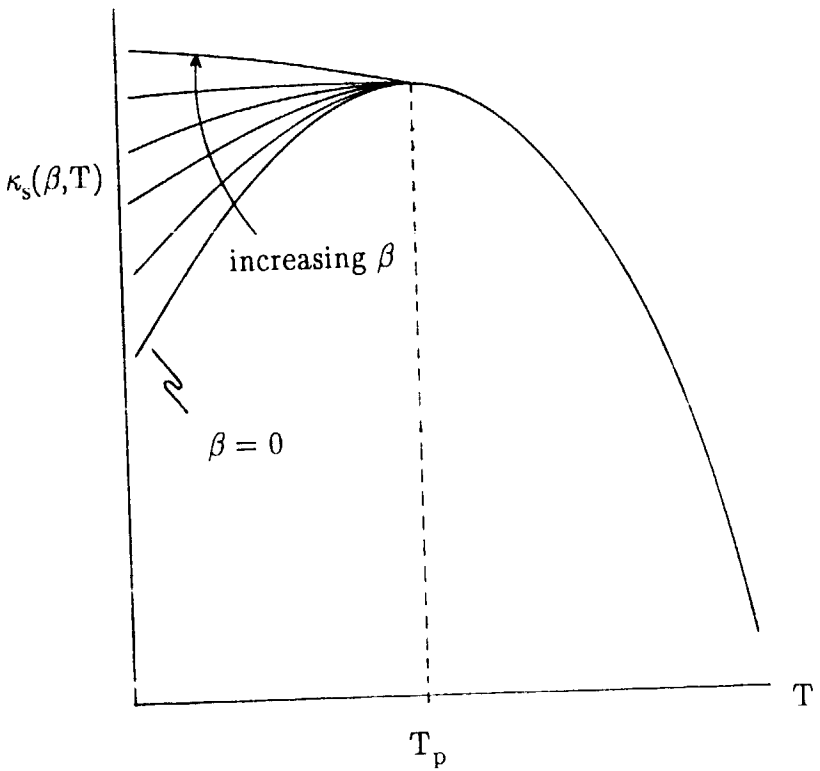

Figure 5.4 – Evolution of $\kappa_s(\beta,T)$

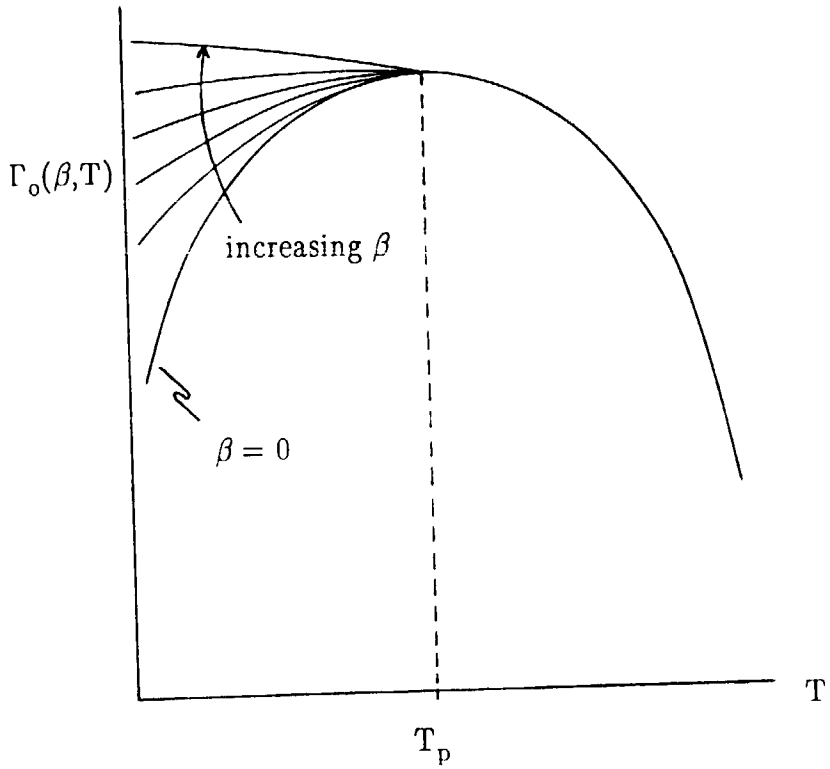

Figure 5.5 – Evolution of $\Gamma_o(\beta,T)$

As a second example, assume the same T_p and a cyclic temperature range from 300°C to 800°C (572°F to 1472°F). $\phi(T)$ will act as a competing mechanism against $\Psi(T)$, forcing β to be negative at temperatures above T_p. This, in effect, erasing the hardening incurred at temperatures in the vicinity of 600°C (1112°F). The resulting magnitude of β will approach zero, and the resulting thermomechanical hardening will be dominated by effects associated with the "hot" cycle temperature.

The proposed form of β is capable of qualitatively predicting the unique thermomechanical hardening trends observed in Chapter 4. Further, this mathematical structure allows the thermomechanical hardening to be dominated by effects associated with the "hot" end of the cycle. With this extension, the Robinson model is able to represent the thermomechanical hardening trends experienced by Hastelloy X, as influenced by metallurgical instabilities.

CHAPTER 6
SUMMARY AND CONCLUSIONS

6.1 Summary

The work presented in this study was conducted to investigate several primary concerns. First, Hastelloy X was shown to display complex phenomenological hardening trends under isothermal conditions. These features were chiefly promoted by a form of metallurgical instability which results in dynamic strain aging. One primary concern was the influence of such instabilities under full thermomechanical conditions, which most accurately describes the environment experienced by structural components in service.

In order to accurately investigate the thermomechanical response of Hastelloy X, it was first necessary to further develop existing thermomechanical testing technology. Chapter 3 describes this development. The culmination of this effort is represented by a mature set of experimental testing procedures and techniques (presented in Section 3.7.4) whose proper use allow closely controlled thermomechanical tests to be performed in a uniaxial, strain–controlled environment.

Upon completing these tests, the isothermal and thermomechanical behaviors were compared and analyzed from both phenomenological and microstructural viewpoints. These comparisons address the second primary concern of this investigation, namely, the following question required an

answered. "Is isothermal testing sufficient for describing a material's full behavioral spectrum ?" With respect to Hastelloy X (and other strain aging materials), the answer to this question is, no. The phenomenological thermomechanical response exhibited trends which were not present under isothermal conditions. These unique trends were found to be well explained by linking the microstructural observations with the specific thermomechanical test conditions (i.e. temperature range). This approach was successfully utilized (in Chapter 4) to clarify and substantiate the observed trends for each of the thermomechanical paths.

After establishing the existence of a unique thermomechanical response, the final concern addressed in this study evolved around the ability to predict such behavior. This ability was gained by properly extending an existing thermoviscoplastic constitutive theory. This adaptation was strongly guided by the observed microstructural physics, as well as the phenomenological trends. The resulting mathematical framework (discussed in Chapter 5) was shown to capable of qualitatively predicting the unique thermomechanical hardening behavior exhibited by Hastelloy X.

6.2 Conclusions

Presented here are the major conclusions pertaining to the material behavior of Hastelloy X. These conclusions are based on the experimental work discussed in Chapter 4.

1) Isothermal hardening trends were found to exhibit a dynamic strain aging peak at temperatures in the vicinity of 600°C (1112°F).

2) In general, isothermal tests performed at temperatures within the "low" temperature regime experienced mild–to–moderate cyclic hardening. This was found to be consistent with the microstructures, where, relatively low dislocation densities were found without the presence of the $M_{23}C_6$ carbide phase.

3) Isothermal tests performed in the "middle" or "peak" temperature regime experienced extreme cyclic hardening. This was found to be consistent with the microstructures, where, the $M_{23}C_6$ phase was found generously dispersed at intragranular locations amid a high dislocation density.

4) Isothermal tests performed in the "high" temperature regime revealed mild hardening, and eventually, with increasing temperature, cyclic softening. Here, the microstructure displayed large cell and subcell structures, predominantly vacant intragranular regions, and morphologically enlarged $M_{23}C_6$ carbides. These features are typical of overaging and thermal recovery type effects.

5) Thermomechanical tests involving temperatures which at some point during the cycle exceed the strain aging peak temperature [i.e. $T \geq \approx 650^{\circ}C$ ($\approx 1200^{\circ}F$)], revealed mild hardening or possibly cyclic softening. Microstructures displayed here are consistent with those described for the "high" isothermal temperature regime.

6) Thermomechanical tests performed in the temperature range from $200^{\circ}C$ to $400^{\circ}C$ ($392^{\circ}F$ to $752^{\circ}F$) were found to harden outside the bounding isothermal cyclic stress range. Amplitude plots revealed that "unbounded" cyclic hardening was occurring at the "cold" end of the thermomechanical cycle. Microstructures revealed high dislocation densities, typically associated with isothermal tests performed at temperatures at or above $400^{\circ}C$ ($752^{\circ}F$). The

$M_{23}C_6$ phase was not present. The combination of the "strong" microstructure and a decreased amount of thermal agitation, enabled the thermomechanical condition to promote hardening in excess of that experienced by the bounding isothermal tests.

7) The thermomechanical tests performed in the temperature range of 400°C to 600°C (754°F to 1112°F) revealed excessive hardening which significantly exceeded that displayed under any isothermal condition. Amplitude plots clearly revealed that the excessive hardening was occurring at the "cold" end of the cycle. The microstructure was found to be similar to those displayed from isothermal tests conducted in the "middle" or "peak" temperature regime. Hardening in this temperature regime is much more severe as a result of the presence of the $M_{23}C_6$ phase (whose precipitation is promoted by metallurgical instabilities). The combination of the "strong" microstructure and a decreased amount of thermal agitation, enabled the thermomechanical condition to promote hardening in excess of that experienced by the bounding isothermal tests. Further, in this case, as a result of the "hot" cyclic temperature occurring in the vicinity of the "peak" temperature, the thermomechanical cyclic hardening surpasses the maximum trend predicted by the isothermal database.

The following conclusions apply to all the thermomechanical tests conducted in this study.

8) The phenomenological hardening rate was governed by the "hot" temperature of the cycle.

9) The microstructural physics were found to be governed by the "hot" temperature of the cycle.

REFERENCES

1. Baird, J. D., "Dynamic Strain Aging," In: *The Inhomogeneity of Plastic Deformation*, ASM, Metals Park, Ohio, 1973.

2. Robinson, D. N., "A Unified Creep–Plasticity Model for Structural Metals at High Temperatures," Oak Ridge National Laboratory, Report No. ORNL/TM–5969, Nov., 1978.

3. Robinson, D. N., and Swindeman, R. W., "Unified Creep–Plasticity Constitutive Equations for Structural Alloys at Elevated Temperatures," Oak Ridge National Laboratory, Report No. ORNL/TM–8444, Oct., 1982.

4. Glasier, L. F., Jr., "Hastelloy X Properties, Data, and Metallurgical Characteristics," Atomic Energy Commission/NASA Tech Brief 68–10023, Feb., 1968.

5. Carden, A. E., Harman D. G., and Franco–Ferreira, E. A., "Thermal Fatigue Analysis of a Cryogenically Cooled Rocket Nozzle," Paper No. 102, American Astronautical Society, Southeastern Symposium, Huntsville, AL., Dec., 1966.

6. Carden, A. E., and Slade, T. B., "High–temperature Low–cycle Fatigue Experiments on Hastelloy X, In:*Fatigue at High Temperature*, ASTM Special Technical Publication 459, 1969, pp. 111–129.

7. McClintock, F. A., and Argon, A. S., *Mechanical Behavior of Materials*, Addison Wesley, Reading, MA., 1966.

8. Jaske, C. E., Rice, R. C., Buchheit, R. D., Roach, D. B., and Porfilio, T. L., "Low–Cycle Fatigue of Type 347 Stainless Steel and Hastelloy Alloy X in Hydrogen Gas and in Air at Elevated Temperatures," NASA LeRC Contract Report No. CR–135022, Jan., 1976.

9. Seaver, D. W., "Low Cycle Fatigue Properties of Hastelloy X at 704°C / 1300°F/," In:*Methods for Predicting Material Life in Fatigue*; ASME Proceedings of the Winter Annual Meeting, New York, N.Y., Dec. 2–7, 1979, pp. 133–144.

10. Walker, K. P., "Research and Development Program for Nonlinear Structural Modeling with Advanced Time–Dependent Constitutive Relationships: Final Report," NASA LeRC Contract Report No. CR–165533, Nov., 1981.

11. Walker, K. P., "Representation of Hastelloy X Behavior at Elevated Temperature with a Functional Theory of Viscoplasticity," ASME Journal of Engineering Materials and Technology, 1981

12. Miller, A. K., "An Inelastic Constitutive Model for Monotonic, Cyclic and Creep Deformation: Part I – Equations Development and Analytical Procedures, Part II – Application to Type 304 Stainless Steel," ASME Journal of Engineering Materials and Technology, Vol 98, 1976, pp. 97–113.

13. Krieg, R. D., Swearengen, J. C., and Rohde, R. W., "A Physically Based Internal Variable Model for Rate–Dependent Plasticity," In: *Inelastic Behavior of Pressure Vessel and Piping Components*, ASME PVP–PB–028, 1978, pp. 15–28.

14. McKoy, H. E., and King, J. F., "Evaluation of Hastelloy X for Gas–Cooled Reactor Applications," Oak Ridge National Laboratory, Report No. ORNL/TM–8499, Nov., 1982.

15. Jordan, E. H., "Elevated Temperature Biaxial Fatigue," NASA LeRC Contractor Report No. 175009, Oct., 1985.

16. Brinkman, C. R., "High Temperature Time Dependent Fatigue Behaviour of Several Engineering Structural Alloys," International Metals Reviews, Vol 30, No. 5, 1985, pp. 235–258.

17. McKoy, H. E., "Mechanical Properties of Hastelloy X and Inconel 617 After Aging 53,000 Hours in HTGR–He," Oak Ridge National Laboratory, Report No. ORNL/TM–9604, SEP., 1985.

18. Bartolotta, P. A., "Thermomechanical Cyclic Hardening Behavior of Hastelloy X," NASA LeRC Contractor Report No. 174999, Nov., 1985.

19. Robinson, D. N., and Bartolotta, P. A., "Viscoplastic Constitutive Relationships with Dependence on Thermomechanical History," NASA LeRC Contractor Report No. 174836, Mar., 1985.

20. Kotval, P. S., and Hatwell, H., "Discontinuous Precipitation of $M_{23}C_6$ Carbide in a Nickel–Base Superalloy," Transactions of the Metallurgical Society of AIME, Vol. 245, Aug., 1969, pp. 1821–1823.

21. Lewis, M. H., and Hattersley, Acta. Met., Vol 13, 1965, p. 1159.

22. Tu, K. N., and Turnbull, D., Acta. Met., Vol 15, 1967, p. 369.

23. Singhal, L. K., and Martin, J. W., Transactions of the Metallurgical Society of AIME, Vol. 242, 1968, p. 814.

24. Arkoosh, M. A., and Fiore, N. F., "Elevated Temperature Ductility Minimum in Hastelloy Alloy X," Metallurgical Transactions, Vol. 3, Aug., 1972, pp. 2235–2240.

25. Rhines, F. N., and Wray, P. J., Transactions of ASM, Vol 54, 1961, pp. 117–128.

26. Shapiro, E., and Dieter, G. E., Metallurgical Transactions, Vol 2, 1971, pp. 1358–1391.

27. Shapiro, E., and Dieter, G. E., Metallurgical Transactions, Vol. 1, 1970, pp. 1711–1719.

28. Kotval, P. S., Transactions of the Metallurgical Society of AIME, Vol. 242, 1968, pp. 1651–1656.

29. Waggoner, E. L., Report No. 816–41101–1, Haynes Stellite Co., Kokomo, IN., Jun., 1961.

30. Lai, G. Y., "An Investigation of the Thermal Stability of a Commercial Ni–Cr–Fe–Mo Alloy (Hastelloy Alloy X)," Metallurgical Transactions from The American Society for Metals and The Metallurgical Society of AIME, Vol. 9A, Jun., 1978, pp. 827–833.

31. Tawancy, H. M., "Long–term Aging Characteristics of Hastelloy X," Journal of Materials Science, Vol. 18, Oct., 1983, pp. 2976–2986.

32. Kotval, P. S., Metallography Journal, Vol 1, 1969, p. 251.

33. Wallwork, G., and Croll, J., In: *Review of High Temperature Materials*, Freund Publishing House, Ltd., Israel, 1976, p. 89.

34 Hall, E. O., and Algie, S. H., Metallurgical Review, Vol 11, 1966, p. 61.

35. Miner, R. V., Allen, G. P., Bartolotta, P. A., Mladsi, S. W., and Ellis, J. R., "Investigation of Cyclic Hardening Mechanisms in Hastelloy X," Proc. from Fourth TMF Workshop, NASA LeRC, Sep. 1987.

36. Ellis, J. R., Bartolotta, P. A., Allen, G. P., and Robinson, D. N., "Thermomechanical Characterization of Hastelloy X Under Uniaxial Cyclic Loading," Turbine Engine Hot Section Technology, NASA LeRC Report No. CP–2444, Oct., 1986, pp. 293–305.

37. Coffin, L. F., Jr., "The Stability of Metals Under Cyclic Plastic Strain," Transactions of the ASME, Journal of Basic Engineering, Vol. 82D, Sep., 1960, pp. 671–682.

38. Li, P., Marchand, N. J., and Ilschner, B., "Inhomogeneous Cyclic Deformation Behavior of Polycrystalline Aluminum," In: *Low–Cycle Fatigue and Elasto–Plastic Behaviour of Materials*, Elsevier Applied Science, London and New York, 1988, pp. 55–64.

39. Conway, J. B., Stentz, R. H., and Berling, J. T., "High Temperature, Low–Cycle Fatigue of Copper–Base Allows in Argon; Part II – Zirconium–Copper at 482, 538 and 593°C," NASA LeRC Contractor Report No. CR–121260, AUG., 1973.

40. Sheffler, K. D., and Doble, G. S., "Influence of Creep Damage on the Low–Cycle Thermal–Mechanical Fatigue Behavior of Two Tantalum Base Alloys," NASA LeRC Final Contractor Report No. CR–121001, May, 1972.

41. Avery, L. R., Carayanis, G. S., and Michky, G. L., "Thermal–Fatigue Tests of Restrained Combustor–Cooling Tubes," Experimental Mechanics, Vol. 7, No. 6, Jun., 1967, pp. 256–264.

42. Bartolotta, P. A., and McGaw, M. A., "A High Temperature Fatigue and Structures Testing Facility," NASA LeRC Report No. TM–100151, Aug., 1987.

43. Ellis, J. R., Bartolotta, P. A., and Mladsi, S. W., "Preliminary Study of Creep Thresholds and Thermomechanical Response in Haynes 188 at Temperatures in the Range 649 to 871°C," Turbine Engine Hot Section Technology, Conf. Publication, 1987, pp. 313–334.

44. Ellis, J. R., and Bartolotta, P. A., "A Fixture Facilitating the Use of Induction Heating in Mechanical Testing," NASA LeRC Report No. TM–102416, Jun., 1990.

45. Robinson, D. N., and Swindeman, R. W., "Additions and Modifications to Constitutive Equations in NE Standard F9–5T," High Temperature Structural Design Program Prog. Rep., Report No. ORNL–5794, Jun., 1981.

46. Robinson, D. N., and Swindeman, R. W., "Modifications to Constitutive Equations in NE Standard F9–5T," High Temperature Structural Design Program Prog. Rep., Report No. ORNL–5863, Dec., 1981.

47. Robinson, D. N., "Thermomechanical Deformation in the Presence of Metallurgical Changes," Proc. from Second Symposium on Nonlinear Constitutive Relations for High Temperature Applications, NASA LeRC, Report No. CP–2271, Jun., 1984.

48. Robinson, D. N., and Ellis, J. R., "High Temperature Constitutive Modeling," Turbine Engine Hot Section Technology, NASA Conf. Pub. 2239, Oct., 1984.

49. Chaboche, J. L., "Viscoplastic Constitutive Equations for the Description of Cyclic and Anisotropic Behavior of Metals," Bulletin De L'Academie Polonaise des Sciences, Vol XXV, No. 1, 1977, pp. 33–42.

50. Bodner, S. R., and Partom, Y., "Constitutive Equations for Elastic – Viscoplastic Strain – Hardening Materials," Journal of Applied Mechanics, Vol. 42, 1975, pp. 385–389.

51. Ponter, A. R. S., "Convexity and Associated Continuum Properties of a Class of Constitutive Relationships," Journal de Mecanique, Vol. 15, No. 4, 1976, pp. 527–542.

52. Ponter, A. R. S., "General Theorems for the Dynamic Loading of Structures for a State Variable Description of Material Behavior," Inst. Phys. Conf. Ser. No. 47, 1979, pp. 130–141.

53. Robinson, D. N., "Constitutive Relationships for Anisotropic High Temperature Alloys," Nuclear Engineering and Design, Vol. 83, 1984.

54. Robinson, D. N., Duffy, S. F., and Ellis, J. R., "A Viscoplastic Constitutive Theory for Metal Matrix Composites at High Temperatures," In: *Thermal Stress, Material Deformation, and Thermo–Mechanical Fatigue*, PVP ASME, Vol. 123, 1987.

55. Miller, A. K., *Unified Constitutive Equations for Creep and Plasticity*, Elsevier Applied Science, 1984, pp. 139–212.

56. Cailletaud, G., and Chaboche, J. L., "Macroscopic Description of the Microstructural Changes Induced by Varying Temperature: Example of In 100 Cyclic Behavior," ICM, 3, Vol. 2, 1979.

APPENDIX A

Included below is an extensive list of articles and reports concerning Hastelloy Alloy X. This literature addresses the many applications and experimental investigations conducted over the years. For completeness, those articles included in the annotative review (Chapter 2) will also be included in this list.

Arkoosh, M. A., and Fiore, N. F., "Elevated Temperature Ductility Minimum in Hastelloy Alloy X," Metallurgical Transactions, Vol. 3, Aug., 1972, pp. 2235–2240.

Bartolotta, P. A., "Thermomechanical Cyclic Hardening Behavior of Hastelloy X," NASA LeRC Contractor Report No. 174999, Nov., 1985.

Brinkman, C. R., "High Temperature Time Dependent Fatigue Behaviour of Several Engineering Structural Alloys," International Metals Reviews, Vol 30, No. 5, 1985, pp. 235–258.

Brinkman, C. R., Strizak, J. P., and Booker, M. K., "Use of Strain–Range Partitioning for Predicting Time–Dependent, Strain–Controlled Cyclic Lifetimes of Uniaxial Specimens of 2 1/4 Cr–Mo Steel, Type 316 Stainless Steel and Hastelloy X," Oak Ridge National Laboratory, Report No. ORNL/TM–5396, Jun., 1978.

Carden, A. E., Harman D. G., and Franco–Ferreira, E. A., "Thermal Fatigue Analysis of a Cryogenically Cooled Rocket Nozzle," Paper No. 102, American Astronautical Society, Southeastern Symposium, Huntsville, AL., Dec., 1966.

Carden, A. E., and Slade, T. B., "High–temperature Low–cycle Fatigue Experiments on Hastelloy X, In:*Fatigue at High Temperature*, ASTM Special Technical Publication 459, 1969, pp. 111–129.

Dicus, D. L., and Buckley, J. D., "The Effects of High Temperature Brazing and Thermal Cycling on the Mechanical Properties of Hastelloy X," In: *Proceedings of the Symposium on Welding, Bonding and Fastening*, NASA LaRC, Report No. N74–30922, 1974.

Ellis, J. R., Bartolotta, P. A., Allen, G. P., and Robinson, D. N., "Thermomechanical Characterization of Hastelloy X Under Uniaxial Cyclic Loading," Proceedings from Conf. on Turbine Engine Hot Section Technology, NASA LeRC , 1976, pp. 293–305.

Fujioka, J., Murase, H., and Matsuda, S., "Effect of Grain Size on Creep and Creep–rupture Properties of Hastelloy X," Japan Institute of Metals, Journal, Vol. 43, Nov., 1979, pp. 1078–1085.

Glasier, L. F., Jr., "Hastelloy X Properties, Data, and Metallurgical Characteristics," Atomic Energy Commission/NASA Tech Brief 68–10023, Feb., 1968.

Gregoire, J. "Determination of Allowable Stress for a Hastelloy Alloy X," Commissariat a l'Energie Atomique, Grenoble (France), Presented at 23rd Colloq. on Metallurgy, Saclay, France, Jun., 1980.

Hada, K., and Mutoh, Y., "Study of the Creep Constitutive Equation of Hastelloy X. I Generation of a Creep Constitutive Equation and its Sensitivity Analysis," JSME, Bulletin, Vol. 26, Nov., 1983, pp 1839–1848.

Harman, D. G., "Thermal Fatigue of Rocket Nozzle Cooling Tubes," Oak Ridge National Laboratories, Report No. ORNL/TM–2089, Feb., 1969.

Jaske, C. E., and Porfilio, T. L., "Low–Cycle Fatigue of Type 347 Stainless Steel and Hastelloy X in Hydrogen Gas Environment," Battelle Pacific Northwest Labs., Richland, WA., Report No. TID–SNA–2047, Dec., 1971.

Jaske, C. E., Rice, R. C., Buchheit, R. D., Roach, D. B., and Porfilio, T. L., "Low–Cycle Fatigue of Type 347 Stainless Steel and Hastelloy Alloy X in Hydrogen Gas and in Air at Elevated Temperatures," NASA LeRC Contract Report No. CR–135022, Jan., 1976.

Jordan, E. H., "Elevated Temperature Biaxial Fatigue," NASA LeRC Contractor Report No. 175009, Oct., 1985.

Kikuchi, M., Watanabe, K., and Kondo, T., "Effects of Cyclic Aging on Mechanical Properties and Microstructures of Hastelloy X," Japan Atomic Energy Research Inst., 1982, DOE Depository Libraries, Report No. DE83–703723.

Kotval, P. S., and Hatwell, H., "Discontinuous Precipitation of $M_{23}C_6$ Carbide in a Nickel–Base Superalloy," Transactions of the Metallurgical Society of AIME, Vol. 245, Aug., 1969, pp. 1821–1823.

Krantz, B. M., "An Investigation of Hot Cracking in Hastelloy X," Ph.D. Thesis, Rensselaer Polytechnic Inst., Troy, NY., 1966.

Lai, G. Y., "An Investigation of the Thermal Stability of a Commercial Ni–Cr–Fe–Mo Alloy (Hastelloy Alloy X)," Metallurgical Transactions from The American Society for Metals and The Metallurgical Society of AIME, Vol. 9A, Jun., 1978, pp. 827–833.

Lai, G. Y., and Thompson, L. D., "Effects of Thermal Aging on the Mechanical Properties of Ni–Cr–Mo–Fe (Hastelloy) Alloy," General Atomic Co., San Diego, CA., Presented at ASME Meeting, San Francisco, CA., Dec., 1978, Report No. GA–A–015016, Aug. 1978.

Levy, I. S., "The Influence of Thermomechanical Treatments on the Strength, High Temperature Stability and Microstructure of Hastelloy X–280," Battelle Northwest Labs., Richland, WA., Report No. BNWL–SA–1183, Aug., 1967.

Marchand, N. J., Ilschner, B., and Pelloux, R. M., "Non–isothermal Fatigue Crack Growth in Hastelloy–X," Fatigue and Fracture of Engineering Materials and Structures, Vol.10, No.1, 1987, pp. 59–74.

McKoy, H. E., and King, J. F., "Evaluation of Hastelloy X for Gas–Cooled Reactor Applications," Oak Ridge National Laboratory, Report No. ORNL/TM–8499, Nov.,1982.

McKoy, H. E., "Mechanical Properties of Hastelloy X and Inconel 617 After Aging 53,000 Hours in HTGR–He," Oak Ridge National Laboratory, Report No. ORNL/TM–9604, SEP., 1985.

Mihanovich, A. J., "Statistical Analysis of 347 Stainless Steel and Hastelloy X Fatigue Test Results," Aerojet Nuclear Systems Co.,Sacramento, CA., Report No. TID/SNA–2075, Oct., 1971.

Miner, R. V., Allen, G. P., Bartolotta, P. A., Mladsi, S. W., and Ellis, J. R., "Investigation of Cyclic Hardening Mechanisms in Hastelloy X," Proceedings from Conf. on Turbine Engine Hot Section Technology, NASA LeRC, 1987.

Moreno, V., "Evaluation of Three Constitutive Models for the Prediction of Hastelloy X Elevated Temperature Cyclic Response," In: *Nonlinear Constitutive Relations for High Temperature Applications*, NASA LeRC Report N83–34351, 1983, pp. 22–39.

Nishiguchi, I., Muto, Y., and Tsuji, H, "Design Fatigue Curves for Hastelloy X," Japan Atomic Energy Research Inst., DOE Depository Libraries, Report No. DE85–701031 1983.

Porfilio, T., and Jaske, C. E., "Compression Low–Cycle Fatigue of Type 347 Stainless Steel and Hastelloy X at Elevated Temperatures," Battelle Pacific Northwest Labs., Richland, WA., Report No. TID/SNA–2075, Apr., 1972.

Reynolds, M. B., "Strain–Cycle Phenomena in Thin Walled Tubing," General Electric Atomic Products, APED San Jose, CA., Report No. GEAP 4462, AEC Research and Development Report, Jan., 1964.

Richard, C. E., Duncan, J. D., Demogenes, C., and Flieder, W. G., "Low Cycle Fatigue Evaluation for Regeneratively Cooled Panels (Hastelloy X and Inconel 625 sheet and sandwich panel specimens)," AiResearch Mfg. Co., Los Angeles, CA., NASA Contract, Report No. NASA–CR–1884, Oct., 1971.

Robinson, D. N., "Thermomechanical Deformation in the Presence of Metallurgical Changes," Proceedings from Second Symposium on Nonlinear Constitutive Relations for High Temperature Applications, NASA LeRC, Report No. CP–2271, Jun., 1984.

Robinson, D. N., and Bartolotta, P. A., "Viscoplastic Constitutive Relationships with Dependence on Thermomechanical History," NASA LeRC Contractor Report No. 174836, Mar., 1985.

Seaver, D. W., "Low Cycle Fatigue Properties of Hastelloy X at 704°C / 1300°F/," In: *Methods for Predicting Material Life in Fatigue*; ASME Proceedings of the Winter Annual Meeting, New York, N.Y., Dec. 2–7, 1979, pp. 133–144.

Shimizu, S., and Ikemoto, Y., "High Temperature Low–Cycle Fatigue Strength of Hastelloy X," Japan Society of Materials Science, Journal, Vol. 26, Mar., 1977, pp. 255–261.

Stoller, D. R., "Material Evaluation of Hastelloy X," ACF Industries Inc., Albuquerque, NM., Report No. ACF–124, May, 1962.

Strizak, J. P., Brinkman, C. R., Booker M. K., and Rittenhouse, P. L., "Influence of Temperature, Environment and Thermal Aging on the Continuous Cycle Fatigue Behavior of Hastelloy X and Inconel 617," Oak Ridge National Laboratory, Report No. ORNL/TM–8130, Apr., 1982.

Suzuki, K., "Relaxation Characteristics of Hastelloy X," Japan Atomic Energy Research Inst. Report No. JAERI–M–8709, Feb., 1980, DOE Depository Libraries.

Tackett, J., "Fatigue Data on Hastelloy Alloy X," Report of Stellite Division, Cabot Corp., 1976.

Tawancy, H. M., "Long–term Aging Characteristics of Hastelloy X," Journal of Materials Science, Vol. 18, Oct., 1983, pp. 2976–2986.

Walker, K. P., "Research and Development Program for Nonlinear Structural Modeling with Advanced Time–Dependent Constitutive Relationships: Final Report," NASA LeRC Contract Report No. CR–165533, Nov., 1981.

Walker, K. P., "Representation of Hastelloy X Behavior at Elevated Temperature with a Functional Theory of Viscoplasticity," ASME Journal of Engineering Materials and Technology, 1981

Warren, M. R., "The Generation of Reliable Design Data for Long Term High Temperature Creep Applications —— of Hastelloy Alloy," In: *Mechanical Behaviour of Materials*; Proceedings of the Third International Conference, Cambridge, England, Vol. 2, August 20–24, 1979, pp 265 – 274.

APPENDIX B

Included here for completeness is the real–time FORTRAN 77 code used to perform the thermomechanical tests for this study. The Digital–to–Analog (D/A) and Analog–to–Digital (A/D) calls specified, are compatable with a digital conversion board manufactured by the Data General Corporation.

```
%INCLUDE 'SAMPAR.F77'
C
    EXTERNAL IDS23,IDA00,IDA10,IDA12
    CHARACTER*10 DATAFILE
    DOUBLE PRECISION
STRAIN,MECHSTRAIN,THERMSTRAIN,RELOAD,TEMPER,TEMP
    DOUBLE PRECISION A,B,C,D RLT,UT,USL,RLSL,VLSB,TI,TISMALL
    DOUBLE PRECISION HIADJ,RLADJ,CHECK1,CHECK2,LASTEMPER
    DIMENSION IORBA(16),IDA3(2),IAD1(3),IAD2(3)
    INTEGER*4 LOADSUM,STRAINSUM,TEMPSUM
    LOGICAL DELAY /.FALSE./
    LOGICAL DELCONTIN /.FALSE./
    LOGICAL SWITCH /.FALSE./
    LOGICAL INPHASE /.TRUE./
    CALL DSTRT(IER)
    VLSB=20.0/65520.0
    IDATA=0
    ICYCLE=0
    ILOAD=0
    ISTRAIN=0
    IPIT=0
    IFLAG=1
    ITEMP=0
    INTERVAL=10
    IDA1=IOR(40000K,4000K)
    IDA1=IOR(IDA1,10000K)
    IDA2=2
    IAD1(1)=0
    IAD1(2)=1
    IAD1(3)=3
    IAD2(1)=177777K
    IAD2(2)=177777K
    IAD2(3)=177777K
    IAD3=3
    ITTL1=040000K
    ITTL2=177777K
```

```
      ITTL3=0
      STRAIN=0.0
      MECHSTRAIN=0.0
      THERMSTRAIN=0.0
      TEMPER=0.0
      TEMP=0.0
      CHECK1=0.0
      CHECK2=0.0
      PRINT*,CHAR(12)
      PRINT*,'          TTTTTTTTTTT   M       M   DDDDDDDD '
      PRINT*,'             T      M M    M M   D      D '
      PRINT*,'             T      M  M   M  M   D      D'
      PRINT*,'             T      M   M M   M   D      D'
      PRINT*,'             T      M    M    M   D     D '
      PRINT*,'             T      M         M   DDDDDDDD '
      PRINT*,' '
      PRINT*,' '
      PRINT*,' '
   10 PRINT*,'   ********* ENTER INITIAL VALUES IN SPECIFIED UNITS
      &*******'
      PRINT*,' '
      PRINT*,'ENTER NAME FOR THIS DATAFILE === '
      READ(*,101) DATAFILE
  101 FORMAT(A)
      OPEN(UNIT=13,FILE=DATAFILE,STATUS='NEW')
      PRINT*,' '
      PRINT*,'ENTER TEMPERATURE AT MAXIMUM MECHANICAL
    STRAIN [degrees C ] === '
      READ*,UT
      PRINT*,'ENTER TEMPERATURE AT MINIMUM MECHANICAL
    STRAIN [degrees C ] === '
      READ*,RLT
      PRINT*,'ENTER TEMPERATURE LAG AT MAXIMUM MECHANICAL
    STRAIN [degrees C] === '
      READ*,HIADJ
      PRINT*,'ENTER TEMPERATURE LAG AT MIMIMUM MECHANICAL
    STRAIN [degrees C] === '
      READ*,RLADJ
      PRINT*,'ENTER TEMPERATURE INCREMENT FACTOR FOR
    CATCH-UP WAVE [from 0.1 to 0.95] === '
      READ*,TISMALL
      PRINT*,'ENTER UPPER MECHANICAL STRAIN LIMIT [% strain] ===
      READ*,USL
      PRINT*,'ENTER LOWER MECHANICAL STRAIN LIMIT [% strain] ===
      READ*,RLSL
      PRINT*,'ENTER MECHANICAL STRAIN RATE [in/in per sec] === '
      READ*,RATE
      PRINT*,'ENTER RELOAD TEMPERATURE [degrees C] === '
      READ*,RELOAD
```

```
    PRINT*,'FOR THE RELATIONSHIP    THERMSTRAIN = C x T + D'
    PRINT*,'       ENTER C (v/c) === '
    READ*,C
    PRINT*,CHAR(12)
 20  PRINT*,'HOW WOULD YOU LIKE TO RESTART THE TEST ?'
    PRINT*,'(1 === POSITIVE STRAIN THEN MECHANICAL STRAIN
INCREMENT)'
    PRINT*,'(2 === POSITIVE STRAIN THEN MECHANICAL STRAIN
DECREMENT)'
    PRINT*,'(3 === NEGATIVE STRAIN THEN MECHANICAL STRAIN
INCREMENT)'
    PRINT*,'(4 === NEGATIVE STRAIN THEN MECHANICAL STRAIN
DECREMENT)'
    PRINT*,'(5 === BEGIN A NEW TEST)'
    PRINT*,' '
    PRINT*,'      CHOICE =====   '
    READ*,IANS
    IF ((IANS.LT.1).OR.(IANS.GT.5)) GOTO 20
    PRINT*,'WHAT CYCLE NUMBER ARE YOU ON ? ===   '
    READ*,ICYCLE
    PRINT*,'WHAT CYCLE WOULD YOU LIKE TO RECORD NEXT ?
===   '
    READ*,IDATA
    PRINT*,'ENTER THE DATA SAMPLE RATE [sec/point]  ===   '
    READ*,COLLECT
    SI=((0.01*RATE)/0.002) ! STRAIN (volts) PER PITCALL
    IF (IDATA.GT.1) THEN
     IFLAG=0
    ELSE
     IDATA=0
    ENDIF
    UTEMP=UT
    RLTEMP=RLT
    USL=USL/0.2
    RLSL=RLSL/0.2
    CHECK1=5.*USL/6.          ! BEGINING OF TEMPERATURE DELAY
      CHECK
    CHECK2=5.*RLSL/6.         ! BEGINING OF TEMPERATURE DELAY
      CHECK
    UT=UT/343.+1.
    RLT=RLT/343.+1.
    ISTORE=COLLECT*100
    A=(UT-RLT)/(USL-RLSL)  ! MASTER-SLAVE FOR TEMPERATURE
    B=(RLT-UT)*RLSL/(USL-RLSL)+RLT
C *** THIS CALCULATES THE MECHANICAL STRAIN
CORRESPONDING TO THE RELOAD TEMPERATURE VIA THE
MASTER-SLAVE RELATIONSHIP    ***
    IF (IANS.NE.5) THEN
     RELOAD=((RELOAD/343.+1.)-B)/A !CHANGE TEMP TO A STRAIN
```

```
VIA A&B
     TEMPER=A*(RELOAD)+B
    ELSE
     RELOAD=0.0
     TEMPER=B
    END IF
     D=((TEMPER–1.0)*343.0)*(–1)*C  ! Ea = 0  AT PROPER  Em
     C=C*275.925*VLSB
C
C  TISMALL IS A USER SPECIFIED PERCENTAGE OF THE
TEMPERATURE INCREMENT PER PITCALL.  THIS ALLOWS THE
MASTER–SLAVE EQUATION TO 'CATCH UP' TO THE ACTUAL
SPECIMEN TEMPERATURE IN A SMOOTH MANNER AFTER THE
RAMPING WAVE IS REVERSED.
C
    TISMALL=((UT–RLT)*SI/(USL–RLSL))*TISMALL
    IF (UT.GT.RLT) THEN
     TI=(1./343.)/100.
     INPHASE=.TRUE.
    ELSE
     TI=(–1./343.)/100.
     INPHASE=.FALSE.
    END IF
    PRINT*,CHAR(12)
    PRINT*,'A = ',A,'    B = ',B
    PRINT*,'C = ',C,'    D = ',D
    IDA3(1)=STRAIN/VLSB
    IDA3(2)=TEMPER/VLSB
    PRINT*,'CHECK INFORMATION THAT WAS ENTERED.'
    PRINT*,'UPPER TEMPERATURE IS  ',UTEMP,' C'
    PRINT*,'LOWER TEMPERATURE IS  ',RLTEMP,' C'
    PRINT*,'UPPER STRAIN LIMIT IS  ',USL*.2,' % strain'
    PRINT*,'LOWER STRAIN LIMIT IS  ',RLSL*.2,' % strain'
    PRINT*,'INTERVAL =  ',INTERVAL,' sec x 10–3'
    PRINT*,'    '
    PRINT*,'RELOAD MECHANICAL STRAIN = ',RELOAD,' volts'
    PRINT*,'RELOAD TEMPERATURE = ',(TEMPER–1.)*343.,' degrees C'
    PRINT*,'    '
    PRINT*,'SAMPLE RATE =  ',COLLECT,' sec/point'
    PRINT*,'    '
    PRINT*,'    '
    PRINT*,'IF CORRECT ENTER 1 IF NOT ENTER 0  '
    READ*,INOT
    IF (INOT.NE.1) GO TO 10
 30   IF (TEMPER.GE.5.10) GO TO 1000
          IDA3(2)=TEMPER/VLSB
          CALL DOITW(IORBA,IDS23,8,IDA1,IDA2,IDA3,IER)
          CALL DOITW(IORBA,IDA00,8,IAD1,IAD2,IAD3,IER)
          TEMP=IAD2(3)*VLSB
```

```
      PAUSE 'REMOTE TEMPERATURE IS BEING ADJUSTED  ENTER
NEW LINE TO CONTINUE'
            CALL DOITW(IORBA,IDA00,8,IAD1,IAD2,IAD3,IER)
            STRAIN=IAD2(2)*VLSB
            TEMP=IAD2(3)*VLSB
      PRINT*,' '
      PRINT*,'PRESENT A to D TEMPERATURE IS ',TEMP*275.925,' C'
      PRINT*,' '
      PRINT*,'THE REMOTE TEMPERATURE HAS BEEN ADJUSTED TO
ITS SLAVE VALUE'
      PRINT*,'              ENTER 0 TO START THE TEST    '
      PRINT*,' '
      PRINT*,'                 ========  '
      READ*,IMIDADJ
      IF (IMIDADJ.NE.0) THEN
            CALL DOITW(IORBA,IDS23,8,IDA1,IDA2,IDA3,IER)
            TEMPER=TEMPER+(FLOAT(IMIDADJ)/686.)
            GO TO 30
      ENDIF
C*********************************************************************
C*********************************************************************
      CALL IDEFPIT (ISTAT,INTERVAL)
C
C ***** INCREMENT MECHANICAL STRAIN UNDER ISOTHERMAL
CONDITIONS      *****
C
      IF (IANS.EQ.5) GO TO 40
C
C
      IF ((IANS.EQ.1).OR.(IANS.EQ.2)) THEN
       DO WHILE (MECHSTRAIN.LE.RELOAD)
        IDA3(1)=MECHSTRAIN/VLSB
        CALL PEND(ISTAT)
        CALL DOITW(IORBA,IDS23,8,IDA1,IDA2,IDA3,IER)
                CALL DOITW(IORBA,IDA00,8,IAD1,IAD2,IAD3,IER)
        MECHSTRAIN=MECHSTRAIN+SI
       END DO
         STRAIN=MECHSTRAIN
       IF (IANS.EQ.1) GOTO 40
       GOTO 50
      END IF
      DO WHILE (MECHSTRAIN.GE.RELOAD)
       IDA3(1)=MECHSTRAIN/VLSB
       CALL PEND(ISTAT)
       CALL DOITW(IORBA,IDS23,8,IDA1,IDA2,IDA3,IER)
       CALL DOITW(IORBA,IDA00,8,IAS1,IAD2,IAD3,IER)
       MECHSTRAIN=MECHSTRAIN-SI
      END DO
       STRAIN=MECHSTRAIN
```

```
      IF (IANS.EQ.3) GOTO 40
      GOTO 50
C
C
 40   DELAY=.FALSE.
      DELCONTIN=.FALSE.
      ICYCLE=ICYCLE+1
      IF (IFLAG.EQ.1)THEN
       IFLAG=0
       IF (IDATA.GE.99) INT=100
       IF (IDATA.LT.99) INT=20
       IF (IDATA.LT.19) INT=5
       IF (IDATA.LT.4) INT=3
       IF (IDATA.LE.1) INT=1
       IDATA=IDATA+INT
      END IF
      IF (ICYCLE.EQ.IDATA)  WRITE(13,100) ICYCLE,ICYCLE,ICYCLE
C
C
      CALL DOITW(IORBA,IDA10,8,ITTL1,ITTL2,ITTL3,IER)
C
C     ********* INCREMENT STRAIN WAVE FORM *********
C
      DO WHILE (MECHSTRAIN.LT.USL)
       IF (DELAY) THEN
        IF ((ABS(TEMP-UTEMP).LT.HIADJ).OR.(DELCONTIN)) THEN
         DELCONTIN=.TRUE.
          TEMPER=TEMPER-TI
         GO TO 60
        END IF
       END IF
       TEMPER=A*MECHSTRAIN+B
       IF (SWITCH) THEN
        IF((INPHASE).AND.(TEMPER.GE.LASTEMPER)) THEN
         SWITCH=.FALSE.
        ELSE IF ((.NOT.INPHASE).AND.(TEMPER.LE.LASTEMPER)) THEN
         SWITCH=.FALSE.
        ELSE
          LASTEMPER=LASTEMPER+TISMALL
         TEMPER=LASTEMPER
        END IF
       END IF
 60    IDA3(1)=STRAIN/VLSB
       IDA3(2)=TEMPER/VLSB
        IF (TEMPER.GE.5.10) GO TO 1000
       CALL PEND(ISTAT)
       CALL DOITW(IORBA,IDS23,8,IDA1,IDA2,IDA3,IER)
       CALL DOITW(IORBA,IDA00,8,IAD1,IAD2,IAD3,IER)
       MECHSTRAIN=MECHSTRAIN+SI
```

```
      THERMSTRAIN=FLOAT(IAD2(3))*C+D
      STRAIN=THERMSTRAIN+MECHSTRAIN
      TEMP=FLOAT(IAD2(3))*VLSB*275.925 ! TEMP IN DEGREES C
      IF ((.NOT.DELAY).AND.(MECHSTRAIN.GT.CHECK1))
DELAY=.TRUE.
       IF((IPIT.EQ.ISTORE).AND.(IFLAG.EQ.1)) THEN
       ILOAD=LOADSUM/IPIT
       ISTRAIN=STRAINSUM/IPIT
       ITEMP=TEMPSUM/IPIT
       WRITE(13,100) ILOAD,ISTRAIN,ITEMP
       IPIT=0
       LOADSUM=0
       STRAINSUM=0
       TEMPSUM=0
      END IF
      IF ((ICYCLE.EQ.IDATA).AND.(IFLAG.EQ.0)) THEN
         IFLAG=1
         IPIT=0
         LOADSUM=0
         STRAINSUM=0
         TEMPSUM=0
       END IF
      IF(IFLAG.EQ.1) THEN
       LOADSUM=LOADSUM+IAD2(1)
       STRAINSUM=STRAINSUM+IAD2(2)
       TEMPSUM=TEMPSUM+IAD2(3)
       IPIT=IPIT+1
      END IF
    END DO
    LASTEMPER=TEMPER
    SWITCH=.TRUE.
C
C
C   ********* DECREMENT STRAIN WAVE FORM *********
C
C
50  DELAY=.FALSE.
    DELCONTIN=.FALSE.
    DO WHILE (MECHSTRAIN.GT.RLSL)
     IF (DELAY) THEN
      IF ((ABS(TEMP-RLTEMP).LT.RLADJ).OR.(DELCONTIN)) THEN
       TEMPER=TEMPER+TI
       GO TO 70
      END IF
     END IF
     TEMPER=A*MECHSTRAIN+B
     IF (SWITCH) THEN
      IF ((INPHASE).AND.(TEMPER.LE.LASTEMPER)) THEN
         SWITCH=.FALSE.
```

```
      ELSE IF ((.NOT.INPHASE).AND.(TEMPER.GE.LASTEMPER))
THEN
       SWITCH=.FALSE.
      ELSE
       LASTEMPER=LASTEMPER-TISMALL
       TEMPER=LASTEMPER
       END IF
     END IF
 70   IDA3(1)=STRAIN/VLSB
     IDA3(2)=TEMPER/VLSB
     IF (TEMPER.GE.5.10) GO TO 1000
     CALL PEND(ISTAT)
     CALL DOITW(IORBA,IDS23,8,IDA1,IDA2,IDA3,IER)
     CALL DOITW(IORBA,IDA00,8,IAD1,IAD2,IAD3,IER)
     MECHSTRAIN=MECHSTRAIN-SI
     THERMSTRAIN=FLOAT(IAD2(3))*C+D
     STRAIN=THERMSTRAIN+MECHSTRAIN
     TEMP=FLOAT(IAD2(3))*VLSB*275.925
     IF ((.NOT.DELAY).AND.(MECHSTRAIN.LT.CHECK2))
DELAY=.TRUE.
     IF((IPIT.EQ.ISTORE).AND.(IFLAG.EQ.1)) THEN
      ILOAD=LOADSUM/IPIT
      ISTRAIN=STRAINSUM/IPIT
      ITEMP=TEMPSUM/IPIT
       WRITE(13,100) ILOAD,ISTRAIN,ITEMP
       IPIT=0
      LOADSUM=0
      STRAINSUM=0
      TEMPSUM=0
      END IF
     IF ((ICYCLE.EQ.IDATA).AND.(IFLAG.EQ.0)) THEN
       IFLAG=1
       IPIT=0
       LOADSUM=0
       STRAINSUM=0
       TEMPSUM=0
     END IF
     IF(IFLAG.EQ.1) THEN
      LOADSUM=LOADSUM+IAD2(1)
      STRAINSUM=STRAINSUM+IAD2(2)
      TEMPSUM=TEMPSUM+IAD2(3)
      IPIT=IPIT+1
     END IF
    END DO
    LASTEMPER=TEMPER
    SWITCH=.TRUE.
    GO TO 40
1000  CALL REMVPIT(ISTAT)
    IDA3(1)=0.00
```

```
      IDA3(2)=0.00
      CALL DOITW(IORBA,IDS23,8,IDA1,IDA2,IDA3,IER)
100     FORMAT(2X,I6,4X,I6,4X,I6)
      STOP
      END
```

NASA
National Aeronautics and Space Administration

Report Documentation Page

1. Report No.	2. Government Accession No.	3. Recipient's Catalog No.
NASA CR-185188		

4. Title and Subtitle	5. Report Date
Thermomechanical Deformation Testing and Modeling in the Presence of Metallurgical Instabilities	January 1990
	6. Performing Organization Code

7. Author(s)	8. Performing Organization Report No.
Michael G. Castelli	None (E-5243)
	10. Work Unit No. 505-63-1B

9. Performing Organization Name and Address	11. Contract or Grant No.
Sverdrup Technology, Inc. NASA Lewis Research Center Group Cleveland, Ohio 44135	NAS3-25266
	13. Type of Report and Period Covered Contractor Report Final

12. Sponsoring Agency Name and Address	14. Sponsoring Agency Code
National Aeronautics and Space Administration Lewis Research Center Cleveland, Ohio 44135-3191	

15. Supplementary Notes

Project Manager, Rod Ellis, Structures Division, NASA Lewis Research Center. This report was a thesis submitted in partial fulfillment of the requirements for the degree of Master of Science in Engineering to the University of Akron, Akron, Ohio 44325 in January 1990.

16. Abstract

A number of viscoplastic constitutive models have been developed to describe deformation behavior under complex combinations of thermal and mechanical loading. Questions remain, however, regarding the validity of procedures used to characterize these models for specific structural alloys. One area of concern is that the majority of experimental data available for this purpose are determined under isothermal conditions. This experimental study is aimed at determining whether viscoplastic constitutive theories characterized using an isothermal data base can adequately model material response under the complex thermomechanical loading conditions typical of power generation service. The approach adopted was to conduct a series of carefully controlled thermomechanical experiments on a nickel-based superalloy, Hastelloy Alloy X. Previous investigations had shown that this material experiences metallurgical instabilities leading to complex hardening behavior, termed dynamic strain aging. Investigating this phenomenon under full thermomechanical conditions leads to a number of challenging experimental difficulties which up to the present work were unresolved. To correct this situation, a number of advances were made in thermomechanical testing techniques. Advanced methods for dynamic temperature gradient control, phasing control and thermal strain compensation were developed and incorporated into real-time test control software. These advances allowed the thermomechanical data to be analyzed with minimal experimental uncertainty. The thermomechanical results were evaluated on both a phenomenological and microstructural basis. Phenomenological results revealed that the thermomechanical hardening trends were not bounded by those displayed under isothermal conditions. For the case of Hastelloy Alloy X (and similar dynamic strain aging materials), this strongly suggests that some form of thermomechanical testing is necessary when characterizing a thermoviscoplastic deformation model. Transmission electron microscopy was used to study the microstructural physics, and analyze the unique phenomenological behavior. In general, the thermomechanical response was found to be dominated by behavioral trends associated with the maximum cycle temperature. Having clearly identified the factors affecting the thermomechanical behavior, an existing thermoviscoplastic constitutive model is extended to qualitatively predict the thermomechanical hardening trends of Hastelloy Alloy X, a dynamic strain aging material. The approach taken in this study involves the introduction of an evolving internal state variable which accounts for the effects of microstructural changes under thermomechanical conditions.

17. Key Words (Suggested by Author(s))	18. Distribution Statement
Thermomechanical testing Viscoplastic modeling Hastelloy X Dynamic strain aging	Unclassified – Unlimited Subject Category 39

19. Security Classif. (of this report)	20. Security Classif. (of this page)	21. No. of pages	22. Price*
Unclassified	Unclassified	173	A08

*For sale by the National Technical Information Service, Springfield, Virginia 22161